NICKEL SELENIDE-BASED ELECTROCHEMICAL SENSORS FOR THE DETERMINATION OF NEVIRAPINE DRUG IN WASTEWATER

by

GINNY SASHA TITO

submitted in accordance with the requirements
for the degree of

MASTER OF SCIENCE

in the subject

CHEMISTRY

at the

UNIVERSITY OF SOUTH AFRICA

SUPERVISOR: PROF. USISIPHO FELENI

CO-SUPERVISORS: PROF. ALEX T. KUVAREGA
PROF. ABOLANLE S. ADEKUNLE

FEBRUARY 2022

DECLARATION

Name: Ginny Sasha Tito
Student number: 67133193
Degree: Master of Science: Chemistry

Exact wording of the title of the dissertation as appearing on the electronic copy submitted for examination:

NICKEL SELENIDE-BASED ELECTROCHEMICAL SENSORS FOR THE DETERMINATION OF NEVIRAPINE DRUG IN WASTEWATER

I declare that the above dissertation is my own work and that all the sources that I have used or quoted have been indicated and acknowledged by means of complete references.

I further declare that I submitted the dissertation to originality checking software and that it falls within the accepted requirements for originality.

I further declare that I have not previously submitted this work, or part of it, for examination at Unisa for another qualification or at any other higher education institution.

(The dissertation will not be examined unless this statement has been submitted.)

03/02/2022

SIGNATURE DATE

ACKNOWLEDGMENTS

First and foremost, I want to thank God for the gift of life and for granting me this opportunity to pursue and complete my studies. All the Honour and Glory belong to Him.

My sincere gratitude and appreciation go to my supervisor, Prof. Usisipho Feleni. I am indebted to you for devoting so much time to educating me about various aspects of electrochemistry including equipment knowledge, operation and data analysis. Your willingness to assist me with anything at any time is truly appreciated. Under your kind guidance, motivation, invaluable support, and contributions throughout this work, I was able to complete it and learn to become a better electrochemist. I would also like to thank my co-supervisors, Prof. Alex T. Kuvarega and Prof. Abolanle S. Adekunle, for their support and guidance during the course of this study.

To my loving husband and best friend, Ngonidzashe Masunga, thank you so much for your unconditional love, unwavering support, proofreading my thesis, motivation, and being my pillar of strength throughout this study. You have been very understanding of the hard work and stress that research can bring, and for that, thank you for making the burden lighter. To our bundle of joy, Adiel Masunga, I love you, my baby! Thank you for all the priceless moments you share with us. You are such a blessing to us.

To my parents, Mr and Mrs Tito, thank you so much for all the love, care, and support. Your unceasing prayers have protected and carried me throughout this journey. Thank you for all the sacrifices you made for me to be where I am today, as I would not have made it to this point without you. I thank God for you every day, and I am forever grateful. I would also like to express my gratitude to my siblings, Gracious, Gwen, and Grant Tito, for their support throughout my studies. The love I have for you guys is immeasurable. The support received from the Tito and Masunga families at large is greatly appreciated.

My special thanks go to the iNanoWS students and staff members. Many thanks to the helpful lab technicians at iNanoWS; Prof. Nyoni, Mr Mokalane, and Mrs Magwaza. To the Applied Electrochemistry Thematic Area: I appreciate all the research meetings that we had and thank you all for your various inputs. Many thanks to my friends Simbongile Gumbi, Mpho Khorae, Fungai Chibaya and Thompho Ravele for making the lab work experience more fun. I would like to thank the National Research Foundation and iNanoWS for their financial support.

DEDICATION

I dedicate this work to my parents, Mr G. Tito and Mrs S. Tito.

PUBLICATIONS

Rebotiloe Morare, Ginny Sasha Tito, Muthumuni Elizabeth Managa, Usisipho Feleni, Recent developments in waterborne pathogen detection technologies, submitted to ACS Sensors.

Ginny Sasha Tito, Adekunle Saheed Abolanle, Alex Tawanda Kuvarega, Bhekie Brilliance Mamba, Usisipho Feleni, Metal chalcogenide-based electrochemical sensor for electro-oxidation of nevirapine in water samples, submitted to ChemistrySelect.

Ginny Sasha Tito, Alex Tawanda Kuvarega, Usisipho Feleni, Banana extract functionalized Nickel Selenide quantum dot-based electrochemical sensor system for sensing and signalling nevirapine drug, submitted to Electrocatalysis.

Ginny Sasha Tito, Adekunle Saheed Abolanle, Alex Tawanda Kuvarega, Azeez Olayiwola Idris, Bhekie Brilliance Mamba, Usisipho Feleni, Nickel selenide quantum dot applications in electrocatalysis and sensors, Electroanalysis, 32(12), 2020, pp. 2603-2614.

PRESENTATIONS

Ginny Sasha Tito, Adekunle Saheed Abolanle, Alex Kuvarega, Usisipho Feleni, The presence and negative effects of ARV drugs in South African water sources. Oral presentation. FameLab SA/ Unisa Reagional Heat 2021. University of South Africa, South Africa, 21 April 2021.

Ginny Sasha Tito, Usisipho Feleni, Embracing 4IR in electrochemistry, National Science Week Programme, University of South Africa, South Africa, 2-6 August 2021

Ginny Sasha Tito, Adekunle Saheed Abolanle, Alex Kuvarega, Usisipho Feleni, Detection of nevirapine drug using synthesised 3-mercaptopropionic acid capped nickel selenide quantum dots. Oral presentation. Applied Electrochemistry Thematic Area. Phapha Building. University of South Africa, South Africa, 11 August 2021.

Ginny Sasha Tito, Adekunle Saheed Abolanle, Alex Kuvarega, Usisipho Feleni, Development of a smart electrochemical sensor for the determination of nevirapine drug in water. Oral presentation. FameLab SA/ Semi-finals 2021. University of South Africa, South Africa, 28 September 2021.

ABSTRACT

The occurrence of antiretroviral drugs (ARVs) in most water sources in South Africa has been of major concern over the past decade. Though they have been reported to occur in low concentrations (low ng/L and µg/L), their increasing concentration poses health risks to humans, animals, and aquatic organisms. This accelerates the emergence of antiretroviral resistance. The consequences of these adverse effects on human health are therefore very concerning. Nevirapine (NVP) is one of the most extensively used ARVs worldwide for the prevention of mother-to-child transmission and has been often detected in water sources. These drugs enter water systems in various ways, including incorrect disposal of unused or expired drugs, via treated or untreated wastewater from the municipality, discharge from hospital wastewater, effluent from sewage treatment plants and industrial wastewater. Several chromatographic methods have been employed in its detection in water, but their high costs and sophisticated nature limit their use in a variety of applications. Very limited research is available on the electrochemical detection of nevirapine in real wastewater samples, as most studies present its detection in human serum or pharmaceutical formulations. Therefore, this work presents the use of novel electrochemical sensor systems for the detection of nevirapine in real wastewater samples. The electrochemical sensor systems were developed by depositing functionalised nickel selenide quantum dots ($NiSe_2QD$) onto an L-cysteine or Nafion-modified gold electrode. The quantum dots were prepared using a simple and cost-effective aqueous method, capped with banana peel extract (BPE) and 3-mercaptopropionic acid (3-MPA) to improve their stability and prevent agglomeration. Microscopic, spectroscopic, and electrochemical techniques were used to determine the properties of the synthesised quantum dots. Fourier transform infrared spectroscopy (FTIR) confirmed the capping of 3-MPA-$NiSe_2QD$, where the SH group absorption band disappeared from the spectra of 3-MPA-$NiSe_2QD$ and decrease in intensity for the COOH groups. The increase in intensity and the shifting of bands to higher wavenumbers were observed for BPE-$NiSe_2QD$. The size of the quantum dots (< 10 nm) was revealed by High-resolution transmission microscopy (HR-TEM) and small-angle X-ray scattering (SAXS). The optical properties of $NiSe_2QD$ were studied by ultraviolet-visible spectroscopy (UV-Vis), which produced absorbance bands at 331 nm and 329 nm corresponding to energy bandgap values of 3.91 eV and 2.99 eV for 3-MPA and BPE-capped $NiSe_2QD$, respectively. Differential pulse voltammetry (DPV) was used to study the electrochemical responses of 3-MPA-$NiSe_2QD$/L-cyst/Au and Au/BPE-$NiSe_2QD$/Nafion to NVP, with a characteristic oxidation peak at 0.76 V. This was performed in 0.1 M phosphate buffer solution (PBS) at a scan rate of 30 mV/s. The electrochemical sensors exhibited enhanced electroactivity, which was attributed to the catalytic effect of the incorporated quantum dots. This was characterised by the low limit of detection (LOD) values of 0.0035 ng/L and 0.0064 ng/L for 3-MPA-NiSe$_2$QD/L-cyst/Au and Au/BPE-NiSe$_2$QD/Nafion sensors, respectively. However, the 3-MPA-NiSe$_2$QD/L-cyst/Au electrochemical sensor produced the best signal with higher a sensitivity of 6.15 µA/pM compared to 5.52 µA/pM for Au/BPE-NiSe$_2$QD/Nafion. The oxidation peak current of NVP had a linear range of 0–1.21 pM with a correlation coefficient of 0.998. The application of both sensors in the determination of nevirapine in real wastewater samples showed good recoveries in the range of 85%-108%, which indicates that the sensors are suitable for real-time sample analysis.

KEYWORDS

Banana peel extract

3-Mercaptopropionic acid

Nickel selenide

Quantum dots

Electrochemical sensor

Nevirapine

Differential pulse voltammetry

Limit of detection

ABBREVIATIONS

AIDS	Acquired immunodeficiency Syndrome
ARVs	Antiretroviral drugs
ASV	Adsorptive stripping voltammetry
AuE	Gold electrode
AuNPs/p((MB)/MWCNTs/GE	Gold nanoparticles/poly(methylene-blue)/multi-walled carbon nanotubes/Graphite electrode
BPE	Banana peel extract
Bi_2O_3/CPE	Bismuth oxide/Carbon paste electrode
CD4	Cluster of differentiation 4
CE	Counter electrode
CNTs	Carbon nanotubes
CoLS	Colloidal
COOH	Carboxylic acid
CuO/CNPs/GCE	Copper oxide-carbon nanoparticles/glassy carbon electrode
CV	Cyclic voltammetry
CYP3A4	Cytochrome P450-3A4 enzyme
DCF	Diclofenac
DNA	Deoxyribonucleic acid
DPASV	Differential pulse anodic stripping voltammetry
DPV	Differential pulse voltammetry
DSSCs	Dye-sensitised solar cells
ED	Electrodeposition
EDC	1-ethyl-3(3-dimethylaminopropyl) carbodiimide hydrochloride
E_{pa}	Anodic peak potential
E_{pc}	Cathodic peak potential
Eu^{3+}/Cu_2O/GCE	Cubic europium/cuprous oxide-modified glassy carbon electrode
FeNiSe/NF	Iron-nickel-selenide/Nickel foam
FTIR	Fourier transform infrared spectroscopy
FWHM	Full-width half-maximum
GCE	Glassy carbon electrode
GC-MS	Gas chromatography-mass spectrometry
GC-TOFMS	Gas chromatography-time of flight mass spectrometry

GIFT	Generalised Indirect Fourier Transformation
GSH	Glutathione
HAART	Highly active antiretroviral therapy
HER	Hydrogen evolution reaction
Hg/CPE	Mercury/carbon paste electrode
HI	Hot injection
HIV	Human Immunodeficiency Virus
HR-SEM/EDX	High-resolution scanning electron microscopy/Energy-dispersive X-ray spectroscopy
HR-TEM	High-resolution transmission electron microscopy
HT	Hydrothermal
Jsc	Short-circuit current density
LC-MS/MS	Liquid chromatography coupled to (tandem) mass spectrometry
L-cyst	L-cysteine
LOD	Limit of detection
LSV	Linear sweep voltammetry
µg/L	Microgram per litre
MIP/CPE	Molecularly imprinted polymer/Carbon paste electrode
3-MPA	3-mercaptopropionic acid
NF	Nickel foam
ng/L	Nanogram per litre
NH	Amine
NHS	N-Hydroxysuccinimide
$NiSe_2QD$	Nickel selenide quantum dots
NNRTIs	Non-nucleoside reverse transcriptase inhibitors
NRTIs	Nucleoside reverse transcriptase inhibitors
NS	Nanosheets
NVP	Nevirapine
OER	Oxygen evolution reaction
OH	Hydroxyl
PBS	Phosphate buffer solution
PCE	Power conversion efficiency
PDDF	Pair distance distribution function

Pd@rGO/MoS_2QD/GCE	Palladium nanoparticles supported reduced graphene oxide decorated with molybdenum disulphide quantum dots-modified glassy carbon electrode
PI	Protease inhibitors
PL	Photoluminescence
PST	Primary settling tank
QD	Quantum dots
QDSSCs	Quantum dot sensitised solar cells
R_{ct}	Charge transfer resistance
RE	Reference electrode
RGO	Reduced graphene oxide
RNA	Ribonucleic acid
SAXS	Small-angle X-ray scattering
SLS	Solid-liquid solution
SSR	Solid-state reaction (SSR)
ST	Solvothermal
SWSV	Square wave stripping voltammetry
WWTPs	Wastewater treatment plants
TGA	Thioglycolic acid
TiO_2/GNR	Titanium oxide/graphene nanoribbons
TOP	Trioctylphosphine
TOPO	N-octylphosphine oxide
UPLC-ESI-MS/MS	Ultrahigh performance liquid chromatography coupled to a triple quadrupole mass spectrometry, with electrospray ionization
Ura/CPE	Uracil/carbon paste electrode
UV-Vis	Ultraviolet-visible spectrometry
WE	Working electrode
WHO	World health organisation
XRD	X-ray diffraction
XTC's	Xenobiotic trace chemicals

TABLE OF CONTENTS

LIST OF FIGURES

LIST OF TABLES

CHAPTER ONE

INTRODUCTION

Summary

This chapter provides an overview of human immunodeficiency virus-acquired immunodeficiency syndrome (HIV/AIDS) and the anti-retroviral drugs used to treat HIV-positive individuals. It also discusses the prevalence of pharmaceuticals in water and their adverse effects. Additionally, this chapter presents the problem statement and motivation, aim and objectives, and the outline of the thesis.

1.1 Pharmaceutical contaminants

Pharmaceuticals consist of a wide range of organic compounds that are designed to produce a therapeutic effect on the body. Pharmaceuticals were developed to improve human and animal health and livestock farming. Some of these pharmaceuticals include non-steroidal drugs such as analgesics, antibiotics, anti-epileptics and antiretroviral drugs, veterinary drugs, therapeutic drugs, and biotechnological products, just to mention a few [1–5]. These pharmaceutical drugs can be bought over the counter at pharmacies (with or without a prescription), obtained from the hospital or clinic, or prescribed by the doctor at a surgery. The high demand for pharmaceuticals is greatly triggered by the emergence of new diseases, ageing societies in developed countries and the growing population worldwide [3,6]. Sometimes, these pharmaceuticals are partially transformed by humans and animals, leading to their excretion through faeces and urine as a mixture of metabolites and parent compounds. This is due to their non-biodegradable nature, which signifies a high resistance to environmental transformation processes. Therefore, they have emerged as environmental pollutants [7,8]. According to Tiwari et al. [9], the metabolites are 50% more toxic than the parental compounds. Worse still, these metabolites are persistent due to their high mobility and weaker sorption potential. Concerns have arisen over the past decades because of their frequent detection in the environment and their toxicological effects [6]. They have been detected at concentrations varying from ng/L to µg/L in drinking water, surface water, groundwater, and wastewater worldwide [3,8,10]. These emerging contaminants are released into the environment via treated or untreated wastewater from municipal [10], discharge from hospital wastewater [11], effluent from sewage treatment plants [2,12], industrial wastewater, improper disposal of unused or expired medicine [8,13], surface run-off from urban or agricultural areas [10,14] and pit latrines in developing countries [13,15]. Other potential sources of contamination are pharmaceuticals used in veterinary medicine, which are excreted on the ground or directly into surface waters [14,16]. Figure 1.1 shows a summary of these pathways. Although these contaminants are present at low concentration levels, they deteriorate the quality of water, and the continuous discharge and chronic exposure to these chemicals pose a health risk to humans, animals, and aquatic organisms [4,9,16,17]. Other adverse effects caused by pharmaceutical pollution include endocrine disruption, genotoxicity, and the development of resistant pathogenic bacteria [4]. Among the numerous emerging pollutants, anti-retroviral drugs are also of major environmental concern given that South Africa uses more of these compounds per year compared to any other nation worldwide. They are used in the fight against HIV/AIDS and several reports have confirmed their presence in the environment [5,13,18,19].

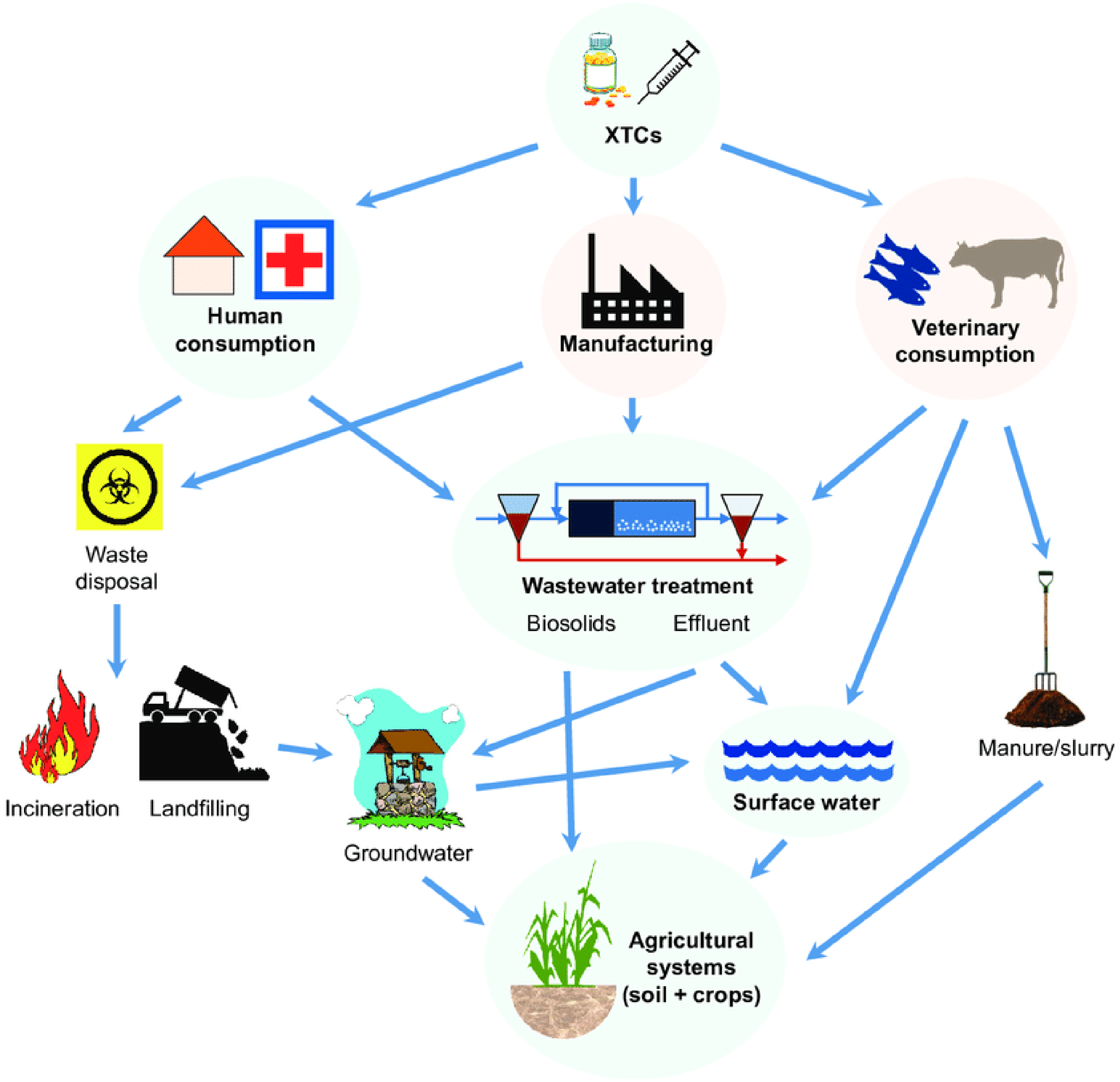

Figure 1. 1. Summary of the major sources of pharmaceuticals contaminants [20]

1.2 Background on HIV

South Africa has the highest number of people living with the Human Immunodeficiency Virus (HIV), with an estimated total of 8.2 million people in 2021 [21]. HIV is a retrovirus that attacks CD4+ helper lymphocytes that are responsible for the body's immune system. If left untreated, HIV decreases the number of CD4 cells in the body, making it harder for the body to fight off infections. The most severe phase of HIV infection is acquired immunodeficiency syndrome (AIDS), which develops when an HIV patient has a CD4 cell count of below 200 cells/mm. This suppresses the immune system and leaves it susceptible to opportunistic infections [22,23].

1.2.1 HIV Treatment

Unfortunately, there is no cure for HIV. Medications that are used for the treatment of retroviral infections, such as HIV type 1, are known as antiretroviral drugs (ARVs). These drugs do not necessarily kill the virus, but instead, they slow its replication process [19]. ARVs have been classified into about six different groups depending on their mode of action as well as which phase of the HIV life cycle they target. These classes include nucleoside reverse transcriptase inhibitors (NRTIs), non-nucleoside reverse transcriptase inhibitors (NNRTIs), protease inhibitors (PI), integrase inhibitors, entry and fusion inhibitors, and CYP450-3A inhibitors. Figure 1.2 shows the life cycle of the HIV and the ARVs sites of action. The first drug used for treatment in 1987 was zidovudine, a NRTI [24,25]. However, it was not very effective, so scientists decided to combine this drug with the reverse transcriptase inhibitors didanosine and zalcitabine. This combination showed great improvement. Nevertheless, this victory was short-lived because patients developed drug resistance [26]. Therefore, there was an urgent need to develop other forms of drugs that would be more effective by delaying the occurrence of drug resistance, reducing death rates, and being less toxic. Combination antiviral therapy was then put into place to prevent the multiplication of the virus at different stages of its life cycle. The triple combination method, also known as highly active antiretroviral therapy (HAART), has been proven to be highly active against the virus [19]. Because of the high mutation rate of HIV, which produces viral offspring resistant to a certain drug, using HAART would suppress the replication of a mutant, as it is highly unlikely that the mutant would be resistant to all three drugs at the same time [19,27]. HAART significantly reduced viral replication and viral load to levels below detection. This generally improved one's immune system, as well as increased their life expectancy [28]. Despite their effectiveness in dealing with the pandemic, some of these drugs are not completely metabolised by cytochrome P450 isozymes and hence are excreted in urine [29]. Sadly, these are finding their way into water sources, leading to contamination. Some of these ARVs are known to be persistent, bio- accumulative, and exhibit endocrine disruptive behaviour [5]. Nevirapine (NVP) is one of the drugs that has been positively detected in water sources.

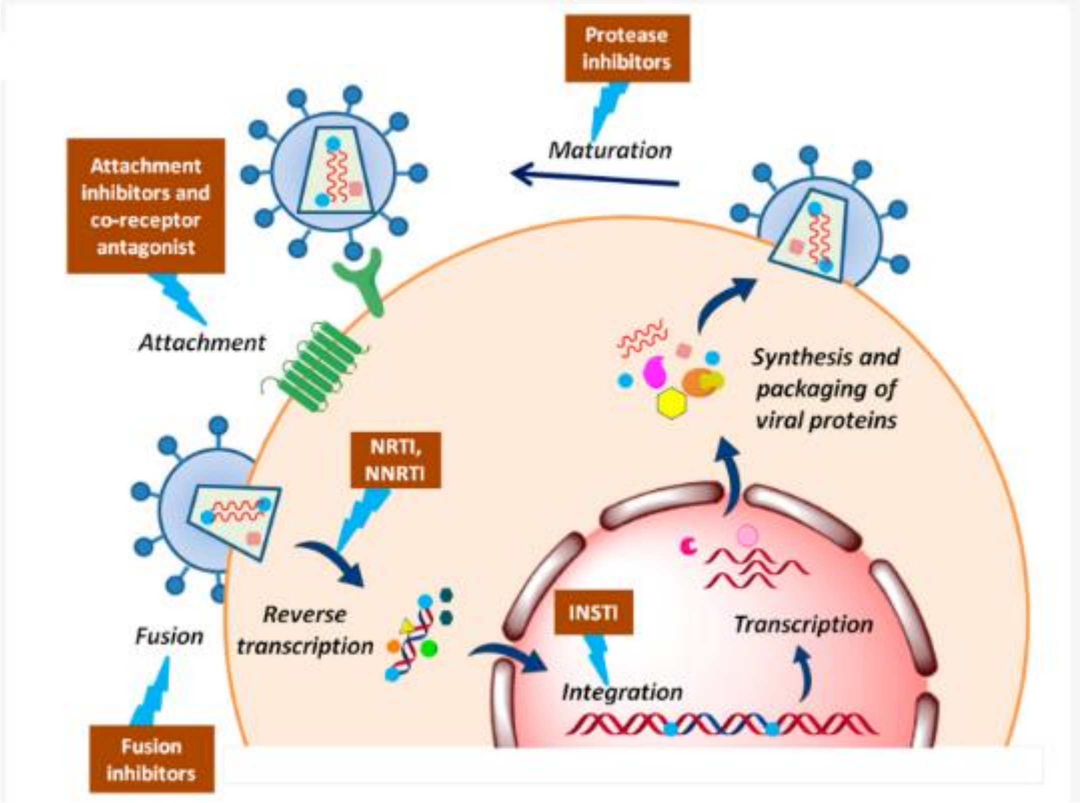

Figure 1. 2. Diagrammatic representation of HIV virus life cycle and ARVs targets [30]

1.2.2 Nevirapine

Nevirapine is a non-nucleoside reverse transcriptase inhibitor (NNRTI) whose chemical name is 11-cyclopropyl-5,11-dihydro-4-methyl-6H-dipyrido[3,2-b;2',3'-e][1,4]diazepin-6-one [31]. It was the first NNRTI to be used for the treatment of HIV infection in 1997 and the prevention of mother-to-child transmission. It can be used as a component of combination therapy. For example, it is usually used as a substitute for efavirenz in Atripla, a fixed-dose pill prescribed for a person who has just tested positive for the virus. Nevirapine is readily absorbed when given orally, with a bioavailability of 90% [19]. The drug is a non-competitive inhibitor. It binds directly to the enzyme reverse transcriptase and distorts its active site, which then prevents DNA polymerase from carrying out its function [27]. It restricts the enzyme's capacity to change conformation, resulting in increased enzyme rigidity and reducing the enzyme's polymerisation function [32]. CYP3A4 oxidatively metabolises nevirapine to several hydroxylated products, such as 2-, 3-, 8-, and 12- hydroxynevirapine which may be further glucuronidated before excretion [33]. These metabolites are illustrated in Figure 1.3. Nevirapine can reduce the viral load, increase the CD4 cell count, and overall reduce one's risk of developing AIDS. However, the use of this drug presents some negative effects, which include severe skin rashes, hepatitis, and a skin disorder called Stevens-Johnson syndrome. According to the findings of in vitro studies, 12-hydroxynevirapine has been suggested to be the causative agent of nevirapine toxicity [33].

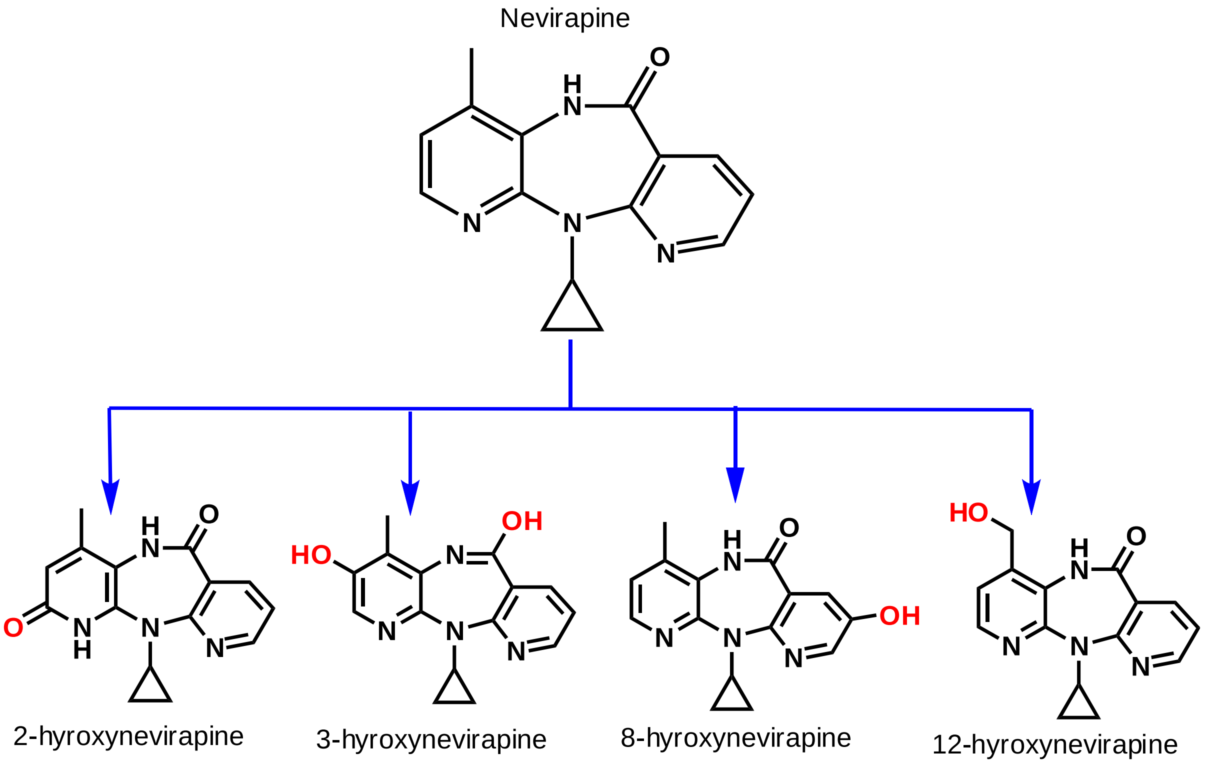

Figure 1. 3. Schematic diagram showing nevirapine and its metabolites

Regardless of the success of nevirapine in reducing the detrimental effects of HIV, its stable chemical structure makes it difficult to be fully degraded by the metabolic systems. Hence, the parent drug and its metabolites are excreted through urine or faeces into the water systems [5]. Other sources of these contaminants include incorrect disposal of unused or expired products; discharge from hospitals; effluents from wastewater treatment plants (WWTPs); discharge from pharmaceutical industries; and the disposal of waste from research institutions. Due to the increase in the amount of nevirapine detected in drinking water because of the inability to remove it at wastewater treatment plants, it has raised a lot of concern regarding people's health [18]. Thus, nevirapine is one of these emerging contaminants that has been reported to be present in most water sources in South Africa. According to Schoeman et al. [5], approximately 2.7% of nevirapine is excreted via urine. The persistence of this drug in the environment is attributed to its non-biodegradable nature. Their presence in water poses a health risk to both humans and aquatic organisms. Some of the dangers of consuming contaminated water include falling sick, suffering from side effects of ARVs or other pharmaceuticals, and, in the long run, developing drug resistance. Unfortunately, WWTPs were never designed to remove these contaminants from water, which explains why they are still present in water sources [5,19]. Schoeman et al. [5] reported nevirapine effluent concentrations ranging from 92 ng/L to 473 ng/L from a WWTP in Gauteng, with a removal efficiency of 22.5%. The concentration of NVP was observed to increase at the different stages of purification in the WWTP. This was attributed to the de-conjugation of the hydroxylated metabolites of NVP, the lack of binding of NVP to the primary settling tank (PST) sludge and the compounds' resistance to degradation [5]. The inability of NVP to be removed from the activated sludge in WWTPs may be a result of its photostability and low biodegradability [34]. Abafe et al. [18] obtained an effluent concentration of 1400 ng/L from Phoenix WWTP in KwaZulu-Natal, South Africa.

1.3 Problem statement and motivation

Less than 1% of the 3% of available freshwater is suitable for human consumption. Regrettably, this small amount of freshwater is prone to heavy pollution from various industries [35]. Pharmaceutical and personal care product pollutants are one of the major emerging contaminants that require great attention. Antiretroviral drugs, such as nevirapine, are pharmaceutical drugs used in the treatment of HIV/AIDS [25]. Nevirapine is an antiretroviral drug that is prescribed for the primary treatment of HIV/AIDS patients. South Africa has been reported to have the highest number of people living with HIV/AIDS. Pregnant mothers who are infected with the virus are given this medication throughout pregnancy to prevent mother-to-child transmission. Newly born babies are also given this medication in syrup form, while much older children receive it in pill form [36–38]. Nevirapine has been detected most frequently in water sources where it might cause significant problems, such as the formation of degradation products that have similar effects to the pure drug itself [5,13,19]. Side effects of this drug include hepatotoxicity, hypersensitivity, and the development of skin rashes. Chromatographic methods have been employed in the past to detect and quantify these drugs in water, but their high cost, lengthy analysis time, sophisticated equipment required, and generally lower detection limits create a significant need for improving existing detection techniques. The limit of detection for nevirapine in wastewater samples was determined to be 6 ng/mL when LC-MS/MS was employed, compared to 1.8 ng/L when GC-MS was utilised. Since these antiviral drugs are found at concentrations in the ng/L range, there is a need for the development of sensor systems that can detect their presence at even lower concentrations than previously reported, are simple to operate, provide rapid responses, and are constructed from readily available materials [18,39–41].

The incorporation of $NiSe_2$ quantum dots into the sensor system to enhance the electrocatalytic response of the gold electrode in the detection of nevirapine in water is proposed. The unique properties and several synthesis routes of $NiSe_2$ quantum dots are discussed thoroughly in chapter 2. Quantum dots (QD) are incorporated into sensing devices to improve their sensing capabilities by rapidly producing an accurate signal. As a result, a more efficient and reliable sensor device is created. The superior structural, optical, and electronic properties of semiconducting materials such as quantum dots have attracted the attention of many researchers over the past decades. They have found great application in a wide range of fields, both in biological and inorganic material systems. In comparison to organic dyes employed in the construction of sensors, QD have several benefits, including high photobleaching thresholds, brightness, long fluorescence lifespan, tunable bandgap, and excellent photostability. Their small size range imparts them with a higher surface area to volume ratio, which gives them superior properties compared to the bulk materials [42–45]. In an effort to replace the use of toxic quantum dots such as cadmium, mercury, and lead, $NiSe_2$ quantum dots are proposed together with the use of greener stabilising agents [46,47]

Stabilising agents, also known as capping agents, are very important because they influence both the physical and chemical properties of the quantum dots. They also aid in the stability, solubility, and reduction of toxicity of the materials. Additionally, capping agents prevent nanocrystals from aggregating. Examples of capping agents that have been widely used include 3-mercaptopropionic acid (3-MPA), thioglycolic acid (TGA) and glutathione (GSH), to mention a few [48,49]. Since the integration of green synthesis principles is of great importance in the field of nanotechnology nowadays, the use of naturally occurring organisms such as fungi, bacteria, and yeast has been applied during the synthesis of nanoparticles in an effort to produce quantum dots in an eco-friendly manner. Extracts from various parts of plants have also been used, including rose plant extracts, orange peels, chitosan, castor oil, and banana extracts, to mention a few. The use of banana peel extract and 3-MPA is proposed for this project. This fruit is available all year round. Although a few applications for banana peels have been investigated, including their use as adsorbents of heavy metals, medicinal purposes, ethanol fermentation, and production of fungal biomass, this still leaves a massive amount of waste material available. New applications of these peels still need to be explored to reduce the amount of waste [50–52]. The banana peel is rich in amine, hydroxyl, and carboxylic acid functional groups, which act as capping agents during quantum dot synthesis. It is also rich in phytochemical compounds and polysaccharides, and it is a good source of natural antioxidants. The extraction method is quite simple [53]. This extract would act as a solution to produce environmentally friendly, functionalised quantum dots. Functionalisation allows for early and rapid detection of the target analyte. Sensors that have been used in determining the presence of nevirapine include uracil/carbon paste electrodes, mercury/carbon paste electrodes, glassy carbon electrodes, and copper oxide-carbon nanoparticle/glassy carbon electrodes, to mention a few. They proved to be very accurate, with a high degree of sensitivity and stability. However, these sensors were primarily used to detect the presence of nevirapine in pharmaceutical, urine, or serum samples [40,54,55]. Therefore, it would be good if the application of these sensors could be expanded to wastewater. Nickel selenide nanomaterials, on the other hand, have been used as electrocatalysts in hydrogen evolution reactions, oxygen evolution reactions, dye-sensitized solar cells, and energy storage materials. Their excellent performance and impressive stability give us confidence in their application as electrocatalysts in this project [56]. To also check the specificity or selectivity of the modified sensor, some interference studies will be conducted by adding other kinds of drugs to the solution and noting how the signal of nevirapine is affected. In our study, a gold electrode drop-casted with nickel selenide quantum dots ($NiSe_2QD$) will be used for the detection of nevirapine drug in a phosphate buffer solution and simulated water samples. The gold electrode was chosen for this study because of its biocompatibility, high conductivity, high corrosion resistance and good mechanical properties [57,58].

1.4 Aim and objectives of the study

The main aim of this project is to develop an electrochemical sensor based on the incorporation of $NiSe_2QD$ onto a gold electrode for the determination of nevirapine drug in water.

The objectives of the study are :

- Synthesis of $NiSe_2QD$ using banana peel extract (BPE) and 3-mercaptopropionic acid (3-MPA) as capping agents.

- Characterisation of the synthesised materials using techniques such as HR-SEM-EDX, HR-TEM, and SAXS for morphological studies, UV-Vis for optical properties, FTIR and Raman Spectroscopy for functional group vibration studies, DPV for electrochemical studies and XRD for crystalline studies.
- Surface modification of gold electrode with L-cysteine to form a self-assembled monolayer, followed by depositing 3-MPA-$NiSe_2$QD.
- Surface modification of bare gold electrode with BPE-$NiSe_2$QD and then followed by Nafion. Determination of the electrochemical properties of the quantum dots using differential pulse voltammetry.
- Development, control experiments (pH, scan rate studies, interference, stability), evaluation and testing of the electrochemical sensor systems in the absence and presence of nevirapine.
- Analysis of nevirapine in wastewater samples.

1.5 Thesis outline

The study consists of **six chapters**

Chapter 1: Introduction; this chapter gives a brief background on HIV/AIDS and the anti-retroviral drugs used for the treatment of HIV-positive persons. It also explores the presence of pharmaceuticals in water as well as their detrimental impacts. This chapter also presents the problem statement and motivation, aim and objectives, and the outline of the thesis.

Chapter 2: Literature review; this chapter discusses recent research that is relevant to this study. It covers a brief discussion on different electrochemical sensors, the numerous synthesis methods utilised in QD synthesis, and nickel selenide applications.

Chapter 3: Methodology and Instrumentation; this chapter gives a brief overview of the techniques used to characterise the QD. The techniques used include High-resolution transmission microscopy and small-angle X-ray scattering for particle size and internal structure analysis, High-resolution scanning electron microscopy and Energy-dispersive X-ray spectroscopy for surface morphology and elemental analysis, Ultraviolet-visible spectrometry and Photoluminescence for optical studies, X-ray diffraction for crystallinity studies, Fourier transform infrared spectroscopy and Raman spectroscopy for functional group analysis and vibrational studies and Differential pulse voltammetry for electrochemistry studies. In addition, the synthesis procedure for 3-MPA-$NiSe_2$QD and BPE-$NiSe_2$QD is described as well as the fabrication of the sensor.

Chapter 4: This chapter presents the data obtained on the characterisation of 3MPA-$NiSe_2$QD and its individual components using UV-Vis, FTIR, SAXS, Raman, SEM-EDX, HR-TEM, PL, XRD and DPV. The electrochemical response of 3MPA-$NiSe_2$QD/L-cyst/Au to nevirapine was explored.

Chapter 5:The use of a binder known as Nafion to stabilise the BPE-$NiSe_2$QD on the electrode is described in this chapter. These QD were characterised using a variety of techniques including FTIR, SAXS, UV-Vis, PL, Raman, XRD, HR-TEM/EDX, and HR-SEM. DPV was used to investigate the electrocatalytic properties of the developed electrochemical sensor, Au/BPE-$NiSe_2$QD/Nafion, to determine its response to nevirapine.

Chapter 6: This chapter draws conclusions from the overall findings of the research study and makes recommendations for future work.

References

1. J. F. Narváez V. and C. Jiménez C., VITAE, Rev. La Fac. Química Farm. **19**, 93 (2012).
2. P. Bottoni, S. Caroli, and A. B. Caracciolo, Toxicol. Environ. Chem. **92**, 549 (2010).
3. K. O. K'oreje, F. J. Kandie, L. Vergeynst, M. A. Abira, H. Van Langenhove, M. Okoth, and K. Demeestere, Sci. Total Environ. **637–638**, 336 (2018).
4. F. Yuan, C. Hu, X. Hu, J. Qu, and M. Yang, Water Res. **43**, 1766 (2009).
5. C. Schoeman, M. Dlamini, and O. J. Okonkwo, Emerg. Contam. **3**, 95 (2017).
6. T. aus der Beek, F.-A. Weber, A. Bergmann, S. Hickmann, I. Ebert, A. Hein, and A. Küster, Environ. Toxicol. Chem. **35**, 823 (2016).
7. C. G. Daughton and I. S. Ruhoy, Environ. Toxicol. Chem. **28**, 2495 (2009).
8. R. López-Serna, M. Petrović, and D. Barceló, Sci. Total Environ. **440**, 280 (2012).
9. B. Tiwari, B. Sellamuthu, Y. Ouarda, P. Drogui, R. D. Tyagi, and G. Buelna, Bioresour. Technol. **224**, 1 (2017).
10. N. H. Tran, M. Reinhard, and K. Y. H. Gin, Water Res. **133**, 182 (2018).
11. H. A. Duong, N. H. Pham, H. T. Nguyen, T. T. Hoang, H. V. Pham, V. C. Pham, M. Berg,

W. Giger, and A. C. Alder, Chemosphere **72**, 968 (2008).

12. J. P. S. Sidhu, W. Ahmed, W. Gernjak, R. Aryal, D. McCarthy, A. Palmer, P. Kolotelo, and S. Toze, Sci. Total Environ. **463–464**, 488 (2013).

13. T. P. Wood, C. S. J. Duvenage, and E. Rohwer, Environ. Pollut. **199**, 235 (2015).

14. N. Kemper, Ecol. Indic. **8**, 1 (2008).

15. J. P. Graham and M. L. Polizzotto, Environ. Health Perspect. **121**, 521 (2013).

16. J. Rivera-Utrilla, M. Sánchez-Polo, M. Á. Ferro-García, G. Prados-Joya, and R. Ocampo-Pérez, Chemosphere **93**, 1268 (2013).

17. O. A. Jones, J. N. Lester, and N. Voulvoulis, Trends Biotechnol. **23**, 163 (2005).

18. O. A. Abafe, J. Späth, J. Fick, S. Jansson, C. Buckley, A. Stark, B. Pietruschka, and B. S. Martincigh, Chemosphere **200**, 660 (2018).

19. S. Ncube, L. M. Madikizela, L. Chimuka, and M. M. Nindi, Water Res. **145**, 231 (2018).

20. F. Polesel, Modelling the Fate of Xenobiotic Trace Chemicals via Wastewater Treatment and Agricultural Resource Reuse, 2016.

21. Statistics South Africa (Stats SA), Mid-Year Population Estimates 2021 (2021), p. 35.

22. C. A. Andrews' and R. A. Koup, The Immunopathology of HIV Infection (1996).

23. M. Ratnam, A. S. Nayyar, D. Santhosh Reddy, B. Ruparani, K. V. Chalapathi, and S. Azmi, J. Oral Maxillofac. Pathol. **22**, 282 (2018).

24. A. Wlodawer and J. Vondrasek, Inhibitors of HIV-1 protease*:* A Major Success of Structure-Assisted Drug Design 1 (1998).

25. E. De Clercq, Curr. Opin. Pharmacol. **10**, 507 (2010).

26. H. Jablonowski, J Acquir Immune Defic Syndr Hum Retrovirol **10**, S52 (1995).

27. M. M. Zdanowicz, Am. J. Pharm. Educ. **70**, (2006).

28. E. J. Arts and D. J. Hazuda, Cold Spring Harb. Perspect. Med. **2**, (2012).

29. P. Riska, M. Lamson, T. MacGregor, J. Sabo, S. Hattox, J. Pav, and J. Keirns, Drug Metab. Dispos. **27**, (1999).

30. E. Shukla and R. Chauhan, Cells **8**, 1155 (2019).

31. S. Halde, A. Mungantiwar, and M. Chintamaneni, Indian J. Pharm. Sci. **73**, 416 (2011).

32. J. Wongtrakul, A. Paemanee, P. Wintachai, C. Thepparit, S. Roytrakul, T. Thongtan, K. Janphen, K. Supparatpinyo, and D. R. Smith, Asian Pac. J. Trop. Med. **9**, 547 (2016).

33. P. Fan-Havard, Z. Liu, M. Chou, Y. Ling, A. Barrail-Tran, D. W. Haas, and A. M. Taburet, Antimicrob. Agents Chemother. **57**, 2154 (2013).

34. C. Nannou, A. Ofrydopoulou, E. Evgenidou, D. Heath, E. Heath, and D. Lambropoulou, Sci. Total Environ. **699**, 134322 (2020).

35. Z. Wang, A. Wu, L. Colombi Ciacchi, G. Wei, Z. Wang, A. Wu, L. Colombi Ciacchi, and G. Wei, Nanomaterials **8**, 65 (2018).

36. G. M. Anabwani, E. A. Woldetsadik, and M. W. Kline, Semin. Pediatr. Infect. Dis. **16**, 116 (2005).

37. L. A. Guay, P. Musoke, T. Fleming, D. Bagenda, M. Allen, C. Nakabiito, J. Sherman, P. Bakaki, C. Ducar, M. Deseyve, L. Emel, M. Mirochnick, M. G. Fowler, L. Mofenson, P. Miotti, K. Dransfield, D. Bray, F. Mmiro, and J. B. Jackson, Lancet **354**, 795 (1999).

38. E. M. Stringer, M. Sinkala, J. S. Stringer, E. Mzyece, I. Makuka, R. L. Goldenberg, P. Kwape, M. Chilufya, and S. H. Vermund, AIDS **17**, 1377 (2003).

39. O. J. Schoeman, C., Mashiane, M., Dlamini, M. and Okonkwo, Chromatogr. Sep. Tech. **6**, 272 (2015).

40. P. Tiwari, N. R. Nirala, and R. Prakash, ChemistrySelect **3**, 5341 (2018).

41. C. Prasse, M. P. Schlüsener, R. Schulz, and T. A. Ternes, Environ. Sci. Technol. **44**, 1728 (2010).

42. U. Feleni, U. Sidwaba, H. Makelane, and E. Iwuoha, J. Nanosci. Nanotechnol. **19**, 1 (2019).

43. D. Bera, L. Qian, T. K. Tseng, and P. H. Holloway, Materials (Basel). **3**, 2260 (2010).

44. R. E. Galian and M. de la Guardia, TrAC Trends Anal. Chem. **28**, 279 (2009).

45. L. Q. and X. Peng*, J. Am. Chem. Soc. **124**, 2049 (2002).

46. P. Mulpur, T. M. Rattan, and V. Kamisetti, J. Nanosci. **2013**, 1 (2013).

47. K. Guo, F. Yang, S. Cui, W. Chen, and L. Mi, R. Soc. Chem. Adv. **6**, 46523 (2016).

48. Deepika1, S. S. Rakesh Dhar1, and Atul Kumar, Bull. Mater. Sci **38**, 1247 (2015).

49. S. J. Mirnajafizadeh F., Int. J. Adv. Sci. Eng. Technol. **6**, 56 (2018).

50. H. M. M. Ibrahim, J. Radiat. Res. Appl. Sci. **8**, 265 (2015).

51. G. K. Deokar and A. G. Ingale, RSC Adv. **6**, 74620 (2016).

52. J. S. Waghmare and A. H. Kurhade, Pelagia Res. Libr. Eur. J. Exp. Biol. **4**, 10 (2014).

53. H. Zheng and L. Wang, Soft Nanosci. Lett. **3**, 29 (2013).

54. S. Shahrokhian, R. Kohansal, M. Ghalkhani, and M. K. Amini, Electroanalysis **27**, 1989 (2015).

55. F. Zhang, L. Li, L. Luo, Y. Ding, and X. Liu, J. Appl. Electrochem. **43**, 263 (2013).

56. F. Wang, Y. Li, T. A. Shifa, K. Liu, F. Wang, Z. Wang, P. Xu, Q. Wang, and J. He, Angew. Chemie Int. Ed. **55**, 6919 (2016).

57. M. Vafaiee, M. Vossoughi, R. Mohammadpour, and P. Sasanpour, Sci. Rep. **9**, 1 (2019).

58. M. M. Collinson, ISRN Anal. Chem. **2013**, 1 (2013).

CHAPTER TWO

ELECTROCATALYSIS AND SENSOR APPLICATIONS OF NICKEL SELENIDE QUANTUM DOTS

Summary

This chapter discusses recent research that is relevant to this study. It includes a brief discussion on different electrochemical sensors and the numerous synthesis methods utilised in QD synthesis. It also covers nickel selenide applications and includes brief information on traditional detection methods and several electrochemical sensors that have been previously utilised to detect nevirapine.

2.1 Introduction

Sensors are widely used in our everyday lives. A sensor is an intelligent device that produces a measurable change in its output in response to a stimulus. Sensors are also transducers; they convert the input stimulus into an electrical or another form of output signal that can be processed. The stimulus can either be physical or chemical [1–3]. Nowadays, common sensors convert the measurement into electrical signals. There are many different types of sensors worldwide. However, according to Hunter et al. [2], a sensor can be described from the perspective of the target measurement, for example, a pressure sensor, or from the platform point of view, for example, an electronic sensor. Some types of sensors include magnetic, thermal, chemical, and radiant sensors, to mention a few. Chemical sensors, in particular, can be categorised as optical, electrical, electrochemical, piezoelectric, or other types based on the operation principle of the transducers [4].

Electrochemical sensors are a rapidly growing field of chemical sensors. They are a powerful analytical tool for real-time analysis. Electrochemical sensor systems provide sample analysis tools that are simple, fast, sensitive, selective, precise and easy to use [1,5,6]. Unfortunately, these electrochemical sensors have some limitations. Specifically, the issue of interferants interacting with modified electrodes hinders their commercialisation. Electrochemical sensors operate on the principle of changes in electrical current or potential caused by chemical reactions. They convert the information associated with the electrochemical reaction into a quantitative or qualitative signal. The signal obtained is proportional to the analyte concentration. The most common design of electrochemical sensors consists of a three-electrode conformation with a working electrode (WE) acting as an anode, a counter electrode (CE) functioning as the cathode, and a reference electrode (RE) for controlling the potential of the system [7]. More practically, the target analyte reacts on the WE, resulting in a current generated between the working and counter electrodes. Additionally, the generated current is proportional to the number of reaction sites present on the WE and the analyte concentration [8]. A simplified diagram illustrating the working principle of these electrochemical sensors is shown in Figure 2.1.

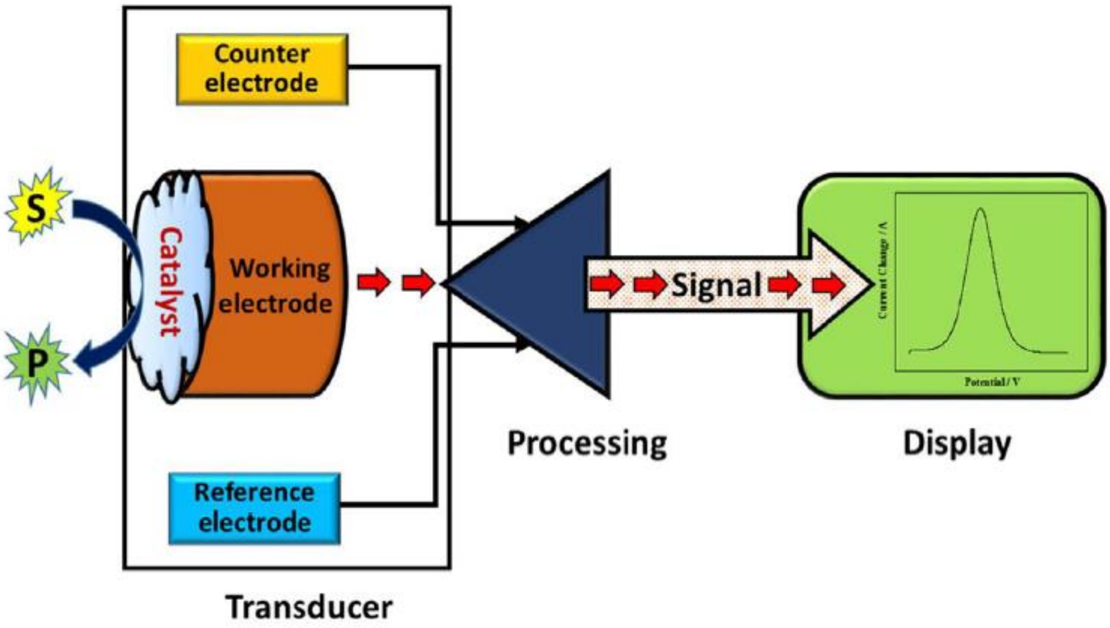

Figure 2. 1. Schematic diagram showing the working principle of electrochemical sensors [9].

2.1.1 Modified electrochemical sensors

The performance of sensors is influenced by the properties of the WE, and a lot of effort has been devoted to the fabrication and maintenance of the electrodes. Electrochemical sensors based on biological components, biosensors, are constrained by the conditions at which the biological components are stable [7]. These biosensors have great selectivity and sensitivity but they also have drawbacks like short shelf life, high production costs, low reproducibility, and repeatability [10]. The incorporation of nanomaterials into electrochemical sensors has had a significant impact on their development, mostly due to the surface-to-volume ratio, one of the most distinctive characteristics of nanometric order. Various nanomaterials have been textured onto the surface of the working electrodes, resulting in an increase in the surface area and redox reaction sites. As a result, improved detection limits and increased signal-to-noise rations have been obtained [4,8,11]. Quantum dots (QD) are a type of nanoparticles that have been widely employed to modify electrodes for sensor applications.

2.2 Introduction to Quantum dots

Quantum dots are nanoparticles with sizes ranging from 2 to 10 nm. Due to their small size, they exhibit unique optical and electrical properties that are distinct from those of bulk materials. They are distinguished from bulk matter by their high surface area to volume ratio and adjustable bandgap caused by quantum confinement phenomena. Their small sizes cause the energy levels of the different bands to be quantized in relation to the size of the dot. As the size of the QD decreases, the bandgap increases, requiring more energy to excite electrons from the valence band to the conduction band [12–14]. QD exhibit exceptional photo luminescent properties. They are used in a wide variety of disciplines, including energy, electrochemical sensors, polymers, and medical diagnostics, to name a few [15–17].

2.2.1 Synthesis of quantum dots

Several synthetic routes have been used in the synthesis of quantum dots. Any metal and chalcogenide (sulphur, selenium, tellurium) can be used to make QD. These chalcogenides include. The existing methods can be generally divided into the top-down or bottom-up approaches, which will be discussed briefly. The top-down approach entails decreasing the size of the bulk material to obtain the desired nanosized particles. The top-down methods are conditioned and fabricated by external parameters to create nanoparticles with the desired shapes and sizes from the bulk material. This method includes techniques such as molecular beam epitaxy, electron beam lithography, ion implantation, and x-ray lithography. The major shortcomings of this approach are structural imperfections caused by patterning and impurity incorporation into the QD [14,18,19]. The alternative bottom-up approach refers to the synthesis of nanomaterials by exploiting the physics and chemistry to artificially assemble the atoms and molecules into nanoparticle clusters [20]. This approach employs a variety of self-assembly techniques that can be broadly classified as vapour-phase or chemical.

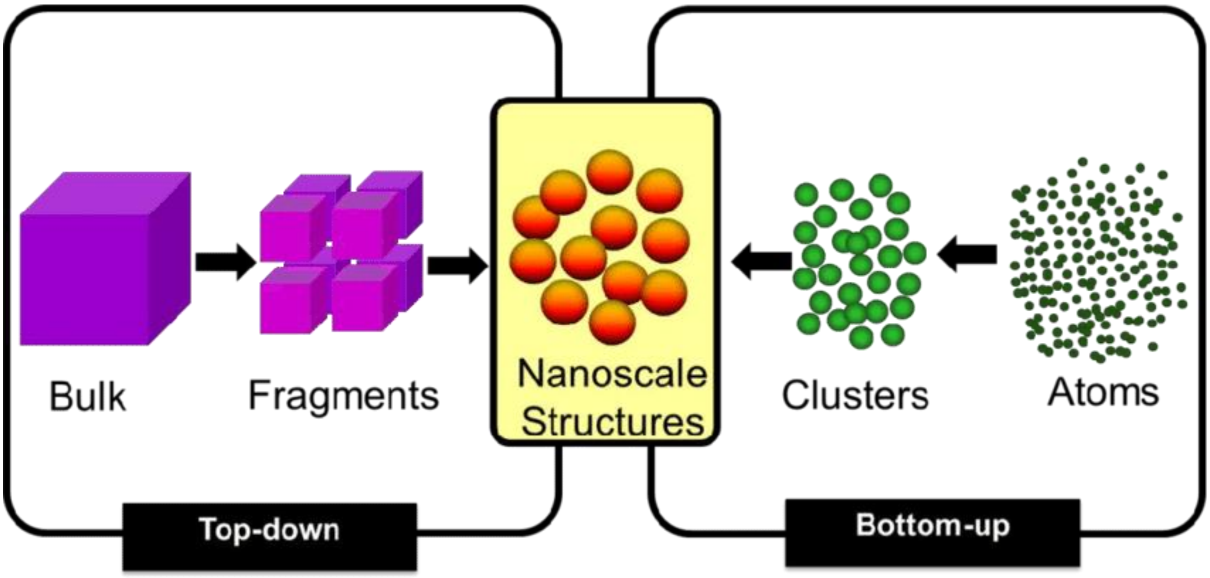

Figure 2. 2. Simplified representation of the top-down and bottom-up synthesis routes for nanostructures [21].

2.2.2 Vapour-phase methods

These vapour-phase methods for producing quantum dots begin with the growth of layers in an atom-by-atom process. Consequently, QD self-assembly on a substrate without any patterning [14,18]. Chemical vapour deposition is another technique for generating thin films from which QD can be self-assembled. Physical vapour deposition layer growth occurs when a solid condenses from vapours generated by thermal evaporation or sputtering. While the above-mentioned methods, among others, are effective in QD synthesis without the need for a template, QD size fluctuation frequently results in inhomogeneous optoelectronic properties [14].

2.2.3 Chemical methods

Chemical methods are mostly based on standard precipitation techniques with precise parameter control for the solution(s). Thus, the precipitation process consists of a nucleation stage followed by particle growth stages. Some of these methods of preparation, such as colloidal and aqueous phase synthesis, will be briefly discussed. Other synthesis processes, such as solvothermal, heating, hydrothermal, and microwave irradiation, will have their properties outlined in Table 2.1 [14,18]. It is critical to note, however, that due to the large variety of potential preparation methods, the right method of synthesis that results in QD with the desired properties must be chosen based on the attributes required for the application [22].

2.2.3.1 Colloidal synthesis of quantum dots

QD synthesis using this route involves the use of an organic or inorganic solvent during a chemical reaction. The resulting QD will be suspended in solution. During the organometallic synthesis, metallic or organometallic precursors and the chalcogenide are rapidly injected into a hot solution containing a coordinating organic solvent such as trioctylphosphine (TOP) or tri-n-octylphosphine oxide (TOPO). The QD begin nucleating immediately after the injection of the precursors. In general, these QD are formed at high temperatures in the range of 180 and 310 ℃ [13,23,24]. The size of the QD is mainly controlled by the chosen temperature and the reaction time. Therefore, aliquots may be removed at regular intervals and then exposed to spectroscopic studies to monitor the size of the particles [13,23]. Once the desired size of the QD has been achieved, the temperature of the reaction is dropped to stop the reaction. Colloidal formation of QD at high temperatures is known as “hot injection”. The coordinating solvents enhance the surface passivation, stabilise the QD, prevent their agglomeration, and provide an adsorption barrier to slow QD growth [14]. An advantage of this method is that it produces highly monodispersed and crystalline QD [23]. Several disadvantages of this method include the production of hydrophobic QD with limited applications, the use of toxic solvents or precursors, the high associated with the use of high temperatures and generally poor water dispersion [13,14]. Nevertheless, several strategies have been employed to make hydrophilic QD in aqueous solvents for possible biological applications. Some of these strategies include silica encapsulation, encapsulation of QD into the core of phospholipid block-copolymers, and ligand exchange with bi-functional compounds, with a functional group that can attach to the QD surface (e.g., thiols), and a hydrophilic group such as carboxylic acid [23,25].

2.2.3.2 Aqueous phase synthesis of quantum dots

Aqueous synthesis offers a simpler, less toxic, and cheaper alternative to the previously mentioned synthesis methods that use high-boiling point organic solvents and organometallic precursors [25–28]. The quantum dots are prepared directly in water, resulting in water-soluble quantum dots. The synthesis process uses water-soluble precursors such as metal nitrates or chlorides. The most commonly used chalcogen precursors are NaHSe (formed by reacting Se powder with sodium borohydride ($NaBH_4$) but variations such as Na_2SO_3 are also used [13,25]. The synthesis of the QD is typically carried out in an inert atmosphere due to the instability of chalcogen sources in ambient conditions. However, this is not the case when compounds like Na_2SO_3 are used as they are air-stable [13,29]. This synthesis route also involves the use of short-chained thiols as stabilising agents. Some of the most commonly used ligands with both sulfhydryl and carboxyl functional groups are L-cysteine (L-cyst), 3-mercaptopropionic acid (3-MPA), and glutathione (GSH) [13,25,28,30]. The sulfhydryl group coordinates with the QD, whilst the carboxyl group contributes to the electrostatic stability of the QD. The carboxyl groups on the surface of the QD also facilitate their attachment to biomolecules such as proteins [13,26]. Moreover, the nucleation reaction occurs rapidly at room temperature and the crystals grow slowly at lower temperatures (~100 ℃) [29]. The temperature, pH of the solution, the concentration of precursors, as well as the reaction time have significant effects on the shape, particle size, and particle size distribution [30]. However, the main disadvantages of this method are poor size distribution and low fluorescence quantum yields. Although aqueous synthesis of nanomaterials has gained momentum over time, there are still many improvements awaited [31,32].

2.2.3.3 Other synthesis methods

Other methods that have been used to synthesise QD include the heating up method, solvothermal, hydrothermal, and microwave irradiation. A summary of the methods' descriptions, advantages, and disadvantages is shown in Table 2.1.

Table 2. 1: Presents a summary of the advantages and disadvantages of different synthetic methods

Synthesis Method	**Description**	**Advantages**	**Disadvantages**	**Ref**
Heating up	This involves the addition of all the reagents to the same pot and steadily heating the mixture to induce nucleation and growth of the QD.	Suitable for large-scale production, reproducibility	High temperatures, organic solvents	[32,33]
Solvothermal	Involves placing reagents into an autoclave filled with organic solvent and	Production of nanoparticles with good crystallinity	Organic solvents, poor control of particle size and shape, low yields	[25,30]

	the synthesis reaction taking place under high pressure and temperature.			
Hydrothermal	It involves heating an aqueous mixture of precursors in an autoclave above the water’s boiling point.	High crystalline nanoparticles, good control of particle size, uniform morphology, high yield	High temperatures and pressure, longer reaction times, special reactor required	[22,34]
Microwave	A mixture of the reagents is transferred to the microwave reaction vial, which is subsequently loaded into a microwave reactor for heating.	Rapid process, instantaneous nucleation and growth of nanoparticles, narrow size distribution, reproducible, less dangerous process, low energy consumption	Low fluorescence quantum yield	[25,33,35]

2.2.3.4 Surface capping agents

Capping agents have been extensively used as stabilisers in the synthesis of nanoparticles. They are of utmost importance as they inhibit nanoparticle overgrowth, prevent their aggregation and regulate their structural properties [36]. The capping agent induces steric or electrostatic interactions between the particles, which contributes to the nanoparticle’s stability [37]. As mentioned in the previous section, short-chained organic compounds have previously been used as capping agents, but plant extracts, dendrimers, polymers, and surfactants have also been reported [38]. Apart from their stabilising properties, they can also be used to enhance the catalytic performance of nanocrystals [36]. However, the use of long-chain hydrocarbons, branched or unbranched polymers, and dendrimers act as a physical barrier, preventing reactants from freely accessing the catalytic active sites on the particle surface [36,39]. Therefore, selecting a suitable capping agent is very crucial. Another way of capping QD involves adding inorganic layers to the surface, forming a core-shell structure. When selecting an inorganic shell material, it is necessary to consider its hydrophobic or hydrophilic nature. The majority of inorganic core/shell QD do not disperse well in water due to the shell's hydrophobic surface. As a result, further modification will be required before the QD may be employed in biological applications [14]. In this study, a short-chained mercapto acid, 3-mercaptopropionic acid (3-MPA), and a plant-derived extract, banana peel extract (BPE), have been used in the synthesis of $NiSe_2$ QD.

2.3 Nickel selenide quantum dot material

Due to their unique optoelectronic properties, stability, and narrow bandgaps, transition metal chalcogenides have been identified as emerging candidates for application in a variety of disciplines [40]. Selenides have a higher electrical conductivity than oxides and sulphides due to selenium's high metallic characteristics. Nickel is significantly less expensive and less toxic than cadmium [40,41]. Nickel and selenium exist in a variety of homogeneous and crystalline phases, including $NiSe_2$, $Ni_{1-x}Se$, and Ni_3Se_2. The rationale for the formation of distinct compounds between these two elements is due to the minor difference in their electronegativity. These p-type semiconductors have a bandgap of 2.0 eV [42,43]. $NiSe_2$QD have excellent thermodynamic stability and electrical conductivity for charge transfer [44–46]. Nickel selenide has a low resistivity and narrow bandgap compared to other chalcogenides, which contributes to its catalytic characteristics [47,48].

2.3.1 Crystal structure models of NiSeQD material

$Ni_{(1-x)}Se$ and NiSe have been reported to exhibit a hexagonal phase. $NiSe_2$ has a cubic crystalline structure, with two Ni atoms flanking Se_2. Ni_3Se_2 has been found to have a rhombohedral phase [41,43,46]. Each corner of the distorted triangular prism is filled with a Ni atom, and six of these atoms surround the Se atom in this configuration. On the other hand, both NiSe and $NiSe_2$ have been reported to have an orthorhombic structure. At ambient temperature, $Ni_{(1-x)}Se$, $NiSe_2$, and Ni_3Se_2 are the most stable states [46]. These phases are depicted in Figure 2.3.

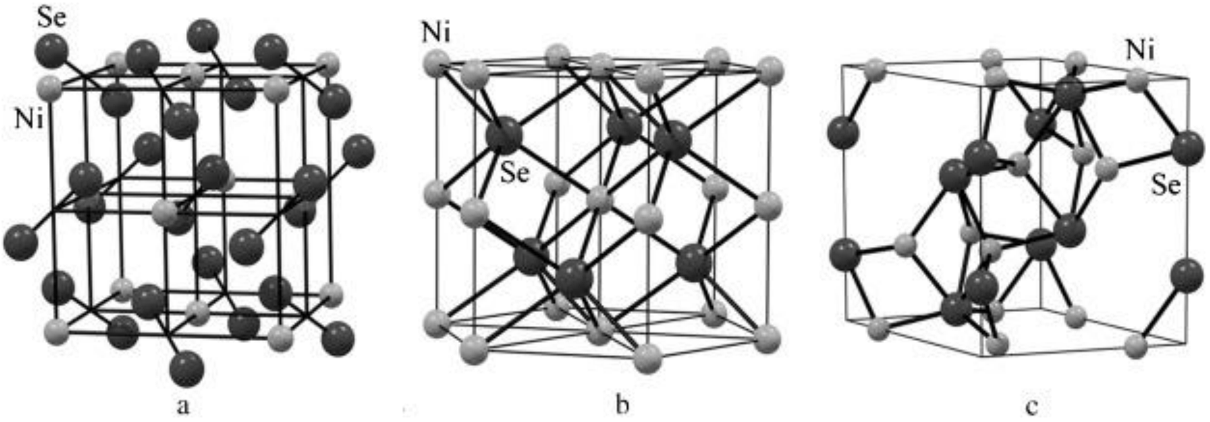

Figure 2. 3. Diagrammatic representation of the crystalline structure of a) $NiSe_2$, b) $Ni_{(1-x)}Se$ and c) Ni_3Se_2 [46].

2.3.2 Synthesis of nickel selenide quantum dots

Numerous synthesis methods have been used to prepare NiSeQD, including colloidal (CoLS) [49], precipitation method [50], hot injection (HI) [51], chemical vapour deposition [42], solvothermal (ST) [52,53], hydrothermal (HT) [54], electrodeposition (ED) [55], solid-state reaction (SSR) [56], chemical bath deposition [57,58], solid-liquid solution methods and (SLS) [59]. The phases of nickel selenide produced are determined by the synthesis routes and the precursors used. Different reaction factors including temperature and pH have been shown to have a considerable impact on the final product [41]. Hussain et al. [41] conducted a comprehensive evaluation of nickel selenide syntheses. Table 2.2 summarises the synthesis methods, stoichiometry, and morphology of different nickel selenide analogues. The literature reports a diversity of surface morphologies, all of which are dependent on the synthesis process and reaction conditions employed. For example, some researchers obtained nanocrystals with a cauliflower shape [60] while others obtained microspheres [46], both of which had a rough surface with numerous pores. Because of the increased surface area and exposure of more active sites, these features improve the electrocatalyst's catalytic efficacy [46,60]. Additionally, nanowires [51,59,61], nanoflower spheres [62], nanorods [49,63], nanoflakes [48], and nanosheets [48,64,65] have been mentioned in the literature.

Table 2. 2: Table details the synthesis methods used for fabricating NiSe with different morphologies using various precursors

Method	**Ni source**	**Se source**	**Temp (°C)**	**Reductant/solvent**	**Product**	**Morphology**	**Ref**

HT	$NiSO_4.7H_2O$	$Na_2SeO_3.5H_2O$	100	H_2O, N_2H_4, EDTA	$Ni_{0.85}Se$	Microspheres	[46]
HT	Nickel foam	Se powder	160	H_2O, ethylenediamine	Ni_3Se_2/NF	Cauliflowers	[60]
HT	Nickel foam	Se powder	160	H_2O, $NaBH_4$	Ni_3Se_2/NF	Nanosheets	[64]
HT	$NiCl_2.6H_2O$	Se powder, g-C_3N_4	160	H_2O, $NaBH_4$	$NiSe_2$/g-C_3N_4	Nanocorals	[66]
HT	$NiCl_2.6H_2O$	Se/C	160	H_2O, N_2H_4	$Ni_{0.85}Se$/C	Nanowires	[67]
HT	Ni acetate	SeO_2	180	Benzyl alcohol	NiSe	Nanorods	[63]
ST	$Ni(NO_3)_2.6H_2O$	SeO_2	180	2-phenylethanol, DMF	$Ni_{0.85}Se$	Nanoflower spheres	[62]
ST	$Ni(NO_3)_2.6H_2O$	SeO_2	180	Glycerol	$Ni_{0.85}Se$	Nanospheres	[52]
ST	$NiCl_2.6H_2O$	Se powder	40	H_2O, $NaBH_4$	NiSe	Spheres	[68]
ST	Nickel foam	Se powder	160	Ethyleneglycol, Ethylenediamine	NiSe/NF	Nanowires	[69]
SSR	Ni powder	Se powder	600	-	Ni_3Se_2	Granular	[41]
ED	$NiSO_4.7H_2O$	$Na_2SeO_3.5HO$	RT	H_2O	$NiSe_2$	Cracked	[70]
SLS	Ni foam	Se powder	180	H_2O, $NaBH_4$	NiSe/NF	Nanowires	[59]
HI	Ni acetate	Na_2SeO_3	120	Ethyleneglycol, NH_2OH	$NiSe_2$	Nanowires	[51]
CoLS	$NiCl_2.6H_2O$	$NiCl_2.6H_2O$	60	H_2O, NH_3	NiSe thin film	Nanorods	[49]

2.3.3 Modification of nickel selenide quantum dots

Nickel is a fairly unstable metal that easily oxidises in solution or at room temperature. As a result, nickel compounds like oxides and hydroxides have been used in various analytical processes because of their exceptional qualities, which include catalytic activity, stability, and synthesis simplicity [71–74]. Selenides have the highest catalytic activity in comparison to sulphides [48,64]. However, it has been found that this catalyst has low electronic conduction, limiting its applicability in alkaline environments [75–77]. To address this issue, a variety of nanomaterials have been added to the NiSe matrix, including carbon nanotubes (CNTs), and nickel foam (NF) [47,75,77–79]. Modification of nanomaterials is critical for increasing the electrical conductivity, stability, agglomeration resistance, and catalytic characteristics of nanomaterials.

The surface layer has a significant impact on the physicochemical properties of NiSe. The agglomeration of nickel selenide nanoparticles reduces the number of active sites that are exposed, lowering the catalyst's catalytic effectiveness. The advantages of modification are increased electrical conductivities [77], catalytic activities [80], stabilities [81] and increased strengths [77]. Hence, modification of the catalyst before using it in various analytical applications is essential.

2.4 General applications of nickel selenide

Electrochemical water splitting is an alternative source of clean and renewable energy production. This process involves two half cells namely the oxygen evolution reaction (OER) and hydrogen evolution reaction (HER). The produced oxygen and hydrogen are used to generate renewable energy. Nickel selenide has been extensively investigated in a variety of applications, such as in electrolysis [82,83], production of hydrogen gas [47,77,81], and supercapacitors [52,84–86]. It has been utilised as an electrocatalyst in the water-splitting reaction due to its high catalytic activity, which is aided by nickel’s strong covalent bonding with selenium [41]. Urea electrooxidation is another environmentally friendly method of generating energy. The application of nickel selenide in HER, OER and urea oxidation will be discussed.

2.4.1 In HER

Hydrogen gas is regarded as a clean fuel carrier and is used in a variety of industries, including food processing and refining [22,76,87–90]. HER efficiently and sustainably produces hydrogen. The production of hydrogen by reducing water is depicted in equation 1.

$$2H^{+} + 2e^{-} \rightleftharpoons H_2 \qquad (1)$$

Nickel selenide nanoparticles have generated considerable interest among academics due to their outstanding electrocatalytic characteristics, inexpensive cost, and abundant nature. Different performance indicators such as the Tafel slope and overpotential are utilised to evaluate a catalyst's performance. The overpotential is the additional potential applied by the electrocatalytic cell to power the electrochemical process. Additionally, it is the voltage that is used to generate a certain current density [91]. The Tafel slope provides essential information regarding the electrochemical reactions' kinetics and reaction rate constants [41,76,92,93]. It also assists in finding the rate-determining step in a process involving several electron transfers [91,94]. The lower the value of the Tafel slope, the more facile the catalytic activity. The Tafel slope is determined using equation 2 [92].

$$T = \frac{2.3\ RT}{\alpha nF} \qquad (2)$$

where R = molar gas constant, T = Temperature, α = electron transfer coefficient, n = number of electrons transferred, and F = Faraday constant.

Table 2.3 shows a comparative study of a range of NiSe nanoparticles used in HER. When HER was performed in acidic media using NiSe [95] and $Ni_{0.85}Se$ [77], relatively high overpotentials of over 270 mV were achieved together with high Tafel slope values as shown in Table 3. The scientists ascribed the discrepancy in their findings to the aggregation and pilling of the nanoparticles, which reduced the number of active sites and resulted in a poor electrocatalytic response.

A different investigation found that differing morphologies of nickel selenide (nanosheets (NS) and nanoflakes) resulted in dissimilar overpotential values [48]. Wang et al. [44] synthesised selenium-enriched $NiSe_2$ nanosheets which exhibited reduced overpotential values due to the excess selenium on the catalyst's surface, which has a significantly lower hydrogen adsorption energy than the Ni atom. As a result of this, the catalytic reaction was enhanced [44,48,77,95]. The experimental conditions used to synthesise nickel selenide have been optimized to produce better application outcomes. Due to the comparatively low conductivity of nickel selenide, several compounds have been utilised to increase this property. For example, porous NF was incorporated into the matrix of NiSe which resulted in an increased surface area, conductivity, and electrical performance [76].

When cobalt and reduced graphene oxide were used to modify nickel selenide, Xu et al. [77] obtained similar results. Cobalt doping on NiSe supported on reduced graphene oxide (RGO) lowers particle aggregation. Cobalt contributes to the enhancement of the electronic structure of $Ni_{0.8}Se$, which leads to an increase in the conductivity. Alternatively, the RGO contributes to the uniform distribution of the nanoparticles, hence increasing the number of catalytic active sites. The electrolysis rate is greatly improved by the catalyst as a result of the system's reduced impedance to electron transfer. Wang et al. [47], on the other hand, obtained poor electrocatalytic results when they employed RGO-PI/CNT during modification. These results are comparable to those found using NiSe as a catalyst [95]. These findings could be explained by the fact that different synthesis methods were used, resulting in nanoparticles of varying sizes. The high HER results obtained by Wang et al. [47] after the incorporation of CNTs in the matrix of NiSe were due to the strong interaction between these two components. Du et al. [78] stated that one-dimensional materials such as CNTs have superior electrocatalytic characteristics, facilitating rapid axial charge transfer. The highly porous carbon nanotubes enhanced the electrocatalytic reaction's conductivity and surface area. According to Hussain et al. [41], the best results for HER occur in acidic media whereas Zhou et al. [76] assert that an alkali media is optimal because catalysts are corroded by acid. The majority of HER have been conducted in acidic environments, and only few in alkali conditions. Additional studies in alkali environments is necessary to determine which environment produces the most favourable outcomes [77].

Table 2. 3: Different NiSe electrocatalysts used in HER

Catalyst	**Overpotential (mV)**	**Tafel slope (mV dec^{-1})**	**Solution**	**Ref**
NiSe	272	64	0.5 M H_2SO_4	[95]
$Ni_{0.85}Se$	270	81	0.5 M H_2SO_4	[77]
$NiSe_2$-NS	117	32	Acidic water	[44]
$NiSe_2$-NS	198	72.1	0.5 M H_2SO_4	[48]
$NiSe_2$ nanoflakes	217	28.6	0.5 M H_2SO_4	[48]
$NiSe_2$/Ni	143	49	0.5 M H_2SO_4	[76]
$Ni_{0.8}Se$/RGO	182	62	0.5 M H_2SO_4	[77]
Co-$Ni_{0.8}Se$/RGO	148	49	0.5 M H_2SO_4	[77]
NiSe-RGO-PI/CNT	270	61	0.5 M H_2SO_4	[47]

2.4.2 In OER

Four electrons are transferred during the OER to form the oxygen-oxygen bond. The reaction is strongly pH-dependent and exhibits high overpotentials. Figure 2.4 illustrates the OER mechanism in acidic and basic media. Four hydroxide ions are converted to dioxygen and water in neutral and alkaline conditions, whereas two water molecules are converted to protons and oxygen molecules in acidic media [96].

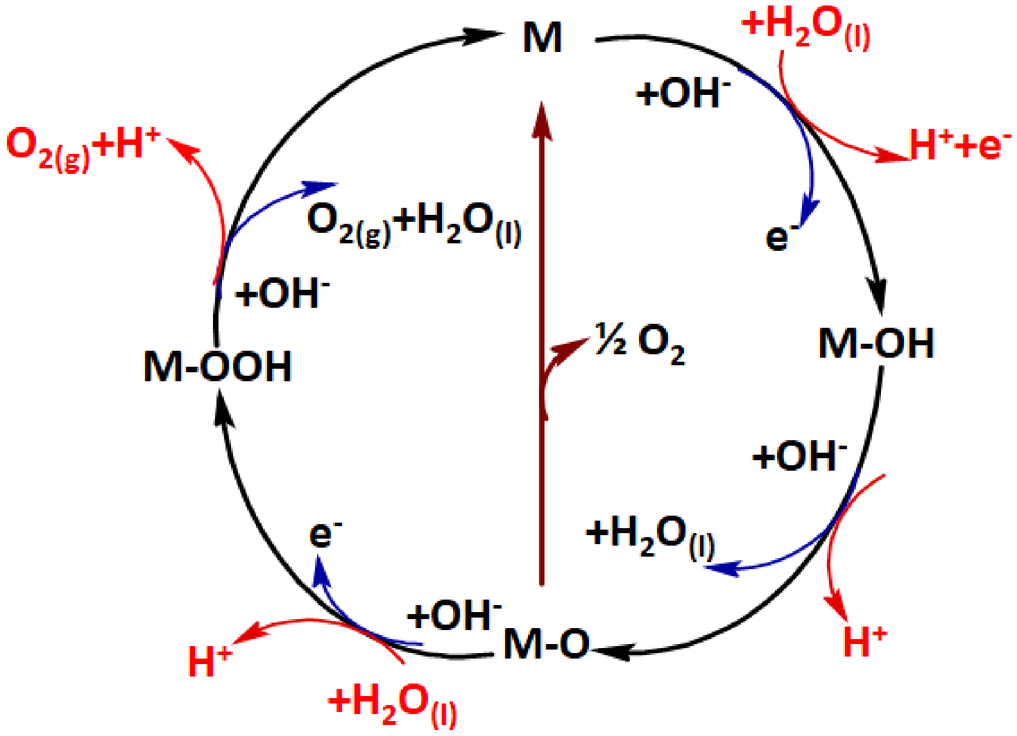

Figure 2. 4. OER mechanism in basic and acidic media [96].

There are only a few reports on the use of nickel selenide and related derivatives in OER as shown in Table 2.4. Zhang et al. [80] demonstrated the use of $NiSe_2$ nanoparticles with an octahedral shape and reported that a 375 mV overpotential was employed to produce a current density of 10 mA cm^{-2} and a Tafel slope of 89.36 mV dec^{-1}, in comparison to lower values achieved using $NiSe_2$ nanosheets having a porous structure [97].

To improve the electrochemical performance of the catalysts, they were modified with various nanomaterials. The use of heteroatoms to dope Ni selenides significantly improves the electrocatalytic performance of OER and total water splitting [79]. This is because the electric conductivity has been increased through intermediate bond modification and the presence of additional active sites [79,80,97]. The process's better performance can be attributed to charge delocalization between the metal cations [78]. Fe doping to generate iron-nickel-selenide/Ni foam (FeNiSe/NF) for use as an electrocatalyst for OER in alkaline media resulted in much higher overpotential, current density and Tafel slope values than $Fe_{7.4\ \%}$NiSe/NF, as shown in Table 4. The NF acted as a supporting structure [79]. Despite the fact that the synthesis was done using the same solvothermal process, the nanorods formed had varying diameters. Iron-nickel-selenide/Ni foam nanorods had much smaller diameters in comparison to those of $Fe_{7.4\ \%}$NiSe/NF which justifies the significant differences in the electrocatalysis results. outcomes.

The smaller the nanoparticles, the larger the surface area and the more exposed catalytic sites. Additionally, incorporating Fe into the catalyst's synthesis improved the catalyst's electrical conductivity, promoted electron mobility, and increased the catalyst's contact surface with the electrolyte.

The use of highly porous $Ni_{0.75}Fe_{0.25}Se_2$ with a large surface area resulted in satisfactory OER results as indicated in the table. A relatively low Tafel slope of 47.2 mV dec^{-1} [97] was achieved compared to 89.36 mV dec^{-1} [80] when unmodified nickel selenide was used. The formation of gas bubbles on the electrode which impedes the transfer of electrons was inhibited by the highly porous quality of the catalyst, resulting in improved electrocatalytic outcomes [78,79,97]. Cobalt modification to obtain $Fe_{0.08}Co_{0.09}Ni_{0.83}Se_2$ produced relatively poor electrocatalytic results. The unsatisfactory outcomes could be attributed to the reduced surface area and big particles around 500 nm. These results were comparable to those obtained using pure Ni_3Se_2, with nanoparticles sizes up to 2000 nm. When electrocatalysts are modified with iron or cobalt, electron transfer resistance must be lowered [80,92]. The analogues of various NiSe morphologies for OER applications are listed in Table 2.4.

Table 2. 4: Different nickel selenide electrocatalysts used in OER

Catalyst	**Overpotential (mV)**	**Current density ($mAcm^{-2}$)**	**Tafel slope (mV dec^{-1})**	**Solution**	**Ref**
$NiSe_2$	375	10	89.36	1 M KOH	[80]
$NiSe_2$-NS	323	10	83.6	1 M KOH	[97]
Ni_3Se_2	290	10	97	0.3 M KOH	[92]
FeNiSe/NF	290	60	61.0	1 M KOH	[78]
$Fe_{7.4\,\%}$NiSe/NF	231	50	43.0	1 M KOH	[79]
$Fe_{0.08}Co_{0.09}Ni_{0.83}Se_2$	268	10	57.53	1 M KOH	[80]
$Ni_{0.75}Fe_{0.25}Se_2$	255	35	47.2	1 M KOH	[97]

2.4.3 As counter electrode in solar cells

Solar power is a non-polluting and renewable energy source that has received a lot of attention in recent years. The sun's heat is turned directly into electricity. The downsides of typical silicon solar cells include the expensive module costs and the complexity of the manufacturing process. These drawbacks have limited their use in residential and industrial applications. Many scientists have been attracted to dye-sensitized solar cells (DSSCs) due to their efficient conversion of light to electricity, ease of fabrication, low manufacturing costs, and environmental friendliness [98–100].

The primary components of a DSSC device are a semiconductor, an electrolyte solution based on I_3^-/I^-, and a counter electrode (CE) that catalyses the reduction of triiodide ions to iodide ions. Various metal selenides, carbon nanomaterials [101], conductive polymers [102,103] carbides [104], and nitrides [105] are some of the famous materials that have been employed as CEs. The triiodide/iodide electrolyte contains two redox couples:

Left redox pair: $I_3^- + 2e^- \rightleftharpoons 3I^-$ (3)

Right redox pair: $3I^- + 2e^- \rightleftharpoons 2I_3^-$ (4)

The charge transfer resistance (R_{ct}) is proportional to the material's catalytic property where a low R_{ct} value enhances electron transport and minimises electron-hole pair recombination [106]. Power conversion efficiency (PCE) is another crucial component to consider. The PCE indicates a solar cell's overall performance whereas the short-circuit current density (Jsc) indicates the current that flows through the solar cell, and it is independent of the solar area when the voltage is zero. Numerous papers on the use of NiSe and its modifications for DSSCs have been published in the literature. For example, Wu et al. [63] employed NiSe-1 as the CE for the DSCC. The NiSe-1 had an average diameter, J_{sc}, R_{ct}, and PCE values of 70 nm, 14.86 mA cm^{-2}, 1.14 Ω and 7.82%, respectively. The poor electrocatalytic performance may be a result of the aggregation of NiSe nanoparticles, that in turn inhibited the reduction activity. As a result, NiSe must be modified to mitigate the agglomeration effects and it contributes significantly to the enhancement of the catalysts properties [107].

Wei et al. [106] synthesised $Ni_{0.5}Fe_{0.5}Se_2$ by doping NiSe with Fe which produced particles with sizes of 20 nm, J_{SC}, R_{ct}, and PCE values of 15.03 mA cm^{-2}, 0.68 Ω and 7.89 %, respectively. Also, Wei et al. [108] got a particle size of 20 nm for Fe-$Ni_{0.85}Se$ nanocomposite but obtained greater short-circuit current density and power conversion efficiency values, with a small decrease in charge transfer resistance by 0.01 Ω. Generally, the iron-modified catalyst outperformed the NiSe-1 catalyst in terms of electrochemical performance. This is because of the material's nanostructure, which enhances the catalyst's surface area. Additionally, metal insertion into the catalyst might result in homo or heterojunction, which aids in the modification of the electronic structure, improve the catalyst's conductivity, allow rapid transfer of charge, and enhance its performance. The lower charge transfer coefficients facilitate rapid electron transport from CE to electrolyte [63,106,108].

Another paper described the production of NiSe/$GN_{0.5}$ using graphene. The nanocomposite exhibited exceptional PCE and J_{SC} values [107]. This was due to the graphene being uniformly distributed on the surface of NiSe, preventing it from aggregating. Thus, good nanoparticle distribution is required for the reduction of triiodide to iodide. However, the use of high graphene content may lead to reduced electron transport and an increase in R_{ct}. Thus, it is necessary to optimise the amount of graphene loaded [107,109].

Co modification to form $Ni_{0.33}Co_{0.67}Se$ [110] produced remarkable results as shown in Table 2. 5. The nanocatalyst's superior performance is a result of the synergistic effects of Ni and Co ions. Furthermore, the porous character of cobalt/nickel-based selenides contributes to the electrocatalytic reduction of triiodide by offering alternate diffusion pathways for the redox reaction.

As Murugadoss et al. [109] showed, the addition of graphene to produce $Co_{0.5}Ni_{0.5}Se/GN_{0.5}$ significantly improves its electrocatalytic characteristics. In this case, the CE achieved a greater PCE of 9.42% [109–112]. Due to the exceptional features of quantum dots (QD), quantum dot sensitised solar cells (QDSSCs) have been discovered as prospective candidates for third-generation solar cells. Zinc selenide, cadmium selenide and cadmium telluride are examples of QD that have been used in solar cells. Despite their highly valued properties, QD have been shown to be less efficient in QDSSCs than DSSCs. To our knowledge, there are just a few studies in the literature describing the development or improvement of CEs [70,113–115]. Therefore, more research and development efforts should be made in this area. Table 2.5 summarises the use of NiSe and its composites as counter electrodes in solar cells.

Table 2. 5: Comparison of NiSe-based CEs in DSSCs.

CE	**Average size of nanomaterial (nm)**	**J_{SC} (mA cm^{-2})**	**R_{ct} (Ω)**	**PCE, CE (%)**	**REF**
NiSe-1	70	14.86	1.14	7.82	[63]
$Ni_{0.5}Fe_{0.5}Se_2$	20	15.03	0.68	7.89	[106]
10% Fe- $Ni_{0.85}Se$	20	16.56	0.67	8.57	[108]
NiSe/$GN_{0.5}$	16	16.73	1.92	8.62	[107]
$Co_{0.42}Ni_{0.58}Se$	200	14.29	2.95	6.15	[112]
$Ni_{0.33}Co_{0.67}Se$	100	17.29	1.11	9.01	[110]
$Co_{0.5}Ni_{0.5}Se/GN_{0.5}$	-	18.33	1.79	9.42	[109]

2.4.4 In urea conversion

Urea is considered a promising energy source due to its high stability, high energy density, vast reserves, high hydrogen content, and ease of storage and transportation [116,117]. Notably, urea is regarded as an advanced carrier of hydrogen due to its lower cell potential (0.37 V) compared to that of the water-splitting reaction (1.23 V) [116,118]. Equations 2.5 and 2.6 illustrate the electrooxidation of urea [119]:

Anodic reaction: $CO(NH_2)_2 + 6OH^- \rightarrow N_2 + CO_2 + 5H_2O + 6e^-$ $E^{\theta} = -0.746$ V (2.5)

Cathodic reaction: $6H_2O + 6e^- \rightarrow 3H_2 + 6OH^-$ $E^{\theta} = -0.83$ V (2.6)

The reaction that takes place at the anode results in the production of nitrogen and carbon dioxide. The cathodic process produces hydroxide ions and hydrogen gas, that can be utilised as energy.

Notably, this process can be used to generate energy while simultaneously resolving the contamination of water [83,119]. However, due to the intricate process of transferring multiple electrons, this oxidation reaction has sluggish kinetics and requires catalysts that are inexpensive, highly stable, and efficient. Latest investigations have demonstrated that Ni composites exhibit remarkable electrocatalytic capabilities for urea oxidation in basic environments, with the reaction taking place on NiOOH active sites. For instance, Xinrang et al. [119] discussed the use of several of these materials in urea electrolysis and fuel cells. Regrettably, there have been few reports on the application of nickel selenide in this field of study. The electrolysis of urea using $NiSe_2$/NF is shown in Figure 2.5.

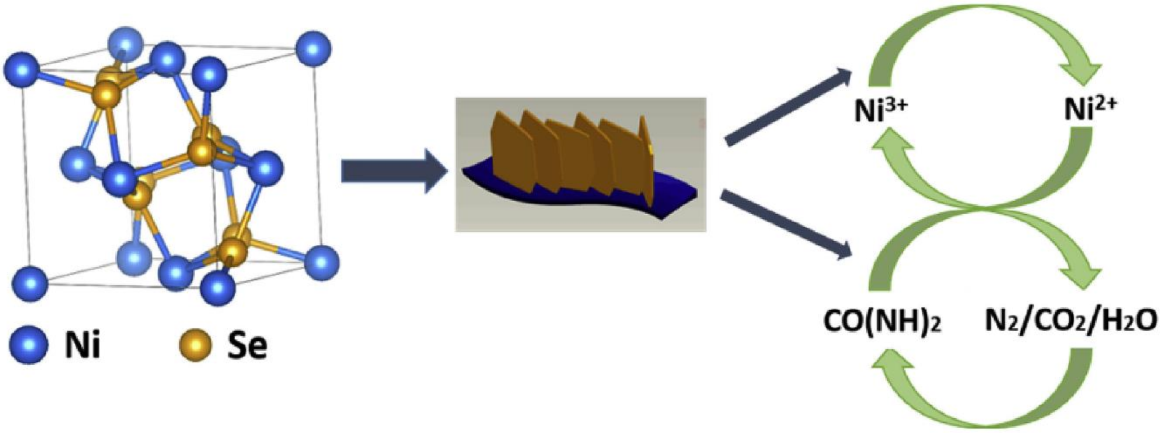

Figure 2. 5. Electrolysis of urea using $NiSe_2$/NF [83].

For the urea electrooxidation reaction (UOR), Xiong et al. [83] employed $NiSe_2$ nanoflakes and achieved remarkable electrocatalytic results. A 20 mV dec^{-1} Tafel slope, a potential of 324 mV to drive 10 mA cm^{-2}, and a charge transfer resistance of 4.5 Ω were obtained. The nanoflakes' extraordinary electrocatalytic effectiveness was attributed to their bumpy or uneven surface which results in an increase in the number of active sites. A different study discussed the application of NiSe nanoparticles/NF, NiSe nanowires/NF, and Se-$Ni(OH)_2$@NiSe/NF to generate a current density of 100 mA cm^{-2} [120], and potentials of 392 mV, 384 mV, and 366 mV were needed, correspondingly. Se-$Ni(OH)_2$@NiSe/NF demonstrated the smallest R_{ct} compared to the other compounds. The small R_{ct} obtained was attributed to the structure's unique core-shell configuration, in which the nickel selenide core's high conductivity enables fast electron transport while Se-$Ni(OH)_2$ shell exposes numerous active sites for the reaction. Furthermore, the use of Se-$Ni(OH)_2$ as an electrocatalyst resulted in the CO_2 adsorption and desorption barriers decreasing, thus enhancing the kinetics of electron transport.

2.4.5 In glucose sensing

While this chapter focused on the environmental uses of NiSe, a few articles have been published in which it has been used for glucose detection. Diabetes mellitus is a major cause of death and disability throughout the world [65]. It is a metabolic disorder in which the body is unable to control the level of glucose in the blood due to pancreatic dysfunction [65,121]. As a result, it is critical to develop very sensitive sensors, that allow for rapid electron movement, and low detection limits.

Sensors not based on enzymes are frequently used compared to enzymatic-based sensors due to their costly prices, the complexity of immobilising the biomolecule on the electrode, and the diminution of the enzyme's function [65,122,123]. Mani et al. [65] demonstrated the application of a nickel selenide nanosheets modified glassy carbon electrode for glucose detection and attained 1.57 µA μM^{-1} cm^{-2} sensitivity and a detection limit of 23 nM. Another study reported having achieved a detection limit of 40 nM and sensitivity of 5.962 µA µ M^{-1} cm^{-2} after using nickel selenide nanosheet arrays on nickel form [64]. The outstanding sensing properties may be attributed to the high surface area, catalytic activity and conductivity, which were achieved through synergistic interactions between nickel selenide and the nickel form [64]. Furthermore, using small amounts of polymer binders could result in negligible or no overpotentials.

2.5 Chromatographic methods for the detection of nevirapine

Nevirapine (NVP) is one of the most commonly prescribed antiretrovirals worldwide [124]. Nevirapine has been detected in the past using several chromatographic methods. The majority of reported methods used solid-phase extraction for isolation and a chromatographic technique for the determination of the analytes. Table 2.6 shows various chromatographic techniques previously used for NVP determination. Using liquid chromatography coupled to (tandem) mass spectrometry (LC-MS/MS), Rimayi et al. [125,126] detected NVP concentrations of 55 ng/L and 71 ng/L in dam water and river water in South Africa, respectively. The method had a 0.2 ng/L limit of detection (LOD). Wooding et al. [127] detected NVP concentrations greater than 148 ng/L and obtained a LOD of 44.4 ng/L using the same technique. In another study, Abafe et al. [128] detected 1900 ng/L NVP in wastewater treatment plant effluent using the same technique but obtained a LOD of 6 ng/L. When gas chromatography-time of flight mass spectrometry (GC-TOFMS) was used to determine NVP concentration in WWTP effluent, a concentration of 350 ng/L was obtained and the method LOD was found to be 1.8 ng/L. GC-TOFMS has been demonstrated to be a feasible alternative to LC-MS/MS in terms of reliability, robustness and sensitivity [129]. Yao et al. [130] detected very low concentrations of NVP, in the range of 0.32-1.86 ng/L in a WWTP in China using an Ultrahigh performance liquid chromatography system coupled to a triple quadrupole mass spectrometry, with electrospray ionization (ESI) (UPLC-ESI-MS/MS). A low LOD of 0.13 ng/L was obtained. Generally, higher concentrations of NVP have been detected in South African WWTPs compared to China and other countries such as Germany or Finland. According to the World Health Organisation (WHO) statistics for 2020, around 25.4 million people in Africa are anticipated to be living with HIV/AIDS, which may result in the large usage of ARVs and subsequent high detection levels in WWTPs [130]. These afore-mentioned analytical techniques offer high precision, sensitivity, accuracy and selectivity. They have been proven to be effective at detecting a broad spectrum of ARVs at low concentrations in a variety of environmental matrices [131–133]. However, these techniques are often overpriced, need sophisticated equipment, demand extensive sample preparation procedures, require trained personnel, and the lengthy analysis time limits the scope of their application. Electrochemical techniques are relatively cost-effective, simple, reliable, sensitive, and fast alternatives to other methods for determining a wide variety of electroactive compounds [11,134–137]. Additionally, electrochemical methods offer high precision, wide liner ranges, low detection limits, portability, and often require small sample volumes [138].

Table 2. 6: Chromatographic techniques used for NVP determination

Detection method	Matrix	LOD	Ref
LC-MS/MS	River water	0.2 ng/L	[125]
LC-MS/MS	Dam water	0.2 ng/L	[125]
LC-MS/MS	Dam water	44.4 ng/L	[127]
LC-MS/MS	WWTP effluent	6 ng/L	[128]
GC-TOFMS	WWTP effluent	1.8 ng/L	[129]
UHPLC-ESI-MS/MS	WWTP effluent	0.13 ng/L	[130]

2.6 Electrochemical techniques for the detection of nevirapine

Various electrochemical techniques have been applied in the detection of NVP in urine [139], human serum [134], pharmaceutical formulations [139], and various electrolyte solutions such as phosphate buffer solutions (PBS), sodium hydroxide (NaOH), and Britton Robinson buffer (BR) as seen in Table 2.7. NVP detection is mostly focused on differential pulse voltammetry (DPV), which is usually carried out in PBS or NaOH solutions of different pH values. Teradal et al. [140] determined NVP in PBS at pH 10 using a bare glassy carbon electrode (GCE), obtaining a limit of detection of 1.026 µM, compared to 0.003 µM when Castro et al. [141] utilised a thin film mercury-modified glassy carbon electrode (Hg/GCE) in a sodium hydroxide solution pH 11.3. The large difference in the LOD values may be attributed to the presence of a thin film of mercury on the surface of the electrode. Electrode modification has enabled the development of novel electrodes for electroanalytical applications. It results in increased selectivity, improved sensitivity, and stability of the electrode response that could not be achieved using bare electrodes [134]. Modified electrodes have several advantages over macro electrodes, including a larger electroactive surface area, improved electron transfer, and surface electrocatalysis [135,139,142]. Limits of detection of 0.066 µM and 0.050 µM were obtained when a copper oxide nanoparticles-carbon nanoparticles-modified glassy carbon electrode (CuO/CNPs/GCE) and palladium nanoparticles supported reduced graphene oxide decorated with molybdenum disulfide quantum dots-modified glassy carbon electrode (Pd@rGO/MoS$_2$QD/GCE) were used to determine NVP in 2 different buffers, LODs of respectively [134,143]. According to Shahrokhian et al. [134], the roughness of the CuO-CNP layer resulted in a significant increase in the electrode's active surface area, which influenced the sensitivity of the voltammetric measurements. On the other hand, Tiwari et al. [143] stated that there was a possibility of π-π conjugation and hydrophobic interaction between the rings of Pd@rGO and the aromatic rings of NVP, which may have resulted in rapid electron transfer processes. The MoS_2QD enhanced the surface area and catalytic activity of the sensor. The electrode modification using titanium oxide/graphene nanoribbons (TiO_2/GNR) resulted in a highly selective sensor with good reproducibility due to the synergic catalytic properties of TiO_2 and GNR [142]. In another study, a limit of detection of 0.0036 was achieved using three-dimensional cubic europium $(Eu)^{3+}$/cuprous oxide-modified glassy carbon electrode (Eu^{3+}/Cu_2O/GCE) [137]. For the determination of NVP in basic media, the modification of the carbon paste electrode with uracil (Ura), molecularly imprinted polymer (MIP) [138], and bismuth oxide (Bi_2O_3) [139] resulted in LODs of 0.05, 0.01, and 0.11 µM, respectively. The gold nanoparticles/poly(methylene-blue)/multi-walled carbon nanotubes/Graphite electrode (AuNPs/p((MB)/MWCNTs/GE) sensor had a LOD of 0.053 µM, which is comparable to the LODs of Pd@rGO/MoS_2QD/GCE and Ura/CPE. NVP has been successfully detected using various electrode materials, but as of current, not on a $NiSe_2$QD modified gold electrode. Additionally, there is a limited applicability for these sensors in real wastewater samples that has to be investigated. Therefore, this study aims to detect NVP directly in wastewater, an area that is still underexplored. The $NiSe_2$QD modified gold electrode for NVP detection could provide a highly sensitive platform with low detection limits.

Table 2. 7: Comparison of the analytical performances of different electrodes in NVP determination.

Working electrode	**Technique**	**Buffer, pH**	**LR (µM)**	**LOD (µM)**	**Matrix**	**Ref**
GCE	DPV	PBS, 10	5.0-350	1.026	NVP tablets, human urine and serum	[140]
Hg/GCE	ASV	NaOH, 11.3	0.04-0.5	0.003	NVP tablets	[141]
CuO/CNPs/GCE	CV, LSV	BR, 7	0.1-100	0.066	Human serum	[134]
Pd@rGO/MoS_2QD/GCE	DPV	PBS, 10	0.1-80	0.050	Human serum	[143]
TiO_2/GNR/GCE	DPV	PBS, 11	0.020-0.14	0.043	NVP formulation	[142]

Eu^{3+}/Cu_2O/GCE	CV, DPV	PBS, 11	0.01-750	0.0036	NVP tablets, human serum	[137]
Ura/CPE	DPV	NaOH, 13	0.1-70	0.050	Human serum	[144]
MIP/CPE	SWSV	PBS, 11	0.05-300	0.010	NVP tablets, human serum	[138]
CPE-Bi_2O_3	DPV	PBS, 8	0.05-50	0.110	NVP tablets, human urine and serum	[139]
AuNPs/p((MB)/ MWCNTs/GE	DPASV	PBS, 11	0.1-50	0.053	NVP tablets Human serum	[135]

ASV, Adsorptive stripping voltammetry; LSV, Linear sweep voltammetry; SWSV, square wave stripping voltammetry; DPASV, differential pulse anodic stripping voltammetry.

References

1. F. R. Simões and M. G. Xavier, in Nanosci. Its Appl. (Elsevier Inc., 2017), pp. 155–178.

2. G. W. Hunter, S. Akbar, S. Bhansali, M. Daniele, P. D. Erb, K. Johnson, C.-C. Liu, D. Miller, O. Oralkan, P. J. Hesketh, P. Manickam, and R. L. Vander Wal, J. Electrochem. Soc. **167**, 037570 (2020).

3. H. S. Hassan, M. F. Elkady, and N. M. Serour, in Handb. Nanomater. Sens. Appl. (Elsevier, 2021), pp. 321–344.

4. N. P. Shetti, D. S. Nayak, K. R. Reddy, and T. M. Aminabhvi, in Graphene-Based Electrochem. Sensors Biomol. (Elsevier Inc., 2019), pp. 235–274.

5. S. A. Balogun and O. E. Fayemi, Biosensors **11**, 172 (2021).

6. A. G. M. Ferrari, R. D. Crapnell, and C. E. Banks, Biosensors **11**, 291 (2021).

7. M. J. Hummel, Bio-Inspired Materials for Electrochemical Sensors, 2021.

8. A. Tricoli and R. Bo, in Front. Nanosci. (Elsevier, 2020), pp. 247–269.

9. K. Y. Goud, M. Satyanarayana, A. Hayat, K. V. Gobi, and J. L. Marty, in Nanoparticles Pharmacother. (Elsevier Inc., 2019), pp. 195–216.

10. K. Białas, D. Moschou, F. Marken, and P. Estrela, Microchim. Acta 2022 1894 **189**, 1 (2022).

11. L. Qian, S. Durairaj, S. Prins, and A. Chen, Biosens. Bioelectron. **175**, 112836 (2021).

12. L. Cui, C. C. Li, B. Tang, and C. Y. Zhang, Analyst **143**, 2469 (2018).

13. R. Dhar, Nanosci. Nanotechnol. An Int. J. **4**, 32 (2014).

14. D. Bera, L. Qian, T. K. Tseng, and P. H. Holloway, Materials (Basel). **3**, 2260 (2010).

15. C. Frigerio, D. S. M. Ribeiro, S. S. M. Rodrigues, V. L. R. G. Abreu, J. A. C. Barbosa, J. A. V Prior, K. L. Marques, and J. L. M. Santos, Anal. Chim. Acta **735**, 9 (2012).

16. Z. Yue, F. Lisdat, W. J. Parak, S. G. Hickey, L. Tu, N. Sabir, D. Dorfs, and N. C. Bigall, ACS Appl. Mater. Interfaces **5**, 2800 (2013).

17. R. Hardman, Environ. Health Perspect. **114**, 165 (2006).

18. A. Valizadeh, H. Mikaeili, M. Samiei, S. M. Farkhani, N. Zarghami, M. Kouhi, A. Akbarzadeh, and S. Davaran, Nanoscale Res. Lett. **7**, 1 (2012).

19. J. Mittal, A. Batra, A. Singh, and M. M. Sharma, Adv. Nat. Sci. Nanosci. Nanotechnol. **5**, 043002 (2014).

20. K. J. Alagarsamy Pandikumar, in Count. Electrode Dye. Sol. Cells (2021), pp. 1–278.

21. R. S. Rawat, J. Phys. Conf. Ser. **591**, (2015).

22. N. Masunga, O. K. Mmelesi, K. K. Kefeni, and B. B. Mamba, J. Environ. Chem. Eng. **7**, 103179 (2019).

23. A. F. E. Hezinger, J. Teßmar, and A. Göpferich, Eur. J. Pharm. Biopharm. **68**, 138 (2008).

24. C. A. R.-G. S. Correa-espinoza, J. F. H.-P. S. A. Martel-estrada, and I. Olivas-armendáriz, J. Non-Oxide Glas. **10**, 7 (2018).

25. Y. K. Gun and S. Byrne, in Quantum Dot Sensors (2013), pp. 1–42.

26. C. Wang, X. Gao, Q. Ma, and X. Su, J. Mater. Chem. **19**, 7016 (2009).

27. M. A. Abate, K. Dehvari, J. Y. Chang, and K. Waki, Dalt. Trans. **48**, 16115 (2019).

28. A. L. Rogach, T. Franzl, T. A. Klar, J. Feldmann, N. Gaponik, V. Lesnyak, A. Shavel, A. Eychmu, Y. P. Rakovich, and J. F. Donegan, J. Phys. Chem. C **111**, 14628 (2007).

29. E. M. Hashem, M. A. Ahmed, and M. F. Abdel Messih, CrystEngComm **22**, 4816 (2020).

30. H. Labiadh and S. Hidouri, J. King Saud Univ. - Sci. **29**, 444 (2017).

31. R. M. Hodlur and M. K. Rabinal, Chem. Eng. J. **244**, 82 (2014).

32. S. Jain, S. Bharti, G. K. Bhullar, and S. K. Tripathi, J. Lumin. **219**, 116912 (2020).

33. J. P. O. M. B. Lutfan Sinatra, Mater. Matters **12**, 3 (2017).

34. P. Palanisamy, M. Chavali, E. M. Kumar, and K. C. Etika, in Nanofabrication Smart Nanosensor Appl. (Elsevier, 2020), pp. 253–280.

35. P. N. Li, A. V. Ghule, and J. Y. Chang, J. Power Sources **354**, 100 (2017).

36. Z. Niu and Y. Li, Chem. Mater. **26**, 72 (2014).

37. C. C. V. Restrepo, Cindy Vanessa, Environ. Nanotechnology, Monit. Manag. **15**, 100428 (2021).

38. R. Javed, M. Zia, S. Naz, S. O. Aisida, N. ul Ain, and Q. Ao, J. Nanobiotechnology **18**, 1 (2020).

39. K. Wieszczycka, K. Staszak, M. J. Woźniak-Budych, J. Litowczenko, B. M. Maciejewska, and S. Jurga, Coord. Chem. Rev. **436**, 213846 (2021).

40. S. Shanmugaratnam and S. Rasalingam, in Nanocatalysts (IntechOpen, 2019).

41. R. A. Hussain and I. Hussain, J. Solid State Chem. **277**, 316 (2019).

42. A. Panneerselvam, M. A. Malik, M. Afzaal, P. O'brien, and M. Helliwell, J. AM. Chem. Soc **130**, 2420 (2008).

43. B. Yuan, W. Luan, and S. T. Tu, CrystEngComm **14**, 2145 (2012).

44. F. Wang, Y. Li, T. A. Shifa, K. Liu, F. Wang, Z. Wang, P. Xu, Q. Wang, and J. He, Angew. Chemie Int. Ed. **55**, 6919 (2016).

45. A. Sobhani, M. Salavati-Niasari, and F. Davar, Polyhedron **31**, 210 (2012).

46. Z. Zhuang, Q. Peng, J. Zhuang, X. Wang, and Y. Li, Chem. - A Eur. J. **12**, 211 (2005).

47. T. Wang, X. Li, Y. Jiang, Y. Zhou, L. Jia, and C. Wang, Electrochim. Acta **243**, 291 (2017).

48. K. S. Bhat and H. S. Nagaraja, Int. J. Hydrogen Energy **43**, 19851 (2018).

49. M. O'Brien, Stephen, J. Nanomater. **2014**, 1 (2014).

50. N. Moloto, M. J. Moloto, N. J. Coville, and S. Sinha Ray, J. Cryst. Growth **311**, 3924 (2009).

51. H. Li, S. Chen, H. Lin, X. Xu, H. Yang, L. Song, and X. Wang, Small **13**, 1701487 (2017).

52. S. Wu, Q. Hu, L. Wu, J. Li, H. Peng, and Q. Yang, J. Alloys Compd. **784**, 347 (2019).

53. C. Zhao, Y. Zhu, W. Liu, Z. Chen, Z. Wang, and P. Feng, J. Solid State Chem. **266**, 37 (2018).

54. A. Sobhani and M. Salavati-Niasari, Superlattices Microstruct. **65**, 79 (2014).

55. T. J. S. Anand, M. Zaidan, and S. Shariza, in Procedia Eng. (Elsevier Ltd, 2013), pp. 555–561.

56. H. Sun, Z. Liang, K. Shen, M. Luo, J. Hu, H. Huang, Z. Zhu, Z. Li, Z. Jiang, and F. Song, Appl. Surf. Sci. **428**, 623 (2018).

57. R. S. Mane and C. D. Lokhande, Mater. Chem. Phys. **65**, 1 (2000).

58. P. P. Hankare, B. V. Jadhav, K. M. Garadkar, P. A. Chate, I. S. Mulla, and S. D. Delekar, J. Alloys Compd. **490**, 228 (2010).

59. K. Xu, H. Ding, K. Jia, X. Lu, P. Chen, T. Zhou, H. Cheng, S. Liu, C. Wu, and Y. Xie, (2016).

60. A. Sivanantham and S. Shanmugam, Appl. Catal. B Environ. **203**, 485 (2017).

61. C. Tang, Z. Pu, Q. Liu, A. M. Asiri, X. Sun, Y. Luo, and Y. He, ChemElectroChem **2**, 1903 (2015).

62. Q. Yang, X. Chen, H. Zhan, S. Wu, Q. Hu, R. Zhou, and Y. Xue, Synth. Met. **257**, 116167 (2019).

63. H. Wu, Y. Wang, L. Zhang, Z. Chen, C. Wang, and S. Fan, J. Alloys Compd. **745**, 222 (2018).

64. M. Ma, W. Zhu, D. Zhao, Y. Ma, N. Hu, Y. Suo, and J. Wang, Sensors Actuators, B Chem. **278**, 110 (2019).

65. S. Mani, S. Ramaraj, S. M. Chen, B. Dinesh, and T. W. Chen, J. Colloid Interface Sci. **507**, 378 (2017).

66. S. Wang, P. He, L. Jia, M. He, T. Zhang, F. Dong, M. Liu, H. Liu, Y. Zhang, C. Li, J. Gao, and L. Bian, Appl. Catal. B Environ. **243**, 463 (2019).

67. X. Yang, J. Zhang, Z. Wang, H. Wang, C. Zhi, D. Y. W. Yu, and A. L. Rogach, Small **14**, 1702669 (2018).

68. N. Moloto, M. J. Moloto, N. J. Coville, and S. Sinha Ray, J. Cryst. Growth **324**, 41 (2011).

69. H. Ren, Z. H. Huang, Z. Yang, S. Tang, F. Kang, and R. Lv, J. Energy Chem. **26**, 1217 (2017).

70. Y. H. Lee, Y. H. Yun, V. Hong Vinh Quy, S. H. Kang, H. Kim, E. Vijayakumar, and K. S. Ahn, Electrochim. Acta **296**, 364 (2019).

71. X. Shang, J. Q. Chi, S. S. Lu, B. Dong, Z. Z. Liu, K. L. Yan, W. K. Gao, Y. M. Chai, and C. G. Liu, Electrochim. Acta **256**, 100 (2017).

72. B. Seo, D. S. Baek, Y. J. Sa, and S. H. Joo, CrystEngComm **18**, 6083 (2016).

73. Y. Lin, Y. Pan, and J. Zhang, Int. J. Hydrogen Energy **42**, 7951 (2017).

74. J. Bai, Q. Sun, Z. Wang, and C. Zhao, J. Electrochem. Soc. **164**, H587 (2017).

75. Y. Hou, M. Qiu, G. Nam, M. G. Kim, T. Zhang, K. Liu, X. Zhuang, J. Cho, C. Yuan, and X. Feng, Nano Lett. **17**, 4202 (2017).

76. H. Zhou, Y. Wang, R. He, F. Yu, J. Sun, F. Wang, Y. Lan, Z. Ren, and S. Chen, Nano Energy **20**, 29 (2016).

77. P. Xu, J. Zhang, Z. Ye, Y. Liu, T. Cen, and D. Yuan, Appl. Surf. Sci. **494**, 749 (2019).

78. J. Du, A. Yu, Z. Zou, and C. Xu, Inorg. Chem. Front. **5**, 814 (2018).

79. Z. Zou, X. Wang, J. Huang, Z. Wu, and F. Gao, J. Mater. Chem. A **7**, 2233 (2019).

80. J. Zhang, B. Jiang, J. Zhang, R. Li, N. Zhang, R. Liu, J. Li, D. Zhang, and R. Zhang, Mater. Lett. **235**, 53 (2019).

81. B. Wang, X. Wang, B. Zheng, B. Yu, F. Qi, W. Zhang, Y. Li, and Y. Chen, Electrochem. Commun. **83**, 51 (2017).

82. H. Xu, K. Ye, K. Zhu, J. Yin, J. Yan, G. Wang, and D. Cao, Inorg. Chem. Front. (2020).

83. P. Xiong, X. Ao, J. Chen, J. G. Li, L. Lv, Z. Li, M. Zondode, X. Xue, Y. Lan, and C. Wang,

Electrochim. Acta **297**, 833 (2019).

84. S. Li, W. Cai, X. Ma, J. Zhu, and Y. Wang, Int. J. Electrochem. Sci **15**, 2923 (2020).

85. L. Du, W. Du, Y. Zhao, N. Wang, Z. Yao, S. Wei, Y. Shi, and B. Zhang, J. Alloys Compd. **778**, 848 (2019).

86. L. Wu, L. Shen, T. Wang, X. Xu, Y. Sun, Y. Wang, Y. Zhao, Y. Du, and W. Zhong, J. Alloys Compd. **766**, 527 (2018).

87. Y. Cui, G. Zhang, Z. Lin, and X. Wang, Appl. Catal. B Environ. **181**, 413 (2016).

88. M. Höök and X. Tang, Energy Policy **52**, 797 (2013).

89. T. N. Vezirolu and F. Barbir, Int. J. Hydrogen Energy **17**, 391 (1992).

90. L. Chiari and A. Zecca, Energy Policy **39**, 5026 (2011).

91. N. T. Suen, S. F. Hung, Q. Quan, N. Zhang, Y. J. Xu, and H. M. Chen, Chem. Soc. Rev. **46**, 337 (2017).

92. A. T. Swesi, J. Masud, and M. Nath, Energy Environ. Sci. **9**, 1771 (2016).

93. V. Fourmond, P. A. Jacques, M. Fontecave, and V. Artero, Inorg. Chem. **49**, 10338 (2010).

94. T. Shinagawa, A. T. Garcia-Esparza, and K. Takanabe, Sci. Rep. **5**, (2015).

95. M. R. Gao, Z. Y. Lin, T. T. Zhuang, J. Jiang, Y. F. Xu, Y. R. Zheng, and S. H. Yu, J. Mater. Chem. **22**, 13662 (2012).

96. N. Yuan, Q. Jiang, J. Li, and J. Tang, Arab. J. Chem. **13**, 4294 (2020).

97. Z. Wang, J. Li, X. Tian, X. Wang, Y. Yu, K. A. Owusu, L. He, and L. Mai, ACS Appl. Mater. Interfaces **8**, 19386 (2016).

98. J. Gong, J. Liang, and K. Sumathy, Renew. Sustain. Energy Rev. **16**, 5848 (2012).

99. J. Gong, K. Sumathy, Q. Qiao, and Z. Zhou, Renew. Sustain. Energy Rev. **68**, 234 (2017).

100. M. Grätzel, J. Photochem. Photobiol. C Photochem. Rev. **4**, 145 (2003).

101. A. Aboagye, H. Elbohy, A. D. Kelkar, Q. Qiao, J. Zai, X. Qian, and L. Zhang, Nano Energy **11**, 550 (2015).

102. J. Kwon, V. Ganapathy, Y. H. Kim, K. D. Song, H. G. Park, Y. Jun, P. J. Yoo, and J. H.

Park, Nanoscale **5**, 7838 (2013).

103. H. Wang, Q. Feng, F. Gong, Y. Li, G. Zhou, and Z. S. Wang, J. Mater. Chem. A **1**, 97 (2013).

104. M. Wu, X. Lin, A. Hagfeldt, and T. Ma, Angew. Chemie Int. Ed. **50**, 3520 (2011).

105. X. Zhang, T. Peng, L. Yu, R. Li, Q. Li, and Z. Li, ACS Catal. **5**, 504 (2015).

106. P. Wei, J. Li, Z. Hao, Y. Yang, X. Li, C. Jiang, and L. Liu, Appl. Surf. Sci. **492**, 520 (2019).

107. V. Murugadoss, J. Lin, H. Liu, X. Mai, T. Ding, Z. Guo, and S. Angaiah, Nanoscale **11**, 17579 (2019).

108. P. Wei, J. Li, H. Kang, Y. Yang, Z. Hao, X. Chen, D. Guo, and L. Liu, Int. J. Energy Res. **44**, 845 (2020).

109. V. Murugadoss, P. Panneerselvam, C. Yan, Z. Guo, and S. Angaiah, Electrochim. Acta **312**, 157 (2019).

110. X. Qian, H. Li, L. Shao, X. Jiang, and L. Hou, ACS Appl. Mater. Interfaces **8**, 29486 (2016).

111. J. Jia, J. Wu, Y. Tu, J. Huo, M. Zheng, and J. Lin, J. Alloys Compd. **640**, 29 (2015).

112. Q. Jiang, K. Pan, C. S. Lee, G. Hu, and Y. Zhou, Electrochim. Acta **235**, 672 (2017).

113. C. V. V. M. Gopi, S. Sambasivam, R. Vinodh, H. J. Kim, and I. M. Obaidat, J. Mater. Sci. Mater. Electron. **31**, 975 (2020).

114. C. H. Chang and Y. L. Lee, Appl. Phys. Lett. **91**, (2007).

115. J. Kusuma, S. Akash, and R. Geetha Balakrishna, Sol. Energy **201**, 674 (2020).

116. H. Yang, M. Yuan, Z. Sun, D. Wang, L. Lin, H. Li, and G. Sun, ACS Sustain. Chem. Eng. **8**, 8348 (2020).

117. A. N. Rollinson, J. Jones, V. Dupont, and M. V. Twigg, Energy Environ. Sci. **4**, 1216 (2011).

118. Z. Wang, P. Guo, M. Liu, C. Guo, H. Liu, S. Wei, J. Zhang, and X. Lu, ACS Appl. Energy Mater. **2**, 3363 (2019).

119. X. Hu, J. Zhu, J. Li, and Q. Wu, ChemElectroChem (2020).

120. C. Tang, Z. L. Zhao, J. Chen, B. Li, L. Chen, and C. M. Li, Electrochim. Acta **248**, 243 (2017).

121. P. K. Kannan and C. S. Rout, Chem. - A Eur. J. **21**, 9355 (2015).

122. K. O. Iwu, A. Lombardo, R. Sanz, S. Scirè, and S. Mirabella, Sensors Actuators, B Chem. **224**, 764 (2016).

123. T. Chen, D. Liu, W. Lu, K. Wang, G. Du, A. M. Asiri, and X. Sun, Anal. Chem. **88**, 7885 (2016).

124. P. Fan-Havard, Z. Liu, M. Chou, Y. Ling, A. Barrail-Tran, D. W. Haas, and A. M. Taburet, Antimicrob. Agents Chemother. **57**, 2154 (2013).

125. C. Rimayi, D. Odusanya, J. M. Weiss, J. de Boer, and L. Chimuka, Sci. Total Environ. **627**, 1008 (2018).

126. S. Ncube, L. M. Madikizela, L. Chimuka, and M. M. Nindi, Water Res. **145**, 231 (2018).

127. M. Wooding, E. R. Rohwer, and Y. Naudé, J. Chromatogr. A **1496**, 122 (2017).

128. O. A. Abafe, J. Späth, J. Fick, S. Jansson, C. Buckley, A. Stark, B. Pietruschka, and B. S. Martincigh, Chemosphere **200**, 660 (2018).

129. O. J. Schoeman, C., Mashiane, M., Dlamini, M. and Okonkwo, Chromatogr. Sep. Tech. **6**, 272 (2015).

130. L. Yao, Z. Y. Chen, W. Y. Dou, Z. K. Yao, X. C. Duan, Z. F. Chen, L. J. Zhang, Y. J. Nong, J. L. Zhao, and G. G. Ying, Water Res. **207**, 117803 (2021).

131. K. Reddy, N. Renuka, S. Kumari, and F. Bux, Chemosphere **280**, 130674 (2021).

132. Y. Zhang, L. Liu, and L. Ren, Sci. Rep. **10**, 1 (2020).

133. C. Ren, P. Fan-Havard, N. Schlabritz-Loutsevitch, Y. Ling, K. K. Chan, and Z. Liu, Biomed. Chromatogr. **24**, 717 (2010).

134. S. Shahrokhian, R. Kohansal, M. Ghalkhani, and M. K. Amini, Electroanalysis **27**, 1989 (2015).

135. M. Bagher, E. Ahmadi, and M. Haseli, Anal. Biochem. **527**, 4 (2017).

136. E. Ahmadi, M. Reza, V. Riahifar, and H. Momeneh, Microchem. J. **146**, 1218 (2019).

137. M. M. Foroughi, S. Jahani, Z. Aramesh-Boroujeni, M. Rostaminasab Dolatabad, and K. Shahbazkhani, Ceram. Int. **47**, 19727 (2021).

138. S. Massumi, E. Ahmadi, A. Akbari, and M. B. Gholivand, J. Electroanal. Chem. **876**, 114508 (2020).

139. N. L. Teradal and J. Seetharamappa, Electroanalysis **27**, 2007 (2016).

140. N. L. Teradal, S. N. Prashanth, and J. Seetharamappa, J. Electrochem. Sci. Eng. **2**, 67 (2012).

141. A. Aguiar Castro, R. Queiroz Aucelio, N. Adrian Rey, E. Monsores Miguel, and P. Augusto Mardini Farias, Comb. Chem. High Throughput Screen. **14**, 22 (2011).

142. D. Apath, M. Moyo, and M. Shumba, J. Chem. **2020**, 1 (2020).

143. P. Tiwari, N. R. Nirala, and R. Prakash, ChemistrySelect **3**, 5341 (2018).

144. F. Zhang, L. Li, L. Luo, Y. Ding, and X. Liu, J. Appl. Electrochem. **43**, 263 (2013).

CHAPTER THREE

EXPERIMENTAL METHODOLOGY

Summary

This chapter gives details of all the chemical reagents used in the preparation of the $NiSe_2$*QD materials and the characterisation techniques employed to study the properties of the QD materials. Herein, various capping agents including 3- mercaptopropionic acid (3-MPA) and banana peel extract (BPE), were utilised for this study. Surface functionalisation of the QD materials is very important as it aids in the stability of the nanomaterials, prevents agglomeration and enhances the optoelectronic properties of the QD [1,2]. The 3-MPA contains the thiol and carboxylic acid groups [3], whereas the BPE has been reported to contain several functional groups, including hydroxyls, amines, and carboxylic acids [4]. These functional groups are suitable for binding onto the surface of the QD. The aqueous colloidal synthesis approach was chosen for this research because of its unique qualities, which include monodispersity, high crystallinity, chemical integrity, and specificity, as well as the ability to further functionalize QD materials [5]. The synthesised QD materials were used for the electro-oxidation of the analyte (nevirapine). Characterisation techniques employed to study the properties of the as-synthesised of 3-MPA-*$NiSe_2$*QD or BPE-*$NiSe_2$*QD include High-resolution transmission microscopy and Small-angle X-ray scattering for particle size and internal structure analysis, X-ray diffraction for crystallinity studies, High-resolution scanning electron microscopy for studying the surface morphology, Energy-dispersive X-ray spectroscopy for elemental analysis, Fourier transform infrared spectroscopy and Raman spectroscopy for functional group analysis and vibrational studies. Ultraviolet-visible spectroscopy and Photoluminescence were utilised for optical studies. Differential pulse voltammetry was used for electrochemistry studies. The modified electrodes, 3-MPA-*$NiSe_2$*QD/L-Cyst/Au and Au/BPE-*$NiSe_2$*QD/Nafion were used in the determination of NVP in 0.1 M PBS pH 7.4. The selectivity of the electrochemical sensors was investigated in the presence of interfering species such as tenofovir, diclofenac and 1-ethyl-3-(3-dimethyl aminopropyl) carbodiimide hydrochloride (EDC). The proposed sensors were also used to determine NVP concentration in real wastewater samples.*

3. Characterisation Techniques

3.1 Spectroscopic techniques

Spectroscopic techniques are highly sensitive and non-destructive techniques used to study the properties of various samples using radiated energy. These techniques are based on the interaction between light and matter [6]. Very small sample volumes are required when using these techniques, and no complex sample preparation is involved.

3.1.1 Ultraviolet-visible spectroscopy (UV-Vis)

UV-Vis is an analytical technique used to obtain the absorbance spectra of a compound in an aqueous solution or a solid. It measures the absorbance or transmittance of light [7]. The amount of light absorbed by the sample at a given wavelength can be calculated by comparing the electromagnetic radiation entering the sample, also known as incident radiation (I_0) and the transmitted radiation (I). The concentration of known solutes can then be calculated using Beer-Lambert's law, which states that the absorbance is directly proportional to the concentration of the absorbing species and the path length of the absorbing medium given by equation 3.1 [7–9].

$$A = \log_{10}\left(\frac{I_0}{I}\right) = \varepsilon \times c \times l \qquad (3.1)$$

Where A is the measured absorbance, I_0 is the incident radiation, I is transmitted radiation, ε is the molar absorbtivity (L $mol^{-1}cm^{-1}$), c is the concentration of the absorbing species in (mol /L) and l is the path length (cm).

When light passes through a sample, the energy from the light excites an electron from a lower energy state to a higher energy orbital. The energy that is required to move from a lower energy state (E_1) to a higher energy state (E_2) must be equal to the energy of the electromagnetic radiation that causes this transition (electronic bandgap). Therefore, the electronic bandgap can be calculated using equation (3.2) [7]. In the present study, UV-vis spectroscopy was used to study the optical properties of the capping agents, metal precursors, and the synthesised 3-MPA and BPE-capped $NiSe_2$QD. UV-vis experiments were conducted on PerkinElmer UV–Vis spectrometer Lambda 6505 (South Africa) in the range of 250 to 800 nm. About 100 µL of the sample was diluted with 2 400 µL of distilled water in a quartz cuvette.

$$E_2 - E_1 = E = \frac{hc}{\lambda} \qquad (3.2)$$

Where E is the energy absorbed, h is the universal Planck's constant, ν is the frequency of incident light, c is the speed of light and λ is the wavelength.

3.1.2 Fourier transform infrared spectroscopy (FTIR)

FTIR is an effective and very powerful tool used to study the interaction between molecules and provides information on the presence of specific functional groups in a compound. This technique can be used to analyse both organic and inorganic substances quantitatively and qualitatively. The FTIR spectrum is recorded between 400 cm^{-1} and 4000 cm^{-1}. In this study, the FTIR instrument was used for the characterisation of the different capping agents and the prepared QD. The FTIR studies were performed on the PerkinElmer FTIR spectrometer Frontier using the KBr pellet method in the range of 400 cm^{-1} to 4000 cm^{-1}. The samples were mixed with KBR and dried in a vacuum oven at 60 °C overnight. The dried powder was then ground and pressed to a thin pellet before analysis.

3.1.3 Raman spectroscopy

Raman spectroscopy is a powerful spectroscopic technique used to investigate the vibrational, rotational and other resonant modes in samples. Raman spectroscopic studies of the synthesised QD were performed at an excitation wavelength of 532 nm on a WiTec Raman spectrometer (Alpha 300, TS 150) at 100× magnification. Samples were analysed on a glass slide.

3.1.4 Photoluminescence spectroscopy (PL)

Photoluminescence is the emission of light by any matter following photon absorption. In simpler terms, it is a process of excitation and emission. This technique is used to study the optoelectronic properties of materials. The Photoluminescence (PL) studies were performed using a Horiba NanoLog™ 3-22- TRIAX (Horiba Instrument Incorporated, Piscataway, NJ, USA), with double grating excitation and emission monochromators. The excitation wavelength used was obtained from UV-Vis.

3.2 Microscopic techniques

Microscopic techniques were used to determine the size and shape of the synthesised QD.

3.2.1 High-resolution scanning electron microscopy (HR-SEM) and Energy-dispersive X-ray spectroscopy (EDX)

HR-SEM is a microscopic technique that uses an accelerated beam of electrons to generate diverse signals at the surface of the specimen. EDX was used for elemental analysis [10]. HR-SEM and EDX were used to determine the surface morphology and elemental characterisation of the as-synthesised 3-MPA-$NiSe_2$QD. The samples for HR-SEM were prepared on clean glass slides. Known volumes of the sample (10 µL) were dropped onto the slide and allowed to dry at room temperature before coating them using an Agar Turbo gold coater. A JEOL JSM-IT300 series SEM was used to capture images. A JEOL JSM-7800FLV field emission scanning electron microscope was used for the characterisation of BPE-$NiSe_2$QD. An energy dispersive X-ray spectrometry (EDX) (Oxford X-MAXN) coupled to SEM was used for chemical composition analysis.

3.2.2 High-resolution Transmission electron microscopy (HR-TEM)

HR-TEM is a highly sophisticated instrument that offers crystallographic information about the specimen at the atomic level. HR-TEM manipulates an electron beam generated at a high potential in an electrically heated filament using a series of electromagnetic lenses [11]. This beam of electrons is transferred through an ultra-thin sample, resulting in an image being formed due to the interaction between the sample and the electrons. In this study, the HR-TEM was used to determine the size and shape of the prepared QD. HR-TEM images were recorded using a Tecnai G2 F20X-Twin MAT operated at an accelerating voltage of 200 kV from FEI (Eindhoven, Netherlands). Before analysis, the liquid samples of the quantum dots were preconcentrated at 14 000 rpm for 30 min. Thereafter, the resulting solution was dispersed in ethanol and sonicated for 10 min. A small drop of the dilute solution of the quantum dots was placed on a copper-coated grid for HRTEM and was allowed to air dry.

3.3 X-Ray Diffraction (XRD)

XRD is a versatile, non-destructive technique that is based on the diffraction of X-rays by matter. It is used for phase identification and the determination of the crystalline structure, crystal size, and chemical composition of materials [12]. A diffraction pattern is generated when a material is irradiated with X-rays. Bragg's Law equation (3.3) establishes a simple requirement under which a diffracted beam can be observed. It explains why cleavage faces of crystals reflect X-ray beams at certain incident angles (θ). The variable d denotes spacing between atomic layers, λ is the wavelength of the X-ray and n is an integer. Figure 3.4 is a schematic representation of XRD. Only diffracted waves that satisfy Bragg's Law form a diffraction pattern [13].

$$n\lambda = 2d \sin\theta \qquad (3.3)$$

The Debye-Scherrer equation (3.4) can be used to calculate the crystallite size [14].

$$d = \frac{K\lambda}{\beta \cos\theta} \qquad (3.4)$$

Where d is the crystallite size, K is a constant crystalline shape factor, λ is the X-ray wavelength, β is the full-width half-maximum (FWHM), and θ is the angle of reflection.

In this study, p-XRD was used to investigate the crystallinity of 3-MPA-$NiSe_2$QD and BPE-$NiSe_2$QD using a PANanalytical XRD machine. The MATCH and Diamond softwares were used for analysis.

3.4 Small-angle X-ray scattering (SAXS)

SAXS has been extensively used to obtain valuable information about the size, shape, and structure of colloidal particles [15]. SAXSdrive software is used to collect the scattering curve. The scattering pattern of the reference (blank) is also captured and then subtracted from the scattering pattern of the sample solution, leaving only the signal from the target particles. The resulting scattering curve is then used for data analysis to obtain valuable information about the size or shape of the particles [16]. SAXStreat and SAXSquant are two programs that are used for data processing and evaluation. SAXStreat software is used for data reduction and to calibrate the position of the primary beam. Further processing of the date including solvent subtraction and de-smearing is performed in SAXSquant. The GIFT (Generalized Indirect Fourier Transformation) software is used to Fourier transform the scattering data to obtain the pair distance distribution function (PDDF) and size distribution curves [3,17]. The structure and sizes of the prepared 3-MPA capped $NiSe_2$QD and BPE capped $NiSe_2$QD were determined using the SAXSpace instrument (Anton Paar, GmbH, North Ryde, Australia) using 35 µL liquid sample in a 1mm diameter quartz capillary. The temperature was controlled at 20 ℃ and five frames were acquired for each measurement at 60 s exposure time and averaged. The measurements for deionised water which was used as the reference material were obtained under the same conditions as the QD.

3.5 Electrochemical techniques

Electrochemical sensors have attracted a great deal of interest in many fields such as analytical chemistry, clinical diagnosis, environmental monitoring, and industrial processes due to their quick response, ease of operation, high selectivity, portability, energy efficiency, and cost-effectiveness [18,19]. The redox properties of the electrochemical sensor and their prospective platform components at the electrode surface, which occur when a potential is applied were investigated using electrochemical techniques. Differential pulse voltammetry (DPV) was employed to measure the electrochemical properties of 3-MPA capped $NiSe_2$QD, BPE capped $NiSe_2$QD, and some precursors using a Palmsens 3 Compact Electrochemical Interfaces

Potentiostat. DPV is a voltammetric technique that monitors current changes against applied voltages. It is similar to square wave voltammetry but more sensitive than cyclic voltammetry. It has been identified as a useful tool in the rapid and sensitive detection of analytes in electroanalytical chemistry. The basic components of a modern electrochemical system are a potentiostat, a computer and an electrochemical cell, as shown in Figure 3.1. Electrochemical measurements are carried out in an electrochemical cell that consists of an ionic electrolyte, a dissolved sample in a solvent, and a three-electrode system. The three-electrode system constitutes a counter electrode (CE), a reference electrode (RE) and a working electrode (WE) [20]. The working electrode is the main component of the electrochemical system where the reaction of interest takes place [20]. It is where the redox properties of the analyte under investigation occurs.

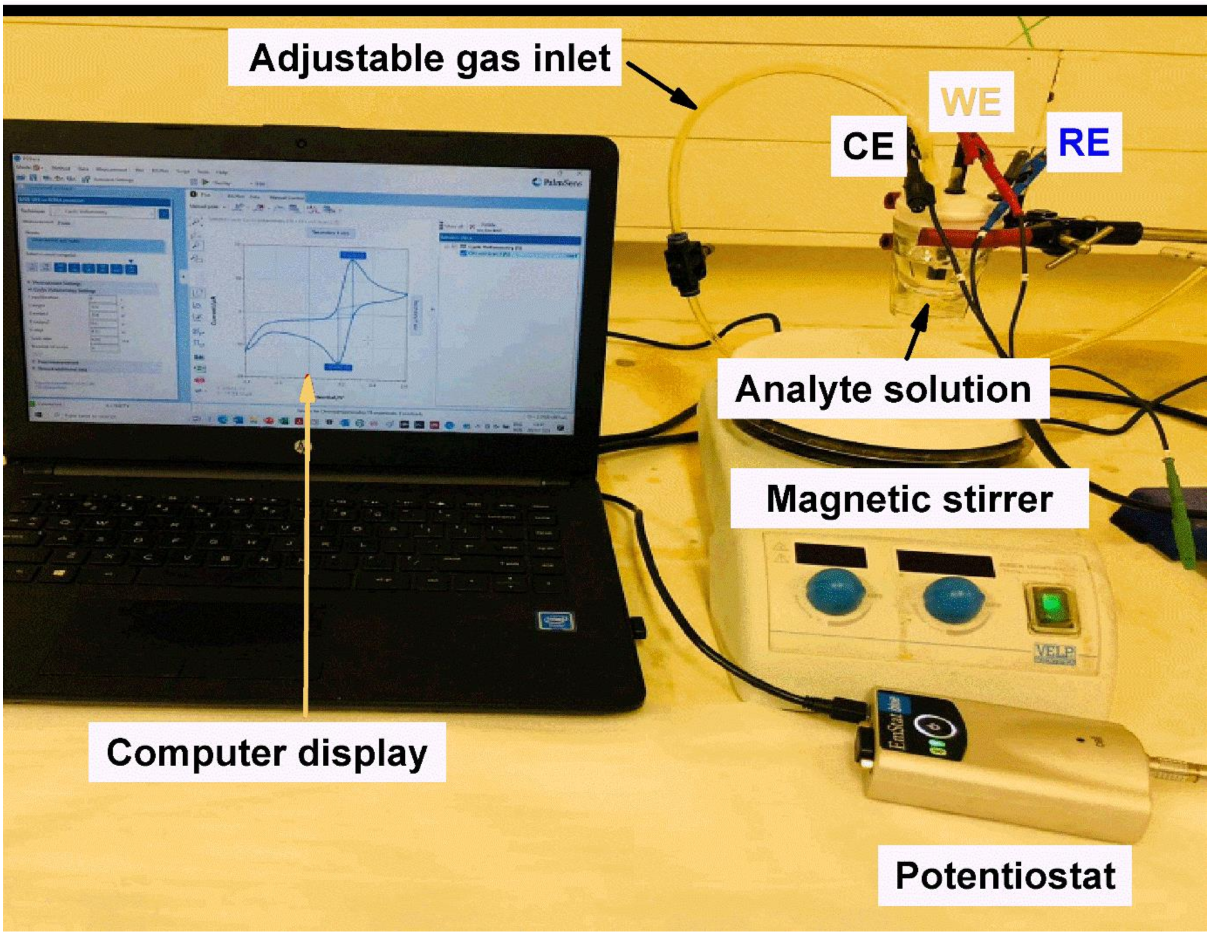

Figure 3. 1 A typical representation of the three-electrode system set-up.

3.6 Materials and methods

3.6.1 Chemical reagents

Nickel chloride hexahydrate ($NiCl_2.6H_2O$, 98%), Selenium powder (Se, ≥ 99.5 %), N-hydroxysuccinimide (NHS, 98 %), 1-ethyl-3-(3-dimethyl aminopropyl) carbodiimide hydrochloride (EDC, ≥98 %), L-cysteine (≥ 98.5 %), Sodium borohydride ($NaBH_4$, ≥ 96 %), 3- Mercaptopropionic acid (3-MPA, ≥ 99%), sodium chloride (NaCl, ≥ 99.5 %), disodium hydrogen phosphate dibasic ($Na_2HPO_4.2H_2O$, ≥ 99.5 %), Sodium phosphate monobasic dihydrate ($H_2NaPO_4.2H_2O$, ≥ 99 %) and Nevirapine 50 mg (NVP, ≥ 98%) were purchased from Sigma-Aldrich, South Africa. Sodium hydroxide (NaOH, 99.95 %) was purchased from Promark Chemicals, South Africa. All the chemicals used in the experiments were of analytical grade and were used as purchased without further purification. Banana peels were sourced locally at a supermarket (Shoprite, South Africa). The drugs used for interference studies, Diclofenac sodium salt ($C_{14}H_{10}Cl_2$ $NNaO_2$), and Tenofovir ($C_9H_{14}N_5O_4P$, ≥ 98 %) were purchased from Sigma Aldrich, South Africa. A phosphate buffer solution (PBS, 0.1 M, pH 7.4) was chosen as the supporting electrolyte. NVP stock solution was prepared by dissolving 2mg of NVP in ethanol. The solution was ultrasonicated at room temperature and kept in a clean polytope as the NVP stock solution. The working solutions were prepared by appropriate dilutions of the stock solution with 0.1 M PBS at pH 7.4. Both the stock and working solutions were kept at room temperature when not in use. However, the buffer solution was kept in the refrigerator at 4 °C.

3.6.2 Preparation of BPE

The BPE was prepared according to a previously reported method [4,21]. The banana peels were washed thoroughly with deionised water and then dried with a paper towel. About 10 g of the peels were weighed and then boiled in deionised water at 80 °C for 10 min. The resulting solution was filtered twice to remove any solid particles, and the extract was stored at 4 °C.

3.6.3 Synthesis of 3-MPA-$NiSe_2$QD and BPE-$NiSe_2$QD

$NiSe_2$QD were prepared using the colloidal synthesis method following the methods established in previous studies with some modifications [3,22]. $NiCl_2.6H_2O$ (2,59g, 0.02M) and 3-MPA (5 mL, 0.06M) were dissolved in 100 mL deionised water. The resulting solution was adjusted to pH 12 using 5 M NaOH. The solution was bubbled with N_2 for at least 30 min. This was kept as flask **A** (Figure 3.2). In a separate flask **B** (Figure 3.3), Se powder (1,58g, 0.02M) and $NaBH_4$ (1,51g, 0.04M) were mixed in 100 mL of deionised water under inert conditions. The solution was stirred until a colourless solution of NaHSe was formed, after which 50 mL of this solution was quickly transferred to flask **A**. The contents were stirred vigorously and refluxed at 100 °C for 60 min. At 60 min, the reaction was quenched by washing the QD solution with very cold water. The resulting quantum dot solution was washed three times for 10 min using propan-2-ol and deionised water to remove any excess precursor. The rotational speed of the centrifuge was set at 4500 rpm. The precipitate obtained was re-dispersed in water and kept as solution **C** as illustrated in Figure 3.4. This solution was kept in the refrigerator for further use. The same procedure was followed in the preparation of BPE-capped $NiSe_2$QD. The chemical reaction for the formation of 3-MPA-$NiSe_2$QD is shown in equations (3.5–3.7) below:

Flask A

$$NiCl_2.6H_2O + H_2O + HSCH_2CH_2CO_2H \rightarrow HCO_2CH_2CH_2S - Ni + 2HCl + 6H_2O \quad (3.5)$$

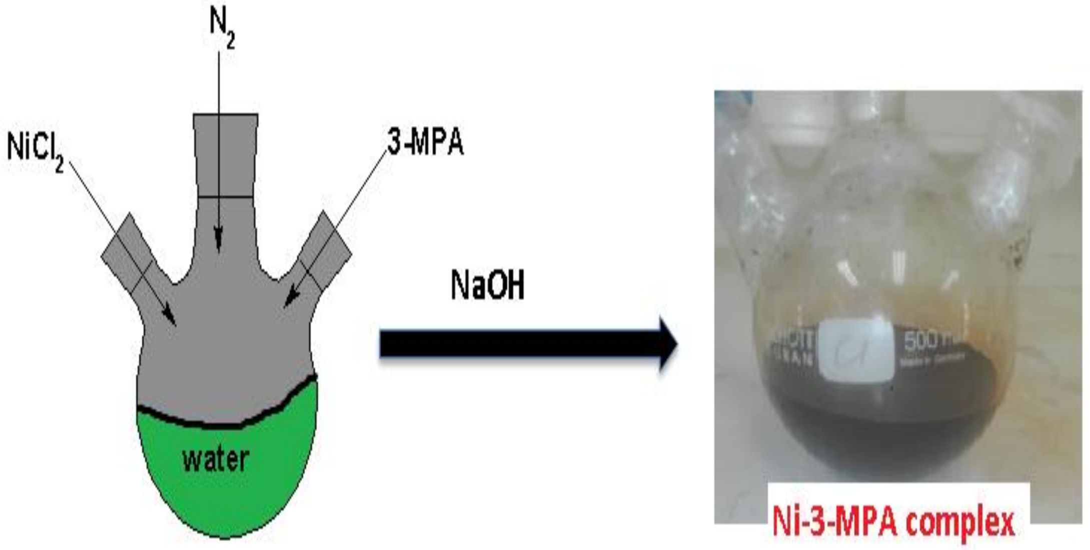

Figure 3. 2 Schematic diagram for the reaction between $NiCl_2$ and the capping agent 3-MPA.

Flask B

$$2Se + 4NaBH_4 + 7H_2O \rightarrow 2NaHSe + Na_2B_4O_7 + 14H_2 \quad (3.6)$$

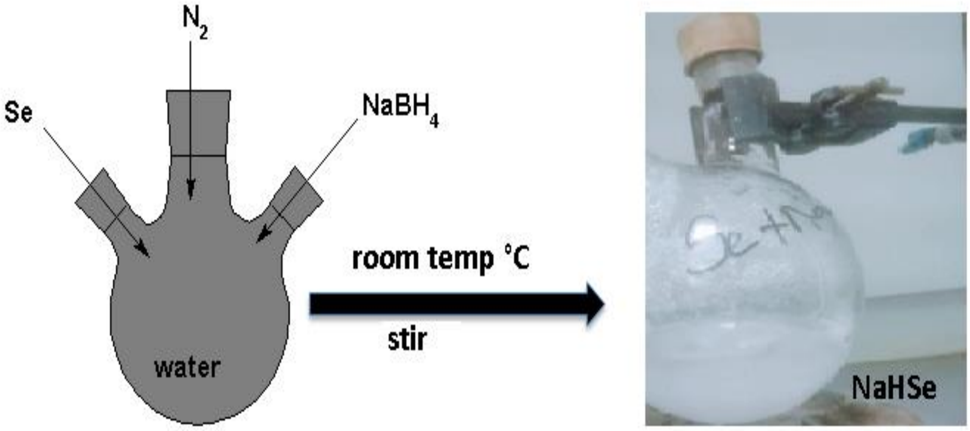

Figure 3. 3. Illustration of the reduction of selenium using sodium borohydride under an inert atmosphere.

Flask A + Flask B

$$2NaHSe \ + HCO_2CH_2CH_2S - Ni \ \rightarrow \tag{3.7}$$

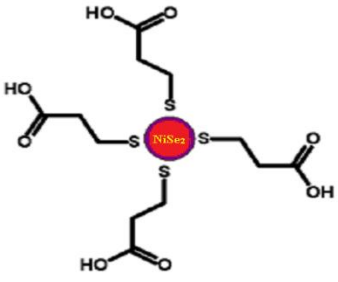

3-MPA-NiSe$_2$QD

Flask C

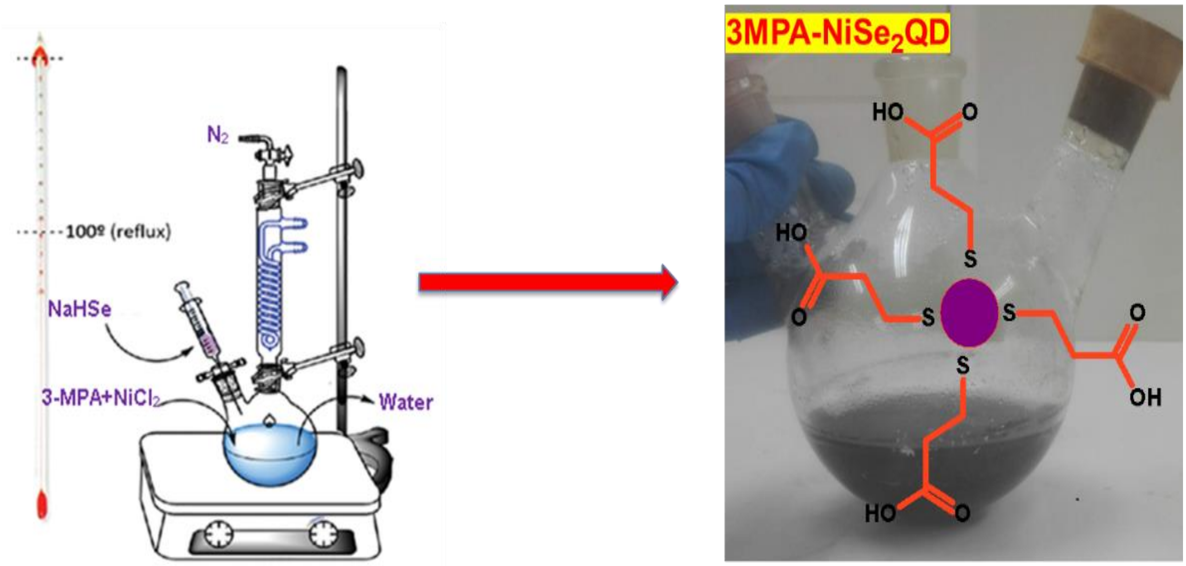

Figure 3. 4. Schematic diagram for the synthesis of 3-MPA- $NiSe_2$QD.

3.7 Electrochemical characterisation

3.7.1 Cleaning electrodes

All electrochemical experiments were carried out on a Palmsens 3 Compact Electrochemical Interfaces Potentiostat. A three-electrode system consisting of a gold working electrode (AuE ~ 0.021 cm^2 diameter), platinum (Pt) wire counter electrode, and Ag/AgCl (3 M NaCl) reference electrode was used. Alumina polishing pads and alumina slurries of (1.0 µm, 0.3 µm and 0.05 µm) (Buehler, Illinois, USA) were used to clean the working electrode. Before use, the working electrode was polished in micro-alumina slurries of 1.0 µm, 0.3 µm, and 0.05 µm, followed by ultrasonication for 5 min in ethanol and water, respectively. The proper way of polishing the working electrode is illustrated in Figure 3.5.

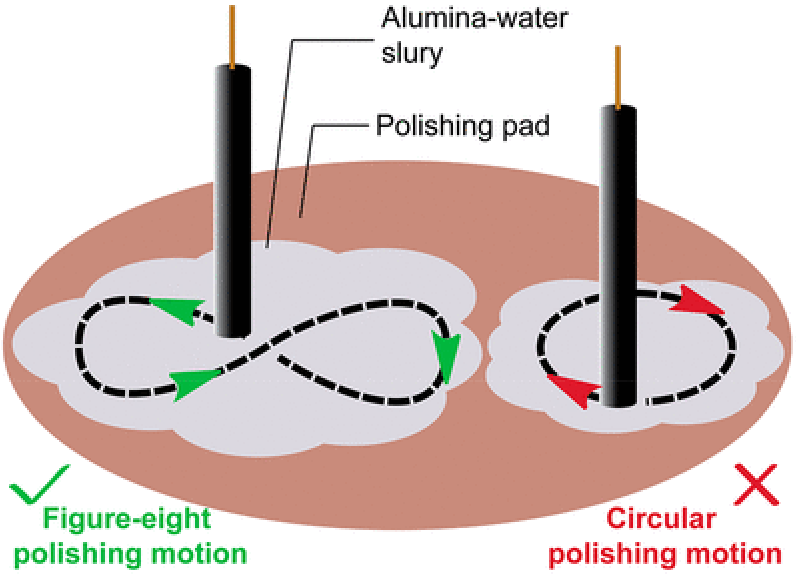

Figure 3. 5. . Simple illustration of the correct way of polishing an electrode [20].

3.7.2 Preparation of L-cysteine monolayer onto the gold electrode surface

After cleaning the electrode as described in section 3.7.1, the electrode was cleaned further electrochemically using a 0.5 M H_2SO_4 solution by running cyclic voltammetry at a scan rate of 50 mVs-^{1} and a potential range from 0 V to 1.5 until reproducible voltammograms were obtained. The L-cysteine/Au modified electrode was formed by drop-casting 20 µL of 0.01 M L-cysteine aqueous solution on the Au electrode. This electrode was kept in the dark for 24 hours to form a monolayer through Au-S covalent bonding. After 24 hours of incubation, the L-cyst/Au was carefully rinsed with water to remove any physically adsorbed L-cyst.

3.7.3 Preparation of the electrochemical sensor

The L-cysteine functionalised Au electrode was activated by drop-casting 10 µL of a 0.01 M mixture (EDC/NHS ratio 1:1) for 30 minutes in the fridge. This was followed by rinsing of the modified electrode and drop-casting 3-MPA-$NiSe_2$QD (4 µL) for 12 h to form 3-MPA-$NiSe_2$QD/L-cyst/Au electrode as illustrated in Figure 3.6. The electrochemical sensor (3-MPA-$NiSe_2$QD/L-cyst/Au) was characterised by differential pulse voltammetry and calibrated for its responses to NVP in 0.1 M phosphate buffer solution (pH 7.4). The calibrated electrochemical sensor was used to determine NVP in real wastewater samples. Diclofenac drug, tenofovir and EDC were used as interfering species to study the selectivity of the sensor.

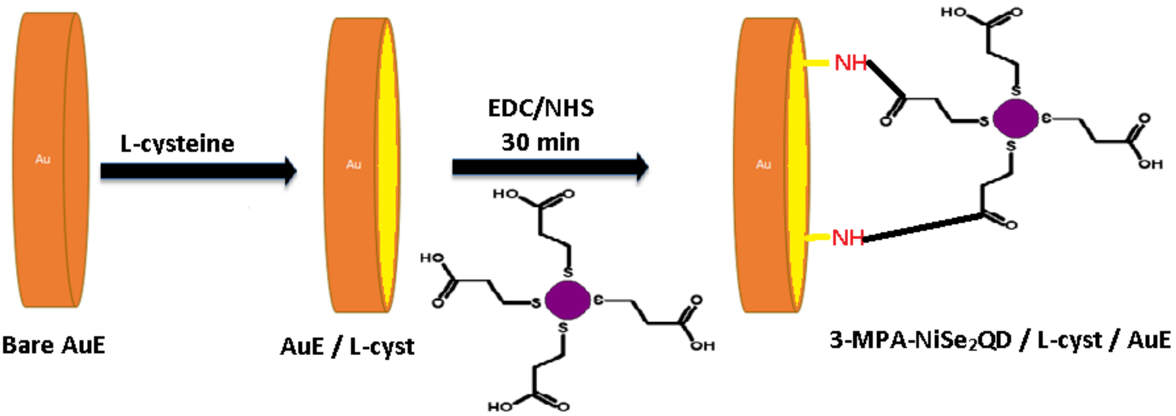

Figure 3. 6. Schematic diagram for the preparation of the electrochemical sensor.

3.7.4 Preparation of the electrochemical sensor using Nafion

Due to the weak interaction observed between the BPE-$NiSe_2$QD and the AuE/L-cyst modified electrode, a binder was then used to prevent the QD from falling off the electrode during analysis. Nafion (5 % w/v solution) was diluted with ethanol to make a 1 % w/v concentration. The AuE was drop-cast with BPE-$NiSe_2$QD (4 µL) and was allowed to dry at room temperature for 12 hours. Thereafter, 2 µL of the Nafion solution was dropped onto the AuE/BPE-$NiSe_2$QD modified electrode and left to air dry for over 12 hours. The Au/BPE-$NiSe_2$QD/Nafion electrochemical sensor was applied for the determination of the NVP drug.

References

1. N. Dhenadhayalan, T. W. Lin, H. L. Lee, and K. C. Lin, ACS Appl. Nano Mater. **1**, 3453 (2018).

2. L. Li, Y. Cheng, Y. Ding, Y. Lu, and F. Zhang, Anal. Methods **4**, 4213 (2012).

3. U. Feleni, U. Sidwaba, H. Makelane, and E. Iwuoha, J. Nanosci. Nanotechnol. **19**, 1 (2019).

4. H. Zheng and L. Wang, Soft Nanosci. Lett. **3**, 29 (2013).

5. P. Mulpur, T. M. Rattan, and V. Kamisetti, J. Nanosci. **2013**, 1 (2013).

6. G. W. Auner, S. K. Koya, C. Huang, B. Broadbent, M. Trexler, Z. Auner, A. Elias, K. C. Mehne, and M. A. Brusatori, Cancer Metastasis Rev. **37**, 691 (2018).

7. F. S. Rocha, A. J. Gomes, C. N. Lunardi, S. Kaliaguine, and G. S. Patience, Can. J. Chem. Eng. **96**, 2512 (2018).

8. R. V. Maikala, Int. J. Ind. Ergon. **40**, 125 (2010).

9. M. Derakhshesh, M. R. Gray, and G. P. Dechaine, Energy and Fuels **27**, 680 (2013).

10. M. Scimeca, S. Bischetti, H. K. Lamsira, R. Bonfiglio, and E. Bonanno, Eur. J. Histochem. **62**, 89 (2018).

11. A. Tonejc, Acta Chim. Solv **46**, 435 (1999).

12. A. Pandey, S. Dalal, S. Dutta, and A. Dixit, J. Mater. Sci. Mater. Electron. **32**, 1341 (2021).

13. S. Nasir, M. Zobir, Z. Zanial, N. Azah, S. Afif, and I. Mustapha, Bioresources **14**, 2352 (2019).

14. L. Alexander and H. P. Klug, J. Appl. Phys. **21**, 137 (1950).

15. D. M. A. M. Luykx, R. J. B. Peters, S. M. Van Ruth, and H. Bouwmeester, J. Agric. Food Chem. **56**, 8231 (2008).

16. A. G. Kikhney and D. I. Svergun, FEBS Lett. **589**, 2570 (2015).

17. A. K. Solanki, Y. S. Rathore, M. D. Badmalia, R. R. Dhoke, S. K. Nath, D. Nihalani, and Ashish, J. Biol. Chem. **289**, 34780 (2014).

18. C. Zhu, G. Yang, H. Li, D. Du, and Y. Lin, Anal. Chem. **87**, 230 (2015).

19. M. Mathew, S. Radhakrishnan, A. Vaidyanathan, and B. Chakraborty, 727 (2021).

20. N. Elgrishi, K. J. Rountree, B. D. McCarthy, E. S. Rountree, T. T. Eisenhart, and J. L. Dempsey, J. Chem. Educ. **95**, 197 (2018).

21. T. Kokila, • P S Ramesh, and • D Geetha, Appl. Nanosci. **5**, 911 (2015).

22. S. Su, J. Mater. Chem. C **3**, 473 (2015).

CHAPTER FOUR

FUNCTIONALIZED NICKEL SELENIDE QUANTUM DOT-ELECTROCHEMICAL SENSOR SYSTEM FOR SENSING NEVIRAPINE IN WASTEWATER

Summary

Semiconductor quantum dots have attracted great interest in research over the past decade due to their peculiar optical and electronic properties. Their extremely small size and electrochemical properties make them a promising platform for sensor applications. The synthesis procedure of some of these QD involves the use of organic molecules to cap the surface atoms. This enhances the stability of the QD. 3-mercaptopropionic acid (3-MPA), a short-chain thiol ligand, has been widely used as a stabilising agent. In this study, 3-MPA was used as a capping agent for $NiSe_2QD$*. This chapter discusses the characterisation of 3-MPA-*$NiSe_2QD$ *and its individual components using various techniques such as UV-Vis, FTIR, SAXSpace, XRD, HR-TEM/SEM, and Raman. It discusses the electrochemical properties of 3-MPA-*$NiSe_2QD$ *and its precursors using DPV in 0.1 M PBS at pH 7.4. Additionally, this chapter discusses the voltammetric responses of the 3-MPA-*$NiSe_2QD$*/L-cyst/Au electrochemical sensor towards nevirapine. For comparison, the detection limit obtained for the electrochemical sensor is compared to those postulated in previous studies.*

4.1 Introduction

The high number of people living with human immunodeficiency virus-acquired immunodeficiency syndrome (HIV/AIDS) in South Africa has led to the implementation of antiretroviral (ARV) treatment programmes globally. Nevirapine (NVP) is one of the most extensively used ARV drug worldwide for the treatment of HIV and the prevention of mother-to-child transmission [1,2]. This drug is classified as a non-nucleoside reverse transcriptase inhibitor (NNRTI). It binds directly and reversibly to the reverse transcriptase enzyme thereby interfering with viral ribonucleic acid (RNA) to deoxyribonucleic acid (DNA) -directed polymerase activities [3–5].

Until now, several analytical methods such as high-performance liquid chromatography (HPLC) [6,7], liquid chromatography coupled to tandem mass spectrometry (LC-MS/MS) [1], gas chromatography with mass spectrometry (GC-MS) [8,9], micellar electrokinetic chromatography (MEKC) [10], spectrophotometry [11] and electrochemical techniques [5,12,13] have been used to quantify NVP in various samples such as pharmaceutical formulations, human serum and wastewater. Amongst these techniques, electrochemical methods have attracted the attention of most researchers because of their simplicity, fast response, cost-effectiveness, high sensitivity and fast alternative to the above-mentioned, mostly expensive and complicated techniques [4,5,14].

Modification of the electrode surfaces can improve the analytical performance of sensors due to the provision of enhanced sensitivity, low detection limits, high stability, wide linear range, and high selectivity which cannot be achieved using bare electrodes [4,15,16]. Among the wide range of materials used for electrode modification, nanomaterials have been widely applied in electrochemical sensors. The remarkable unique and fascinating properties of nanomaterials, which include high surface areas, fast electron transfer between electroactive species and electrocatalysis over the surface helps to enhance the sensitivity and electrochemical stability. [5,17,18]. Quantum dots (QD) particularly have caught the attention of many researchers because of their outstanding reactivity, high optical and electrical properties. QD are semiconductors with size ranges between 2 nm to 10 nm. Their large surface area to volume ratio and high efficiency in the transportation of electrons makes them suitable for the detection of various analytes [19–21].

Functionalisation of the quantum dot surface using capping agents is very important as it improves the optoelectronic properties of the material [22]. This surface modification enhances the stability of the QD and prevents their aggregation to enforce maximum interaction with the target analytes [23]. Some of the functional groups present in the capping agents include the thiol group (-SH), carboxylic acids (-COOH), or amines ($-NH_2$). Among these various functional groups, the thiol group has been reported to successfully passivate II-IV QD due to its high affinity for group II metals ions [24]. Examples of organic compounds containing the thiol group include thioglycolic acid (TGA), mercaptosuccinic acid (MSA), L-cysteine (L-cyst), 3-mercaptopropionic acid (3-MPA) and glutathione (GSH) [24,25]. Amongst these different stabilisers, 3-MPA has been chosen as the source of thiol. 3-MPA has both the -SH and -COOH groups present in its structure. Interestingly, the use of functionalised QD allows for the rapid transfer of electrons to the target analyte resulting in higher charge detaching efficiency [26].

Nickel selenide ($NiSe_2$) has a low resistivity, a narrow bandgap and good electrical conductivity for charge transfer [27–29]. $NiSe_2$ has been reported to have superior electrochemical redox characteristics when compared to other Ni-based compounds [30]. This is due to the electron-rich active sites and the synergistic effect of nickel and selenium [27,30]. Nickel selenide has been intensively used in hydrogen evolution reactions [27,31–35], oxygen evolution reactions [36–40], solar cells [41–47], supercapacitors [48–51] and urea oxidation [52]. Regrettably, to our knowledge, there are few reports documented in the literature on the use of $NiSe_2$QD for electrochemical sensor development and application. However, $NiSe_2$ nanosheets have been utilised as an electrode modifier for a glucose sensor, and a low detection limit of 23 nm and sensitivity of 1.57 µA μM^{-1} cm^{-2} were attained [30]. Hence, this study focused on the development of an electrochemical sensor system based on the 3-MPA-$NiSe_2$QD for the detection of NVP in wastewater samples.

4.2 Results and Discussion

The synthesis of 3-MPA-$NiSe_2$QD was described in Chapter 3 section 3.6 (pages 51-53) and the characterisation in section 3.1 (pages 46-50). Electrochemical characterisation and sensor fabrication were also discussed in sections 3.7.2 and 3.7.3 of Chapter 3 (pages 54-55).

4.2.1 SAXSpace results

Small-angle X-ray scattering spectroscopy (SAXS) was used to investigate the internal structure, particle size and size distribution of the synthesised $NiSe_2$QD material in aqueous media. GIFT software was then used to Fourier-transform the results from SAXS into a pair distance distribution function (PDDF) by volume and size distribution by number as shown in Figure 4.1. The PDDF of the $NiSe_2$QD showed a core-shell structure with a radius of 17 nm and a maximum QD diameter of 59 nm and as depicted in Figure 4.1A (a). The core resembled a globular or spherical shape [53]. In contrast to 3-MPA-$NiSe_2$QD, L-cyst- 3-MPA-$NiSe_2$QD has a maximum radius of 16 nm and shows some shoulder peaks as 4 nm, 8 nm, 24 nm, and 38 nm. An increase in the size of the shell is observed in Figure 4.1A (c). This can be attributed to the presence of more thiol groups present in L-cysteine which may have contributed to further capping of the QD by forming a covalent bond with the metal, or the formation of S-S bonds between the L-cysteine molecules or possibly the formation of amide bonds between the carboxylic acid groups of the 3-MPA-$NiSe_2$QD and the amine groups of the L-cysteine [55]. Figure 4.1B shows the PDDF of (a) L-cyst-NVP and (b) 3-MPA-NiSe$_2$QD-NVP and (c) L-cyst-3-MPA-NiSe$_2$QD-NVP respectively. An overall shift in the lower nm range is observed with the sensor L-cyst-3-MPA-NiSe$_2$QD-NVP and a maximum radius of 15 nm is observed. The rate of transfer of electrons is enhanced by the presence of 3-MPA-NiSe$_2$QD and this agrees with the results obtained in electrochemistry. Figure 4.1C shows the size distribution by number which was calculated using the GIFT program. The data reveals the presence of monodispersed particles with a maximum radius of 6 nm. Even though there are bigger particles showing a maximum radius of 21 nm and 27 nm as shown in insert (x), a comparison of these peaks shows that the first peak has a higher intensity compared to the others. Therefore, this confirms the production of the QD as most of the particles had a maximum radius of 6 nm.

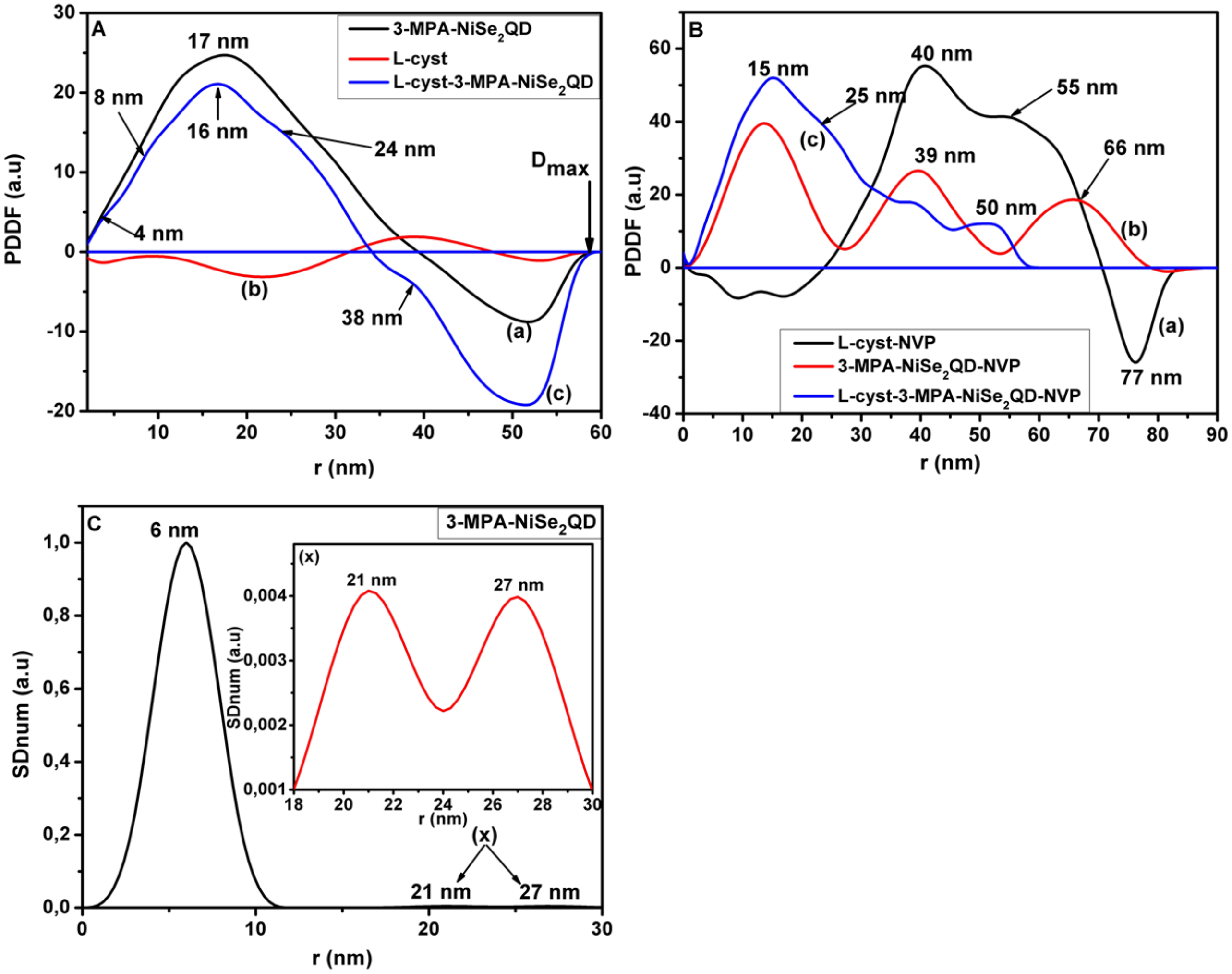

Figure 4. 1. SAXS PDDF results of A: (a) 3-MPA-$NiSe_2$QD, (b)L-cyst and (c) L-cyst-3-MPA-$NiSe_2$QD, B: L-cyst-NVP, (b)) L-cyst-3-MPA-$NiSe_2$QD-NVP and C: particle radius, r, distributed by the number of particles.

4.2.2 UV-Vis and Optical Bandgap

The optical properties of the QD and precursors were investigated by UV-Vis spectrophotometer and photoluminescence spectroscopy. Figure 4.2A shows the optical properties of the precursors used where (a) is $NiCl_2$, (b) 3-MPA, (c) Ni-3-MPA complex and insert (d) reduced Se spectra, respectively. The UV spectra of $NiCl_2$ shows three absorption bands at 395 nm, 656 nm, and 717 nm. These bands confirm the presence of Ni^{2+} ions [56,57]. These results are similar to those obtained for the $[Ni(H_2O)_6]^{2+}$ species at room temperature where the absorbance band between 350 nm and 500 nm is assigned to $^3A_{2g} \rightarrow {}^3T_{1g}$ (P). Interestingly, the $^3A_{2g} \rightarrow {}^3T_{1g}$ band in the region 600 nm to 800 nm is split, producing the main peak at 717 nm and the shoulder peak at 656 nm because of spin-orbit coupling that mixes the $^3T_{1g}$ (F) and ^1E_g states [57,58]. The absorbance spectra of the capping agent in Figure 4.2A (b) shows two absorption bands at 266 nm and 320 nm which may be attributed to the presence of the thiol group and carboxylic acid respectively. Based on the spectra obtained for the Ni-3-MPA (Figure 4.2A (c) complex, it can be concluded that the disappearance of the absorption band at 266 nm confirms the successful capping using the thiol group. The presence of the carboxylic acid groups is signified by the band at 320 nm which is present in both spectra (b) and (c). The insert (d) shows a weak absorbance band at 493 nm for the reduced Se. This may be resulting from Se_2^{2-} species [59]. Nickel selenide is a p-type semiconductor with a bandgap of 620 nm (2.0 eV) [60]. The UV-Vis spectra of 3-MPA capped $NiSe_2$QD (Figure 4.2B) displayed several absorbance bands at 261 nm, 306 nm, 331 nm, 445 nm, and 487 nm respectively. The absorbance band at 261 nm is attributed to the $n \rightarrow \sigma^*$ transition of the thiol group present in 3-MPA while the absorbance band at 306 nm may be ascribed to metal to ligand charge transfer (i.e., nickel ions and 3-MPA capping agent [53,61]. The 3-MPA-$NiSe_2$QD exhibited a signature absorption band at 331 nm corresponding to the energy band gap of 3.91 eV as shown in Figure 4.2C and the bands occurring at 445 nm and 487 nm were assigned to the Se_2^{2-} species of the QD. The estimate of the optical band gap was evaluated using the Tauc equation 4.1 represented by :

$$\alpha h v = k\,(h v - E_g)^{n/2} \qquad (4.1)$$

where α, h, v, k, Eg are absorption coefficients, Planck constant, frequency, proportionality constant and energy bandgap respectively. The value of n equals 1 corresponds to a direct transition.

The bandgap is a very important characteristic of semiconducting material. The bandgap of a nanomaterial is inversely related to its size, i.e. the bandgap decreases as the size of the nanomaterial increases [60,62]. The curves of $(\alpha h\nu)^2$ against hv were plotted and estimates of the band-gap energy were obtained by extrapolation of the curve $(\alpha h\nu)^2 = 0$. The obtained value of 3.91 eV is however slightly larger than that of bulk nickel selenide (2.0 eV) [60]. This is an attribute of the formation of very small-sized particles of less than 5 nm as confirmed by HR-TEM and also due to quantum size effects. However, the material is a semiconductor as its band-gap value is below 4 eV. The PL spectra of 3-MPA-NiSe$_2$QD is shown in Figure 4.2D obtained at an excitation wavelength of 370 nm.

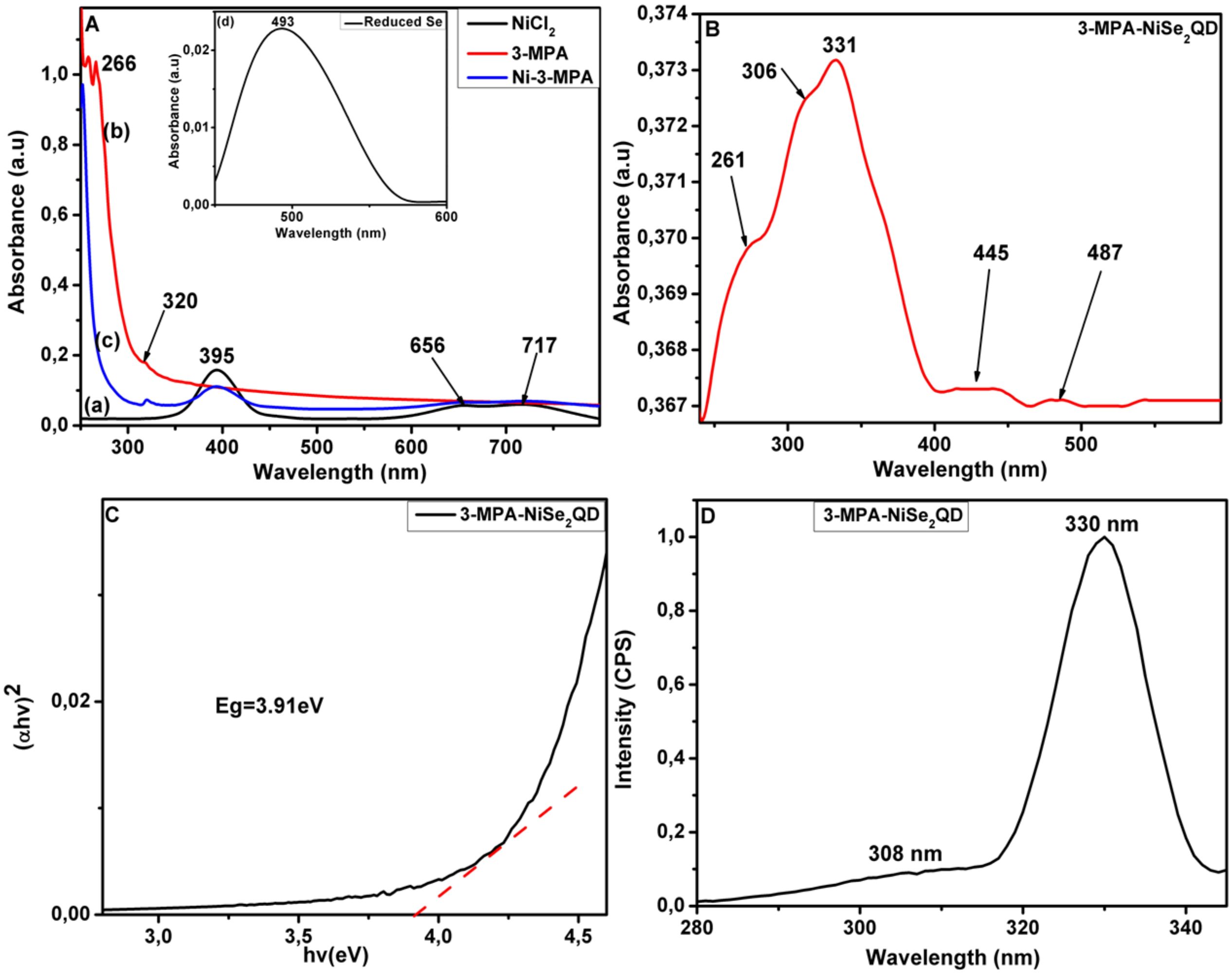

Figure 4. 2. UV-visible absorption spectra of the precursors, B: 3-MPA-$NiSe_2$QD, C: Tauc plot of 3-MPA-$NiSe_2$QD and D: Normalised PL spectra of 3-MPA-$NiSe_2$QD.

4.2.3 FTIR results of 3-MPA- $NiSe_2$QD

FTIR measurements were carried out to elucidate major functional groups present in the capping agents used and their role in stabilising the QD materials. Figure 4.3A shows the FTIR spectra of (a) 3-MPA capping agent and (b) 3-MPA capped $NiSe_2$QD. A broad absorption band is observed in both spectra around 3448 cm^{-1} which is due to the O-H stretching of absorbed water molecules. Four distinct absorption bands appearing at 2924 cm^{-1}, 2569 cm^{-1}, 1691 cm^{-1} and 1402 cm^{-1} are attributed to C-H stretch, S-H stretching of the thiol group, C=O of the vibration of the carboxylic acid group and CH_2 resulting from the carbon chain of 3-MPA capping agent. However, Figure 4.3A (b) displayed the disappearance of the characteristic band due to S-H stretching, indicating the interaction of the thiol group of the capping agent with the core of $NiSe_2$QD. This confirmed the formation of S-NiSe bonds between 3-MPA and the $NiSe_2$ core [53]. The spectra of 3-MPA capped $NiSe_2$QD showed an increase in the absorption peak at 1570 cm^{-1}assigned to the carboxylate anion (COO^-) of the surface ligands [63]. This was formed during the synthesis process when the sodium hydroxide used to adjust the pH to 12 deprotonated the COOH group. The absorption bands between 1242 cm^{-1} and 1002 cm^{-1} are ascribed to C-O stretching. A C-S stretching vibration was observed at 947 cm^{-1} in the spectra of the capping agent.

Further characterisation by FTIR was performed to evaluate the interaction between the (a) L-cyst, (b) 3-MPA-$NiSe_2$QD and (c) L-cyst-3-MPA-$NiSe_2$QD as depicted in Figure 4.3B. The band appearing at 3183 cm^{-1} was assigned to the amine ($-NH_2$) functional group of L-cysteine. The five well-resolved peaks observed at 3446 cm^{-1}, 2992 cm^{-1}, 2543 cm^{-1}, 2082 cm^{-1} and 1612 cm^{-1} were assigned to the stretching vibration of O-H, CH_2, S-H, N-H and C=O respectively [64,65]. The absorption peaks at 1517 cm^{-1}, 1428 cm^{-1} and 1295 cm^{-1} are attributed to the N-H group of the NH_3^+ group of L-cyst, C-N stretch and C-O stretch respectively [66]. The spectra shown in Figure 4.3B (b) was attributed to the successful binding of the capping agent 3-MPA onto the $NiSe_2$ core. The diminution of the band at 2543 cm^{-1} in Figure 4.3B (b) signifies the cleavage of the S-H bond and the formation of NiSe-S bonds at 698 cm^{-1} [64]. There is an overall decrease in the intensity of the bands in Figure 4.3B (c) and a blue shift to lower wavenumbers which may be caused by intramolecular bonding between the carboxylic acid group and the amine group present in L-cysteine. This is evidenced by a decrease in the C=O stretch and the disappearance of the amine group at 3183 cm^{-1}. The appearance of this new amide bond is observed at 1490 cm^{-1} [67].

Figure 4.3C depicts the FTIR spectrum obtained for nevirapine. The characteristic bands appearing between 3296 and 3187 cm^{-1} are attributed to the N-H stretching of the 7 membered rings in NVP. The C-H stretching vibrations of the heteroaromatic ring are shown at 3058 cm^{-1} and C=O stretch in a cyclic amide appears at wavenumber 1643 cm^{-1} [68]. The peaks observed between 1585 cm^{-1} and 1410 cm^{-1} are typical of C-C stretching in the aromatic ring [69]. The bands shown at wavenumbers between 1288 cm^{-1} and 1246 cm^{-1} are due to C-N stretching vibrations for aromatic amines and that seen at 785 cm^{-1} shows C-H bending of aromatic groups [70].

FTIR measurements were performed once more to evaluate the possible interactions between the NVP drug, L-cysteine, and the sensor platform. The results obtained are shown in Figure 4.3D. NVP working solution was prepared by several dilutions of the stock solution using 0.1 M PBS buffer solution. There was no significant change observed in the spectra for the combination of L-cysteine and NVP as shown in Figure 4.3D (a) as no shifting of predominant peaks of L-cysteine was observed. This suggests there are no chemical interactions between the drug and L-cysteine. This is because the L-cysteine forms a monolayer and is not responsible for the detection of the drug. These results are in good agreement with the findings made in electrochemical characterisation. However, a slight difference in the region between 3500 cm^{-1} and 2700 cm^{-1} was observed which may be due to the formation of weaker bonds such as van der Waals' forces, dipole-dipole interaction or hydrogen bonds [71]. Figure 4.3D (b) shows a decrease in intensity and a redshift of the spectra towards higher wavenumbers. A decrease in the C=O stretch at 1638 cm^{-1} was observed. The absorption band at 1574 cm^{-1} may be ascribed to the amide bond formation between the functionalised 3-MPA-$NiSe_2$QD and the L-cysteine with the help of the cross-linking agents. This bond is observed at 1486 cm^{-1} in spectra 4.3D (c). According to Elahe et al. [14], the presence of free amine groups at the surface ensures adsorption of more NVP.

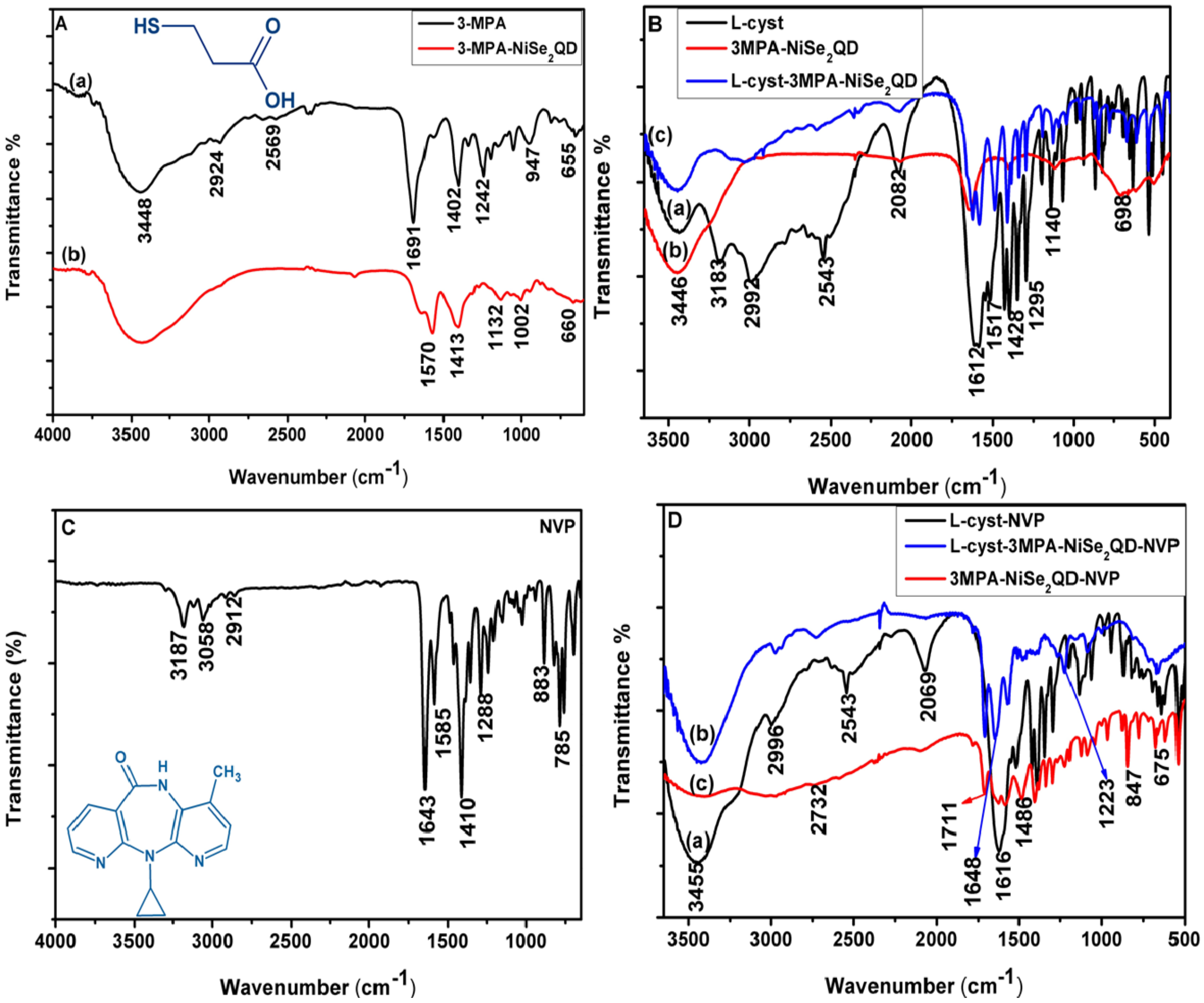

Figure 4. 3. FTIR spectra for A: (a) 3-MPA capping agent, (b) 3-MPA-$NiSe_2$QD and B: (a) L-cyst, (b) 3-MPA-$NiSe_2$QD and (c) L-cyst-3-MPA-$NiSe_2$QD, C: NVP and D: (a)L-cyst-NVP, (b) 3-MPA-$NiSe_2$QD-NVP and (c) L-cyst-3-MPA-$NiSe_2$QD-NVP.

4.2.4 Raman results

The Raman spectra of $NiSe_2$QD were recorded at room temperature in a backscattering configuration excited by a 532 nm line of Ar+ ion laser in the range of 0 to 3500 cm^{-1}. Figure 4.4 shows the spectrum of the as-prepared $NiSe_2$QD capped with 3-MPA. The band observed at 210 corresponds to the stretching mode of the Se-Se pair with symmetries A_g and T_g, where A_g and T_g modes correspond to in-phase and out-of-phase stretching vibrations of the X–X pairs respectively [72–77]. These active modes in $NiSe_2$ with a pyrite-type structure are mainly caused by the intraionic stretching modes of dumb-bell-shaped Se_2 units [73,76]. The band appearing at 490 cm^-

^{1} shows the characteristic longitudinal optical (LO) one-phonon mode of nickel selenide [43] whereas the band appearing at 846 cm^{-1} is characteristic of Si-O-Si from the glass slide which was used as a sample holder [78]. The characteristic band of C-COO^{-} is shown by the band at 1 050 cm^{-1} [79,80]. The stretching vibrations of internal C-C aid to the vibrations observed in the spectra for 3-MPA-NiSe$_2$QD and the band at 1235 cm^{-1} are attributed to twisting CH$_2$ vibrations [81]. C-H stretching is signified by the band at 2700 cm^{-1} [82]. The absence of the S-H stretching mode in the region around 2500 cm^{-1} in Figure 4.4 indicates that the thiol groups are covalently bound to the surface of the QD which confirms the results obtained from FTIR [83].

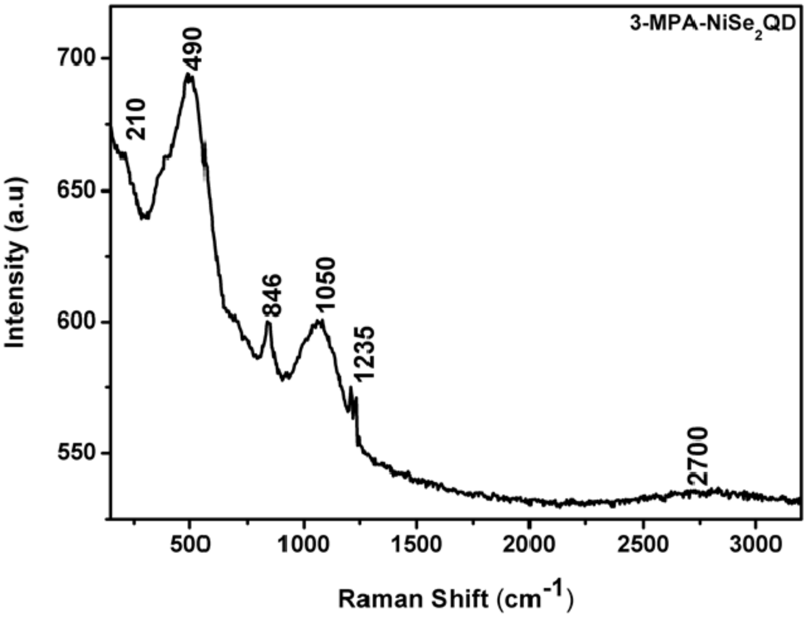

Figure 4. 4. The Raman spectra of 3-MPA-NiSe$_2$QD.

4.2.5 Surface morphology of 3-MPA-NiSe$_2$QD

The SEM micrographs providing the surface morphology and compositional information of 3-MPA-NiSe$_2$QD are shown in Figures 4.5A and B, respectively. Figure 4.5A shows agglomerated spherical particles. The observed agglomeration of the particles may be attributed to the small volume of capping agent used during the preparation of the QD. Elemental composition analysis was investigated using energy-dispersive X-ray spectroscopy (EDX), and it revealed the presence of nickel, selenium, oxygen, carbon and sulphur atoms as shown in Figure 4.5B.

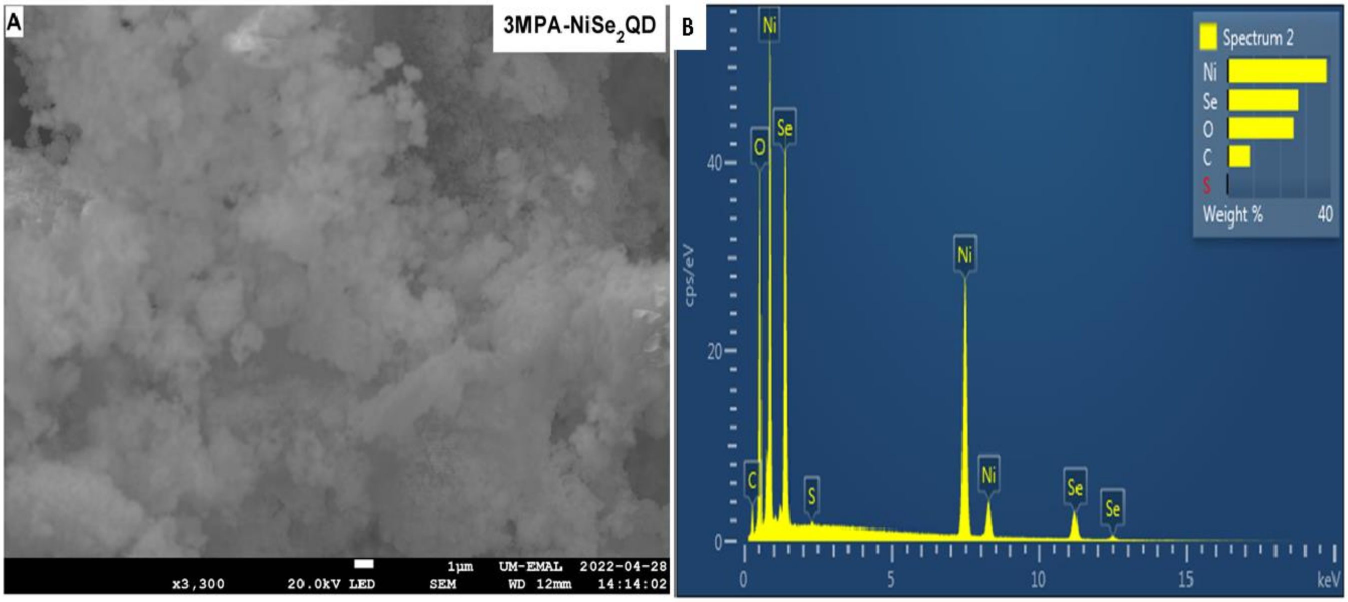

Figure 4. 5. (A) SEM micrograph and (B) EDX spectrum of 3-MPA-NiSe$_2$QD.

4.2.6 TEM/SAED and XRD results

The structural morphology and crystal structure of NiSe$_2$QD were investigated by high-resolution transmission electron microscopy (HR-TEM) and X-ray diffraction (XRD) as depicted in Figure 4.6. The HRTEM images show non-agglomerated, well-dispersed spherical particles with very small sizes of less than 5 nm and well-resolved lattice fringes. The electrostatic repulsion of the negatively charged carboxylate groups present in the capping agent (3-MPA) may have prevented the aggregation of the nanoparticles [26,53]. Additionally, good crystallinity of the 3-MPA-NiSe$_2$QD was confirmed by the presence of the well-resolved lattice fringes shown in the insert (x). The selected area electron diffraction pattern (SAED) in Figure 4.6C indicates crystalline behaviour. The XRD was used to define the crystallinity of the phase of the synthesised QD, and the pattern obtained is shown in Figure 4.6D. The diffraction peaks observed at 2θ values of 25.8, 29.9, 33.6, 37.0, 42.9, 45.7, 50.3, 53.5, 55.6, 57.9 and 62.1° can be indexed to (111), (200), (210), (211), (220), (300), (311), (222), (320), (321) and (400). These diffraction peaks were identified using Joint Committee on Powder diffraction Standards (JCPDS) card no. 96-153-7618 which corresponds to the cubic phase of NiSe$_2$ with a pyrite structure [84–86]. The simulated crystal structure of NiSe$_2$ with the space group P a-3 (205) is shown in Figure 4.6E.

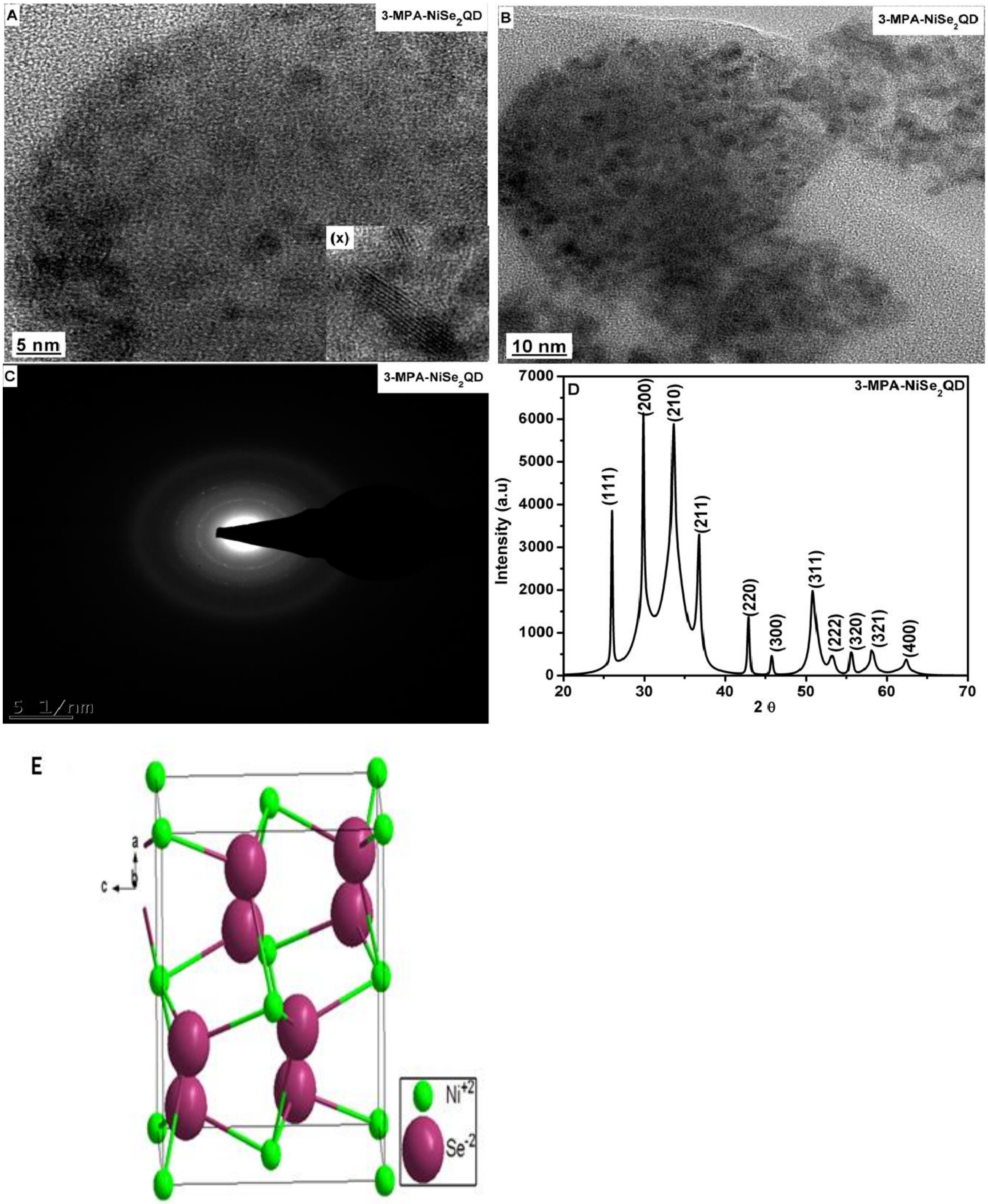

Figure 4. 6. HRTEM micrographs of A, B: 3-MPA- $NiSe_2$QD and (x) inserted (zoomed) region of 3-MPA-$NiSe_2$QD at 5 nm and 10 nm scale view, respectively, C: SAED pattern of 3-MPA-$NiSe_2$QD, D: XRD pattern of 3-MPA-$NiSe_2$QD and E: Simulated crystal structure of $NiSe_2$ (green

= Ni, purple = Se).

4.2.7 Electrochemistry of precursors

Electrochemical studies of the precursors used in the synthesis of the QD were investigated. These studies were conducted so to further understand which components of the QD material were responsible for the obtained oxidation and reduction peaks. Differential pulse voltammetry of $NiCl_2$, reduced selenium (Se^{2-}) in the form of NaHSe, and the capping agent 3-MPA was investigated under the same conditions as the QD. Aqueous solutions of the precursors were spiked into the 0.1 M phosphate buffer at pH 7.40 and the bare AuE was used for their characterisation. The resulting voltammograms are shown in Figure 4.7 A-D. The voltammogram of $NiCl_2$ shown in Figure 4.7A shows 2 oxidation peaks at -0.50 V and shoulder peak at 0.94 V which may be attributed to the one-electron reduction of Ni (II) to Ni (I) and one electron oxidation to Ni (III) respectively. This is similar to the results obtained by Taraszewska and Roslonek when they investigated the electrochemical behaviour of some nickel complexes in acetonitrile solution [87,88]. The reduction of Ni (III) to Ni (II) can be assigned to the cathodic peak at 1.09 V. According to Murray and Margerum [89], the range for the reduction potential of the Ni (III)/ Ni (II) couple varies between 0.79 V and 0.9 V versus the normal hydrogen electrode which is close to the potential achieved in this experiment. The reduction peaks at -0.55 V may be due to the reduction of Ni (II) to Ni (I) and the peak at -0.97 V may be attributed to the reduction of Ni (II) to elemental Ni respectively [90]. The interaction of the capping agent with the gold electrode yielded 2 oxidation peaks and 2 reduction peaks as illustrated in Figure 4.7B. The adsorption of hydroxyl anions appears at very negative potentials and in this case, it is signified by the peak at -1.20 V [91]. The shoulder peak observed at -0.71 V is due to the oxidation of the carboxylic acid group of 3-MPA whereas the enhancement in the gold oxide peak around 0.67 V is due to the interaction of the electrode with the thiol group present in 3-MPA [92]. According to Pacoste et al. [93], the oxidation of the thiol group of 3-MPA contributes to the peak observed around 0.67 V. This results in the formation of thiol radicals ($RS^{\cdot}$) which could then react to form disulphides as illustrated in Equation 4.2 and 4.3. The reduction peaks observed at 0.56 V, -0.44 V, and -1.05 V can be attributed to the reduction of thiols, disulphides, and the gold oxide respectively. This agrees with Roos et al. [94] who stated that the reduction potentials of thiyl radicals are positive whereas those of disulphides are negative in most cases.

$RSH \rightarrow RS^{\cdot} + H^{+} + e^{-}$ (4.2)

$2RS^{\cdot} \rightarrow RS - SR$ (4.3)

The new oxidation peaks appearing at -0.25 V and 0.04 V in Figure 4.7C are attributed to the metal-ligand charge transfer of $NiCl_2$-3-MPA in comparison to the voltammograms of the capping agent and $NiCl_2$ precursors. The cathodic peaks observed are due to the reduction Ni of Ni species as mentioned above. The differential pulse voltammogram of Se (-II) in the form of NaHSe in phosphate buffer solution is depicted in Figure 4.7D. The reduction of Se follows equation 4.4:

$4NaBH_4 + 2Se \leftrightarrow 2NaHSe + Na_2B_4O_7 + 14H_2$ (4.4)

The reaction of the peak occurring at -0.57 V is assigned to the oxidation of Se (-II) shown in equation 4.5 while the oxidation peak at 0.91 V is assigned to the oxidation of Se (0) to Se (IV) as illustrated in equation 4.6 [93,95]. On the other hand, the reduction potentials of 0.17 V and -0.56 V are due to the reduction of Se (IV) to Se (0) and Se (0) to Se (-II) respectively.

$Se^{2-} \leftrightarrow Se_{(s)} + 2e^{-}$ (4.5)

$Se_{(s)} + H_2O \leftrightarrow H_2SeO_3 + 4H^{+} + 2e^{-}$ (4.6)

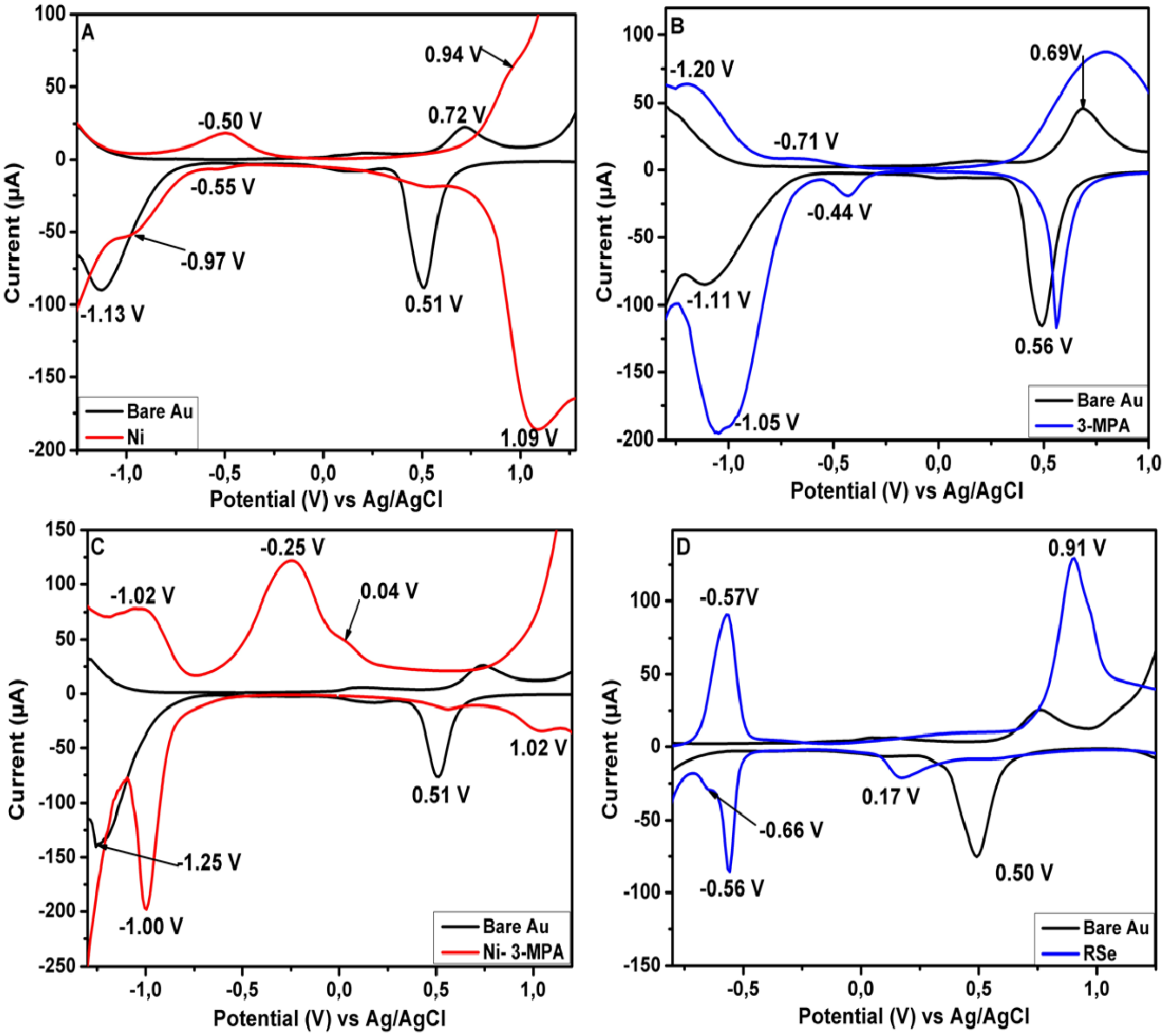

Figure 4. 7. The differential pulse voltammograms of A: $NiCl_2$, B: 3-MPA, C: $NiCl_2$-3-MPA and D: NaHSe in 0.1 M PBS pH 7.4 at 30 mV/s.

4.2.8 Electrochemistry of 3-MPA- $NiSe_2$QD

Electrocatalytic properties of bare Au electrode and 3-MPA-$NiSe_2$QD/L-cyst/Au modified electrode was studied by differential pulse voltammetry (DPV). L-cysteine (L-cyst) was used in the modification of the gold electrode. L-cysteine is a type of amino acid and contains carboxyl, amine, and thiol groups in its structure [96]. The L-cysteine forms self-assembled monolayers over gold surfaces [96]. Figure 4.8 displays the DPV of bare Au (a) and L-cyst/Au. The bare Au shows one anodic peak with a potential of 0.76 V and a peak current of 22 µA. The L-cyst/Au shows an anodic peak at 0.76 V and a peak current of 45 µA. The sharp increase in the peak current is caused by the coupling of the oxidation of the AuE surface to that of S-H in L-cyst forming a strong covalent Au-S bond. The thiol groups have a strong affinity for gold surfaces which explains the observation above [97]. Equation 4.7 shows the adsorption of sulphur onto the gold electrode [98].

$$RSH + Au \leftrightarrow Au - S_{ads} + H^{+} + e^{-} \qquad (4.7)$$

When 3-MPA-$NiSe_2$QD were deposited onto an unmodified gold electrode surface as depicted in Figure 4.8B (b), 2 anodic peaks were observed. In contrast, 5 anodic peaks were observed when 3-MPA-$NiSe_2$QD were deposited onto L-cyst/Au modified electrode shown in Figure 4.8B (c). This may be because, in the absence of the monolayer formed by L-cysteine, the QD were falling off the electrode. Hence a monolayer prevented the QD from falling off the electrode by forming strong amide bonds between some free carboxylic acid groups in 3-MPA-$NiSe_2$QD and free amine groups in L-cysteine. Water-soluble carbodiimide (EDC) and an active ester compound N-hydroxysuccinimide (NHS) were used as crosslinking agents to couple carboxylic acid groups to primary amines to form the peptide bond [99,100]. The five anodic peaks were observed at E_{pa} = -0.39 V (peak A_1), -0.22 V (peak A_2), 0.29 V (peak A_3), 0.56 V (peak A_4) and 0.76 V (peak A_5), respectively. For peaks (A_1), A_2 and A_3, the observed anodic peaks were attributed to the Ni^{2+} generated from the oxidation of the QD and the interaction between the metal to ligand charge transfer ($NiCl_2$-3-MPA). A shift in the selenium oxidation from 0.91 V to 0.56 V in comparison to the starting material precursor was observed hence peak A_4 is characteristic of oxidation Se^{0} of the QD [93]. This is similar to the results obtained by Gaponic et al. [101] where the anodic current peaks observed around 0.62 V was attributed to Se in Au/ZnSe. The peak at 0.76 V is due to the oxidation of $NiSe_2$QD. It should be noted that peak A_5 is overlapping with that of the gold oxide as shown in Figure 4.8B (a). Interestingly, the enhancement seen in the current compared to that of the Bare electrode is due to the fast electron transfer contribution from the presence of $NiSe_2$QD on the surface of the electrode. On the other hand, five reduction peaks were observed at E_{pc} = 1.11 V (peak C_1), 0.51 V (peak C_2), 0.02 V (peak C_3), and -0.55 V (peak C_4) and -1.01 V (peak C_5), respectively. The reduction peak at 1.11 V is due to the reduction of Ni (III) to Ni (II). Peak C_2 was also present in the reduction of the gold oxide. However, peak C_3 can be due to the reduction of Se (IV) to Se (0) and this is similar to the cathodic peak observed by Gaponic et al. [101] which was attributed to the electrodeposition of selenium. The peak denoted C_4 may be the characteristic reduction of the $NiSe_2$QD.

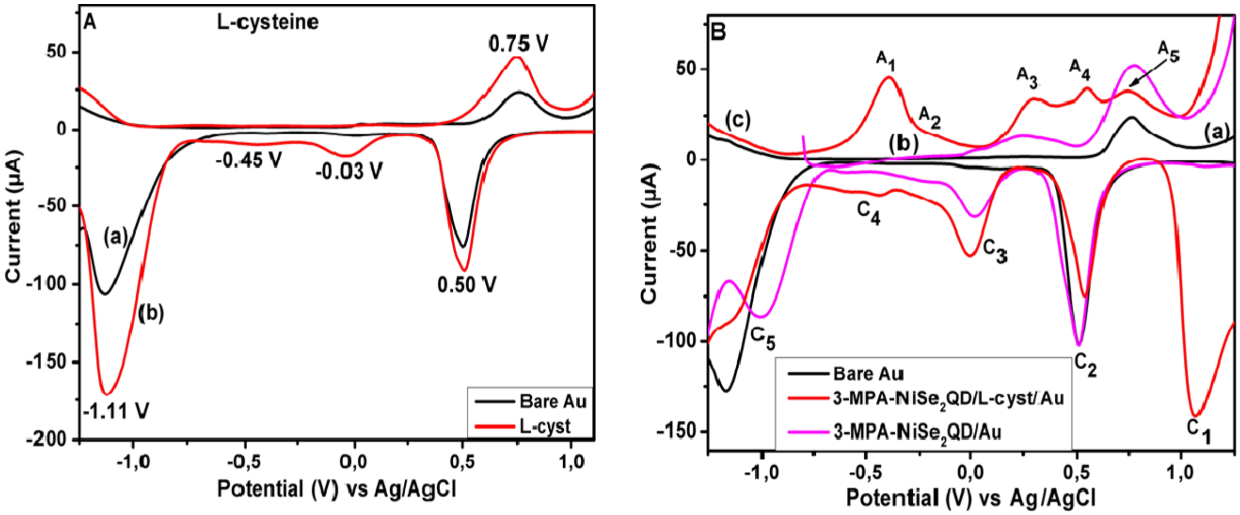

Figure 4. 8. Differential pulse voltammograms A: (a) Bare Au and (b) L-cyst/Au and B: (b)3MPA-$NiSe_2QD$/Au and (c) 3MPA-$NiSe_2QD$/L-cyst/Au in 0.1 M PBS pH 7.4 at 30 mV/s.

4.2.9 Preliminary studies for NVP detection

Various experiments were conducted to evaluate the possibility of NVP detection by the Bare AuE or the L-cysteine modified AuE. When 10 nM of NVP solution was spiked into the cell with L-cyst/Au under aerobic conditions as shown in Figure 4.9A, no significant change was observed in the oxidation peak current. This confirms that L-cyst is not responsible for the detection of NVP. On the other hand, when the Bare AuE was used, an insignificant increase in the current was noted. However, this change was too small. Interestingly, when the L-cyst/AuE was modified with the 3-MPA-$NiSe_2QD$ shown in Figure 4.9B, an increase in the signal was observed and a shift to less positive potential indicating fast electron transfer. Therefore, the 3-MPA-$NiSe_2QD$/L-cyst/Au can be applied for the detection of NVP.

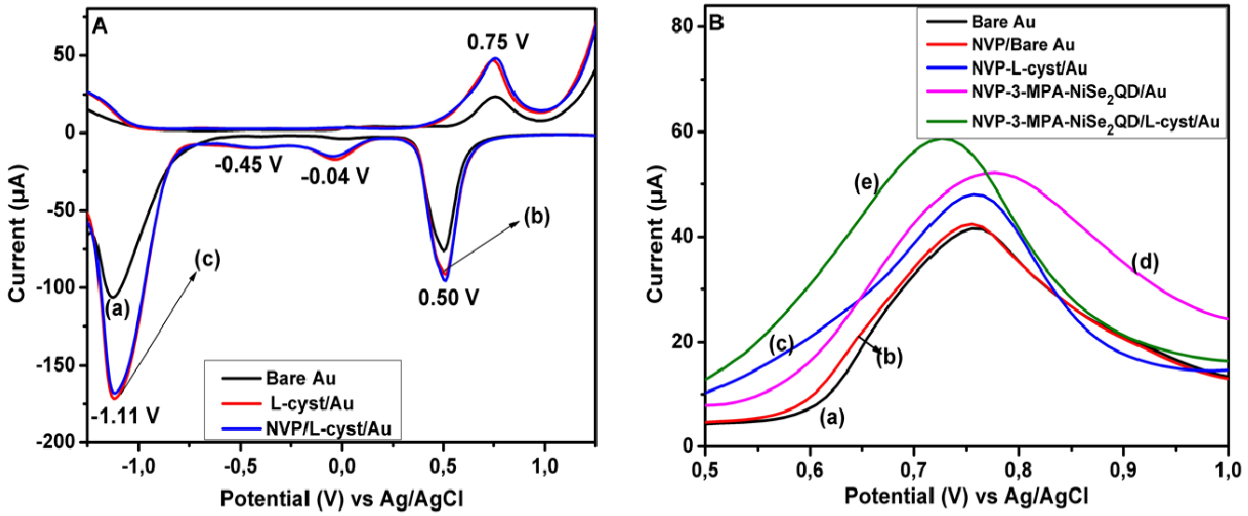

Figure 4. 9. Differential pulse voltammograms A: (a)Bare Au, (b) L-cyst/Au and (c) NVP/L-cyst/Au B: (a) Bare Au, (b) NVP/Bare Au, (c) NVP-L-cyst/Au (d) NVP-3MPA-NiSe$_2$QD/Au (e) NVP-3MPA-NiSe$_2$QD/L-cyst/Au in 0.1 M PBS pH 7.4 at 30 mV/s.

4.2.10 pH studies

The effects of pH on the electrochemical response of 3-MPA-NiSe$_2$QD/L-cyst/Au toward the detection of 10 nM nevirapine were studied using DPV at pH range values ranging from 4.0 to 9.0 in 0.1 M PBS. As illustrated in Figure 4.10A, the oxidation peak current increased from pH 4.0 to pH 7.0 and then decreased at pH 9.0. Interestingly, the oxidation peak potential shifted negatively and the peak current enhanced between pH 4.0 and pH 7.0. The best response was obtained under neutral conditions. Therefore, pH 7.4 phosphate buffer solution was selected for further studies. The peak potential was affected by the pH of the buffer solution as shown in Figure 4.10B. A linear relationship was established between E_{pa} and pH which can be expressed with the following equation 11:

$$E_{pa}(V) = -0.0661pH + 1.1174\ (R^2 = 0.8776) \qquad (11)$$

The slope value of -66.1 mV/ pH obtained for nevirapine is in close proximity to -59 mV / pH, the theoretical value. It is an indication of the participation of an equal number of protons and electrons in the oxidation of nevirapine at the surface of the electrode [14,16,18]. This is similar to the results obtained by Apath et al. [15].

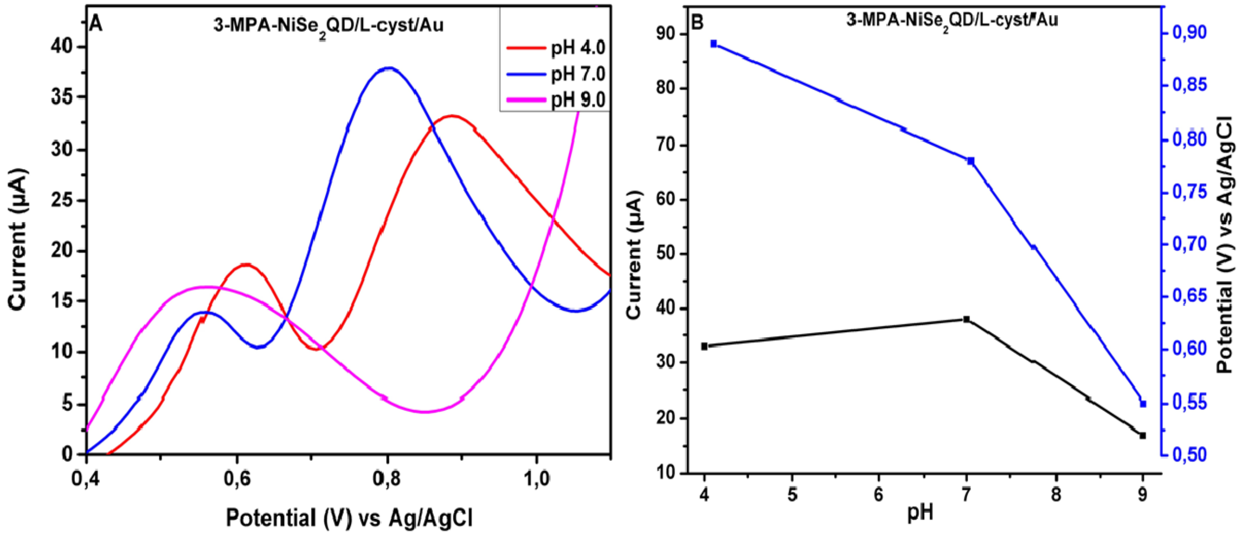

Figure 4. 10. A: DPV responses of 3-MPA-NiSe$_2$QD/L-cyst/Au to 10 nM NVP at different pHs in 0.1 M PBS and B: effect of solution pH on the oxidation peak current and potential.

4.2.11 Electrocatalytic responses of the electrochemical sensor

The influence of the scan rate on the electrochemical response of 10 nM NVP at 3-MPA-NiSe$_2$QD/L-cyst/Au was investigated in the range of 5 to 50 mV/s in PBS (0.1 M, pH 7.40), presented in Figure 4.11A. As it is seen, the peak current increases with an increase in the scan rate and an overall shift to negative potentials was observed. Therefore, 30 mV/s was chosen as the scan rate for this study. Figure 4.11B shows the differential pulse voltammetric responses of the sensor in the absence and presence of nevirapine under aerobic conditions. The potential was scanned from 0.5 V to 1.0 V as shown by the voltammograms. Nevirapine exhibited an irreversible oxidation peak in PBS (pH 7.4). The cathodic peak current at 0.76 V increased steadily to a maximum value until the point of saturation was reached when different concentrations of nevirapine were added as depicted in Figure 4.11C. This also resulted in a remarkable enhancement of the cathodic peak together with a slight shift to less positive potential. Figure 4.11D shows a dynamic linear range (DLR) of 0.08 pM – 1.21 pM and the sensor's sensitivity was determined to be 6.15 µA/pM. The limit of detection (LOD) was calculated according to the data obtained in the straight-line equation and using equation 4.8 below:

$$LOD = \frac{3 \; X \; SD}{m} \qquad (4.8)$$

Where SD is an estimate of the standard deviation and m is the slope. The LOD was found to be 0.013 pM (0.0035 ng/L).

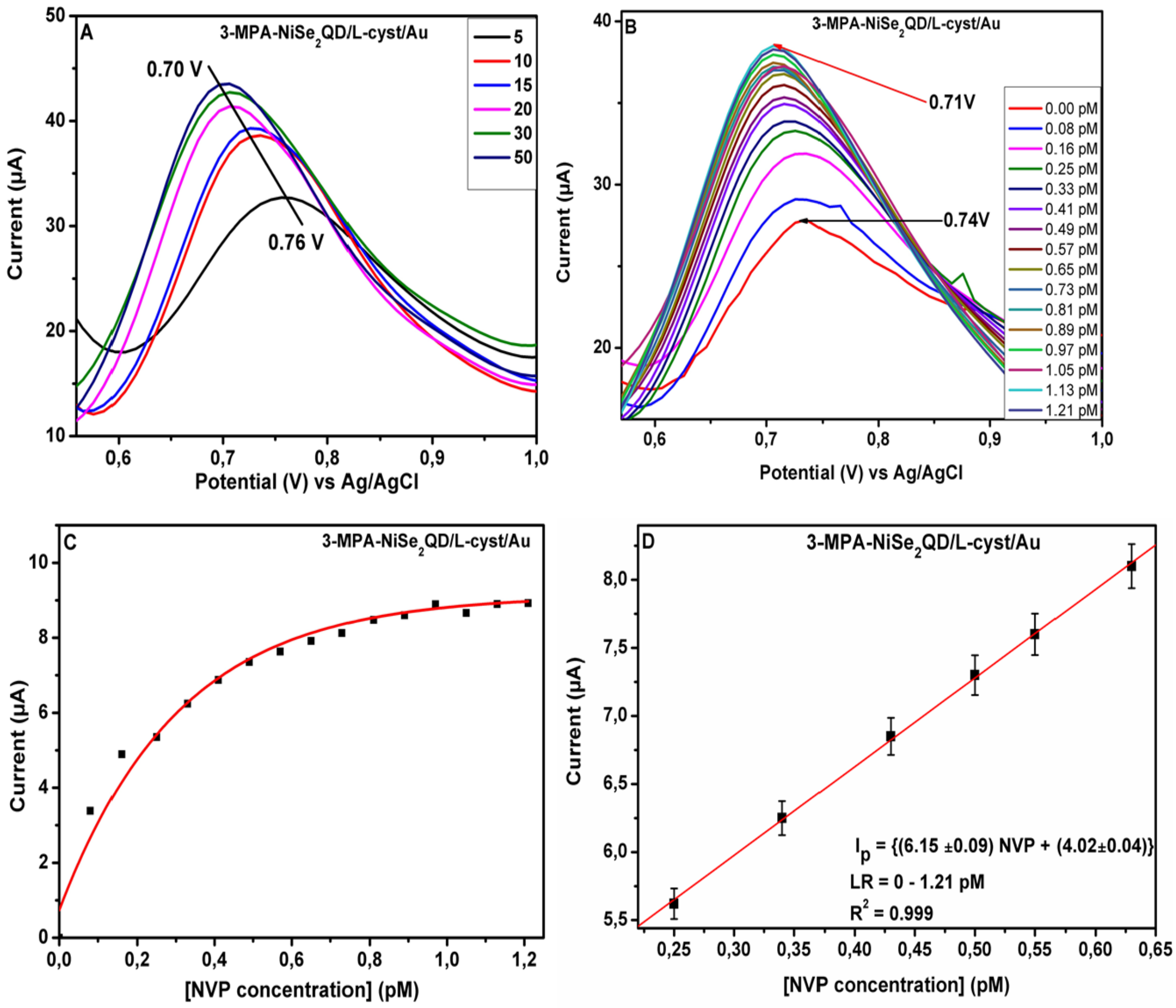

Figure 4. 11. A: Investigation of scan rate, B: DPV responses of 3-MPA-NiSe$_2$QD/L-cyst/Au to NVP in 0.1 M PBS (pH 7.4) at 30 mV/s, C: Exponential curve and D: calibration curve drawn from the linear region of the sensor system.

4.2.12 Interference study

The resistance to interference is one of the most important studies that is required for sensor application. To evaluate the selectivity of the 3-MPA-NiSe$_2$QD/L-cyst/Au sensor, the effect of some potential interferents on the determination of 10 nM nevirapine was investigated. The interferents applied include tenofovir an HIV antiretroviral drug that belongs to the class of nucleoside reverse transcriptase inhibitors (NRTIs). It is used in combination therapy and also in the treatment of hepatitis B [102]. A commonly used anti-inflammatory drug diclofenac (DCF)

[103] and 1-ethyl-3-(3-dimethyl aminopropyl) carbodiimide hydrochloride (EDC) a carbodiimide used as a cross-linking agent to yield amide bonds were also employed as interfering species. As shown in Figure 4.12, the electrochemical response of the 3-MPA-NiSe$_2$QD/L-cyst/Au sensor showed no significant change in the peak current in the potential window 0.5 V to 1.0 V in the presence of the interfering species. It was found that these compounds are oxidized at different potentials and hence do not interfere with NVP detection. However, a slight enhancement observed in the DPV signal may be attributed to the presence of the same functional groups such as the imine (C=N) or methyl (CH$_3$), similarity in chemical structure (presence of 6 membered rings with nitrogen as a substituent) or similar electrochemical behaviours. Thus, the proposed sensor is free from interference,therefore, it is suitable for nevirapine detection in real samples.

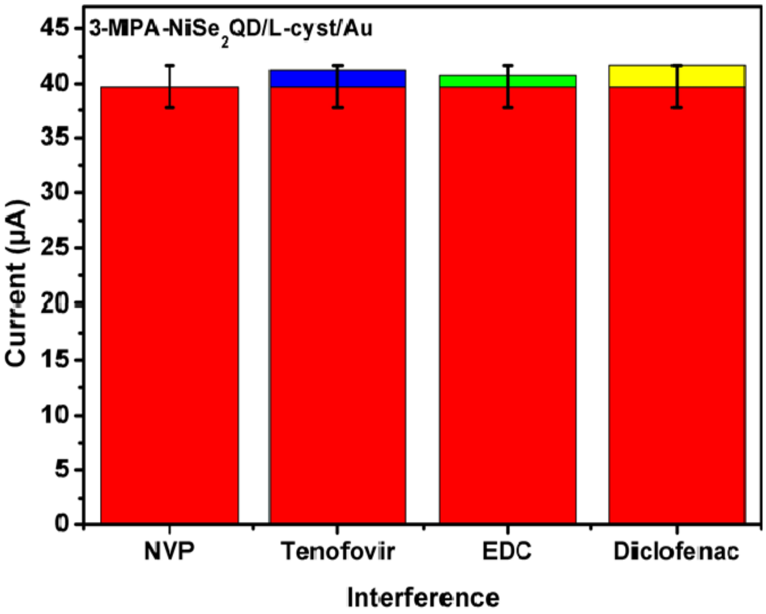

Figure 4. 12. Peak current responses of 10 nM NVP in the presence of interfering species (I0 µM Tenofovir, 1 mM EDC and 10 µM Diclofenac).

4.2.13 Stability study

The storage stability of the 3-MPA-NiSe$_2$QD/L-cyst/Au sensor was examined by DPV in 0.1 M PBS (pH 7.4) containing 10 nM nevirapine. Two storage conditions were investigated. The sensor was stored in the dark at room temperature for 9 days for the first experiment and the results obtained from Figure 4.13A show that the peak current of the sensor decreased to 67 % of the initial response. Remarkably, in another experiment where it was stored in the refrigerator at 4 °C, the results illustrated in Figure 4.13B show that the sensor retained 84 % of its initial response after 9 days. Therefore, storing the sensor in the refrigerator is much better as it helps maintain the integrity of the sensor. These results indicate that the sensor was stable for nevirapine detection. sor.

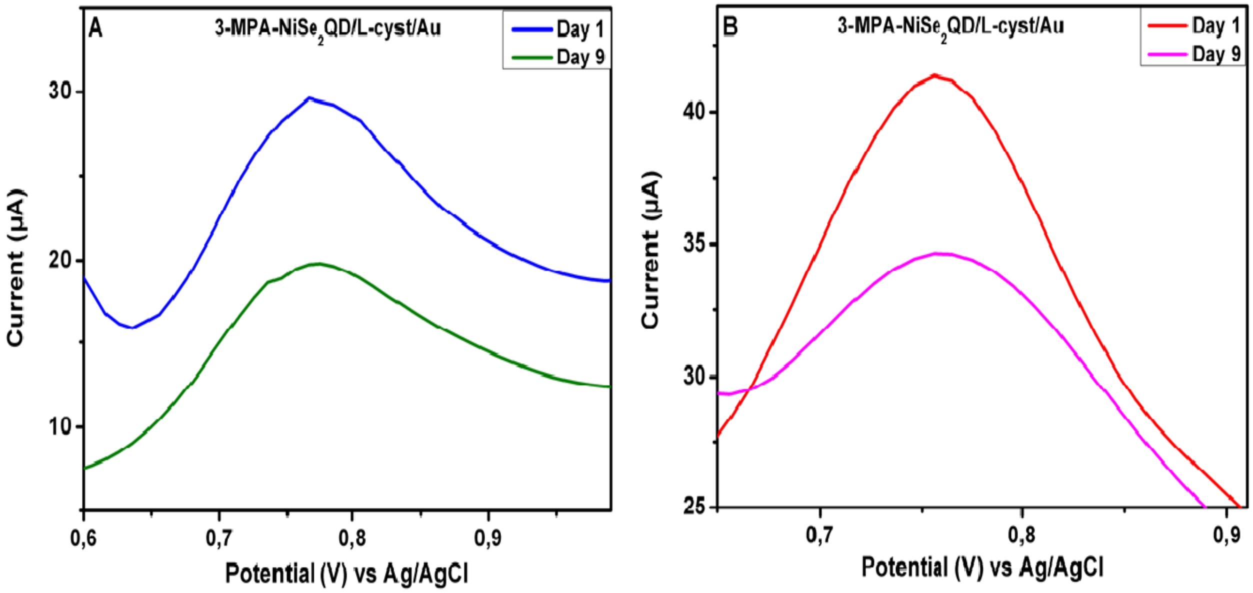

Figure 4. 13. A: DPV responses of 3-MPA-NiSe$_2$QD/L-cyst/Au to 10 nM nevirapine at day 1 and day 9 after storage in the dark at room temperature and B: results for day 1 and day 9 after storage at 4 °C.

4.2.14 Application in real samples

In order to prove the applicability of the proposed sensor in real samples, the 3-MPA-NiSe$_2$QD/L-cyst/Au electrode was used to detect nevirapine concentration in wastewater effluent (Northern wastewater effluent, 26-04-2021) spiked with NVP. Figure 4.14 shows a typical voltammogram for the responses obtained for three samples. The recovery values obtained for the spiked NVP samples 1, 2 and 3 were 99.7 %, 101 % and 99.8 % respectively as shown in Table 4.1. These results prove that the sensor is suitable for real sample applications.

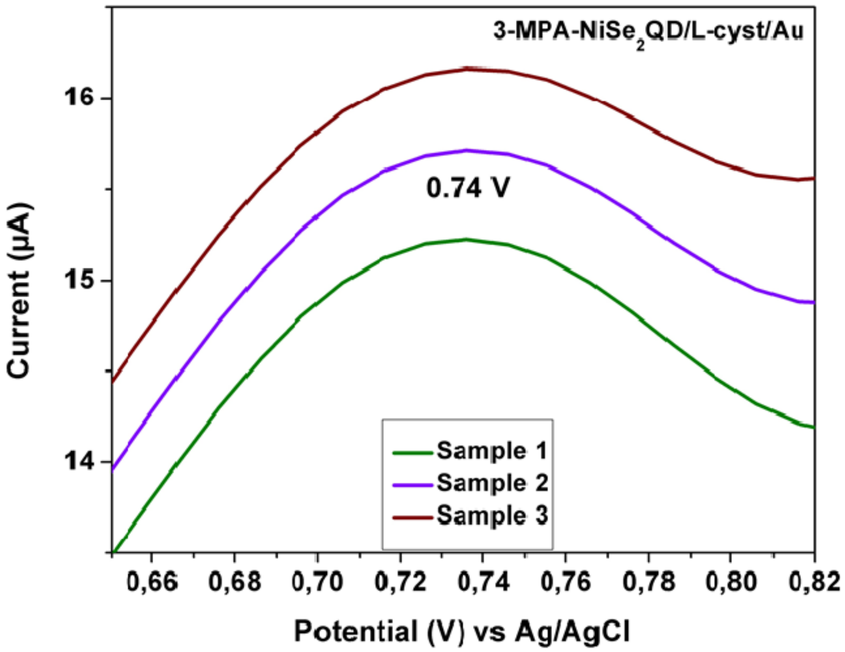

Figure 4. 14. DPV response of 3-MPA-NiSe$_2$QD/L-cyst/Au on successive addition of NVP from 0.33 pM to 0.65 pM in Northern wastewater effluent.

Table 4. 1: Determination of NVP in real wastewater samples.

Real waste water sample	**NVP added (pM)**	**NVP Found ± SD (pM)**	**Recovery (%)**	**% RSD**
1	0.33	0.329 ± 0.020	99.7	0.65
2	0.49	0.493 ± 0.015	101	0.42
3	0.65	0.649 ± 0.024	99.8	0.56

Conclusion

This work presents the fabrication of a novel 3-MPA-NiSe$_2$QD/L-cyst/Au electrochemical sensor for the selective detection of NVP in 0.1 M PBS Buffer, pH 7.40. The newly modified sensor significantly improved the analytical performance because of the presence of 3-MPA-NiSe$_2$QD which enhanced the catalytic activity by promoting fast electron transfer. The fabricated sensor showed high sensitivity and selectivity, low detection limit, high reproducibility, and reasonable stability under optimised conditions. The overall performance of this remarkable electrochemical sensor was way better than previously reported sensors as seen in Table 2.7 (Chapter 2, section

2.6). The proposed sensor was successfully used in the determination of NVP in real wastewater samples with satisfactory results.

References

1. P. Fan-Havard, Z. Liu, M. Chou, Y. Ling, A. Barrail-Tran, D. W. Haas, and A. M. Taburet, Antimicrob. Agents Chemother. **57**, 2154 (2013).

2. O. A. Abafe, J. Späth, J. Fick, S. Jansson, C. Buckley, A. Stark, B. Pietruschka, and B. S. Martincigh, Chemosphere **200**, 660 (2018).

3. M. M. R. De Maat, A. D. R. Huitema, J. W. Mulder, P. L. Meenhorst, E. C. M. Van Gorp, and J. H. Beijnen, Br. J. Clin. Pharmacol. **54**, 378 (2002).

4. S. Shahrokhian, R. Kohansal, M. Ghalkhani, and M. K. Amini, Electroanalysis **27**, 1989 (2015).

5. M. Bagher, E. Ahmadi, and M. Haseli, Anal. Biochem. **527**, 4 (2017).

6. W. Samee, S. Vorarat, P. Srilamai, S. Ongart, R. Suwannaratana, and C. Sornchaithawatwong, Thai Pharm. Heal. Sci. J. **2**, 39 (n.d.).

7. B. Fan and J. T. Stewart, J. Liq. Chromatogr. Relat. Technol. **24**, 3017 (2001).

8. M. Vogel, N. Bertram, J. C. Wasmuth, J. Emmelkamp, J. K. Rockstroh, and C. Reichel, J. Chromatogr. Sci. **48**, 91 (2010).

9. P. Lemmer, S. Schneider, M. Schuman, C. Omes, V. Arendt, J.-C. Tayari, L. Fundira, and R. Wennig, Ther. Drug Monit. **27**, 521 (2005).

10. R. Sekar and S. Azhaguvel, Chromatographia **67**, 389 (2008).

11. T. V. Sreevidya and B. Narayana, Eclet. Quim. **35**, 93 (2010).

12. F. Zhang, L. Li, L. Luo, Y. Ding, and X. Liu, J. Appl. Electrochem. **43**, 263 (2013).

13. N. L. TERADAL, S. N. PRASHANTH, and J. SEETHARAMAPPA, J. Electrochem. Sci. Eng. **2**, 67 (2012).

14. E. Ahmadi, M. Reza, V. Riahifar, and H. Momeneh, Microchem. J. **146**, 1218 (2019).

15. D. Apath, M. Moyo, and M. Shumba, J. Chem. **2020**, 1 (2020).

16. S. Massumi, E. Ahmadi, A. Akbari, and M. B. Gholivand, J. Electroanal. Chem. **876**, 114508 (2020).

17. S. Menon, S. Jesny, and K. G. Kumar, Talanta **179**, 668 (2018).

18. N. L. Teradal and J. Seetharamappa, Electroanalysis **27**, 2007 (2016).

19. M. Pedrero, S. Campuzano, and J. M. Pingarrón, J. AoaC Int. **100**, (2017).

20. K. D. Wegner and N. Hildebrandt, Chem. Soc. Rev. **44**, 4792 (2015).

21. P. Mulpur, T. M. Rattan, and V. Kamisetti, J. Nanosci. **2013**, 1 (2013).

22. N. Dhenadhayalan, T. W. Lin, H. L. Lee, and K. C. Lin, ACS Appl. Nano Mater. **1**, 3453 (2018).

23. L. Li, Y. Cheng, Y. Ding, Y. Lu, and F. Zhang, Anal. Methods **4**, 4213 (2012).

24. A. Singh, V. S. Tripathi, S. Neogy, and M. C. Rath, Mater. Chem. Phys. **214**, 320 (2018).

25. P. Nurerk, P. Kanatharana, and O. Bunkoed, Luminescence **31**, 515 (2016).

26. P. M. Ndangili, A. M. Jijana, P. G. L. Baker, and E. I. Iwuoha, J. Electroanal. Chem. **653**, 67 (2011).

27. K. S. Bhat and H. S. Nagaraja, Int. J. Hydrogen Energy **43**, 19851 (2018).

28. A. Panneerselvam, M. A. Malik, M. Afzaal, P. O’brien, and M. Helliwell, J. AM. CHEM. SOC **130**, 2420 (2008).

29. W. Maneeprakorn, C. Q. Nguyen, M. A. Malik, P. O’Brien, and J. Raftery, J. Chem. Soc. Dalt. Trans. 2103 (2009).

30. S. Mani, S. Ramaraj, S. M. Chen, B. Dinesh, and T. W. Chen, J. Colloid Interface Sci. **507**, 378 (2017).

31. F. Wang, Y. Li, T. A. Shifa, K. Liu, F. Wang, Z. Wang, P. Xu, Q. Wang, and J. He, Angew. Chemie Int. Ed. **55**, 6919 (2016).

32. T. Wang, X. Li, Y. Jiang, Y. Zhou, L. Jia, and C. Wang, Electrochim. Acta **243**, 291 (2017).

33. H. Zhou, Y. Wang, R. He, F. Yu, J. Sun, F. Wang, Y. Lan, Z. Ren, and S. Chen, Nano Energy **20**, 29 (2016).

34. P. Xu, J. Zhang, Z. Ye, Y. Liu, T. Cen, and D. Yuan, Appl. Surf. Sci. **494**, 749 (2019).

35. M. R. Gao, Z. Y. Lin, T. T. Zhuang, J. Jiang, Y. F. Xu, Y. R. Zheng, and S. H. Yu, J. Mater. Chem. **22**, 13662 (2012).

36. A. T. Swesi, J. Masud, and M. Nath, Energy Environ. Sci. **9**, 1771 (2016).

37. J. Zhang, B. Jiang, J. Zhang, R. Li, N. Zhang, R. Liu, J. Li, D. Zhang, and R. Zhang, Mater. Lett. **235**, 53 (2019).

38. Z. Wang, J. Li, X. Tian, X. Wang, Y. Yu, K. A. Owusu, L. He, and L. Mai, ACS Appl. Mater. Interfaces **8**, 19386 (2016).

39. Z. Zou, X. Wang, J. Huang, Z. Wu, and F. Gao, J. Mater. Chem. A **7**, 2233 (2019).

40. J. Du, A. Yu, Z. Zou, and C. Xu, Inorg. Chem. Front. **5**, 814 (2018).

41. H. Wu, Y. Wang, L. Zhang, Z. Chen, C. Wang, and S. Fan, J. Alloys Compd. **745**, 222 (2018).

42. P. Wei, J. Li, Z. Hao, Y. Yang, X. Li, C. Jiang, and L. Liu, Appl. Surf. Sci. **492**, 520 (2019).

43. V. Murugadoss, J. Lin, H. Liu, X. Mai, T. Ding, Z. Guo, and S. Angaiah, Nanoscale **11**, 17579 (2019).

44. P. Wei, J. Li, H. Kang, Y. Yang, Z. Hao, X. Chen, D. Guo, and L. Liu, Int. J. Energy Res. **44**, 845 (2020).

45. V. Murugadoss, P. Panneerselvam, C. Yan, Z. Guo, and S. Angaiah, Electrochim. Acta **312**, 157 (2019).

46. Q. Jiang, K. Pan, C. S. Lee, G. Hu, and Y. Zhou, Electrochim. Acta **235**, 672 (2017).

47. X. Qian, H. Li, L. Shao, X. Jiang, and L. Hou, ACS Appl. Mater. Interfaces **8**, 29486 (2016).

48. S. Li, W. Cai, X. Ma, J. Zhu, and Y. Wang, Int. J. Electrochem. Sci **15**, 2923 (2020).

49. L. Du, W. Du, Y. Zhao, N. Wang, Z. Yao, S. Wei, Y. Shi, and B. Zhang, J. Alloys Compd. **778**, 848 (2019).

50. L. Wu, L. Shen, T. Wang, X. Xu, Y. Sun, Y. Wang, Y. Zhao, Y. Du, and W. Zhong, J. Alloys Compd. **766**, 527 (2018).

51. S. Wu, Q. Hu, L. Wu, J. Li, H. Peng, and Q. Yang, J. Alloys Compd. **784**, 347 (2019).

52. P. Xiong, X. Ao, J. Chen, J. G. Li, L. Lv, Z. Li, M. Zondode, X. Xue, Y. Lan, and C. Wang, Electrochim. Acta **297**, 833 (2019).

53. U. Feleni, U. Sidwaba, H. Makelane, and E. Iwuoha, J. Nanosci. Nanotechnol. **19**, 1 (2019).

54. S. Su, J. Mater. Chem. C **3**, 473 (2015).

55. M. P. Bilibana, U. Feleni, A. R. Williams, and E. Iwuoha, Processes **9**, 1 (2021).

56. N. Nowrouzi and M. Zarei, Tetrahedron **71**, 7847 (2015).

57. N. Zhang, J. Brugger, B. Etschmann, Y. Ngothai, and D. Zeng, PLoS One **10**, 1 (2015).

58. W. Liu, A. Migdisov, and A. Williams-Jones, Geochim. Cosmochim. Acta **94**, 276 (2012).

59. H. Rojo, A. C. Scheinost, B. Lothenbach, A. Laube, E. Wieland, and J. Tits, Dalt. Trans. **47**, 4209 (2018).

60. N. Moloto, M. J. Moloto, N. J. Coville, and S. Sinha Ray, J. Cryst. Growth **324**, 41 (2011).

61. L. J. Yang, Q. L. Liu, M. X. Wang, L. S. Gu, Y. H. Luo, and B. W. Sun, Spectrochim. Acta - Part A Mol. Biomol. Spectrosc. **166**, 1 (2016).

62. A. Sobhani, M. Salavati-Niasari, and F. Davar, Polyhedron **31**, 210 (2012).

63. R. H. Ellerbrock and H. H. Gerke, J. Plant Nutr. Soil Sci. **184**, 388 (2021).

64. L. Li, L. Liao, Y. Ding, and H. Zeng, RSC Adv. **7**, 10361 (2017).

65. S. Devi, B. Singh, A. K. Paul, and S. Tyagi, Anal. Methods **8**, 4398 (2016).

66. S. Wei, C. Guo, L. Wang, J. Xu, and H. Dong, Sci. Rep. 1 (2021).

67. Y. Ji, X. Yang, Z. Ji, L. Zhu, N. Ma, D. Chen, X. Jia, J. Tang, and Y. Cao, ACS Omega **5**, 8572 (2020).

68. B. A. Witika and R. B. Walker, Pharmazie **74**, 91 (2019).

69. K. Sowjanya, K. Shobha Deepthi, and A. Bharathi, Int. J. Pharm. Pharm. Sci. **4**, 368 (2012).

70. J. Ramkumaar, G.R, Srinivasan, S., Bhoopathy, T.J., Gunasekaran, S., Charles and J. and Ramesh, J. Theor. Appl. Phys. **7**, 1 (2013).

71. R. Maji, N. S. Dey, B. S. Satapathy, B. Mukherjee, and S. Mondal, Int. J. Nanomedicine **9**, 3107 (2015).

72. B. Mohanty, B. K. Jena, M. Kandasamy, N. Dalai, R. K. Sahu, R. M. Kadam, B. Chakraborty, and B. Jena, Sustain. Energy Fuels **4**, 3058 (2020).

73. H. Fan, M. Zhang, X. Zhang, and Y. Qian, J. Cryst. Growth **311**, 4530 (2009).

74. C. de las Heras and F. Agullo-Rueda, J. Phys. Condens. Matter **12**, 5317 (2000).

75. T. Wang, D. Gao, W. Xiao, P. Xi, D. Xue, and J. Wang, Nano Res. **11**, 6051 (2018).

76. J. Yang, G. H. Cheng, J. H. Zeng, S. H. Yu, X. M. Liu, and Y. T. Qian, Chem. Mater. **13**, 848 (2001).

77. X. Teng, J. Wang, L. Ji, Y. Lv, and Z. Chen, Nanoscale **10**, 9276 (2018).

78. A. Jitianu, G. Amatucci, and L. C. Klein, J. Mater. Res. **23**, 2084 (2008).

79. M. Moskovits and J. S. Suh, J. Am. Chem. Soc. **107**, 6826 (1985).

80. A. Kudelski, Surf. Sci. **502**–**503**, 219 (2002).

81. J. L. Castro, M. R. López-Ramírez, J. F. Arenas, and J. C. Otero, J. Raman Spectrosc. **35**, 997 (2004).

82. R. W. Berg, Appl. Spectrosc. Rev. **50**, 193 (2015).

83. M. S. Abd El-Sadek, J. R. Kumar, and S. Moorthy Babu, Int. J. Nanoparticles **2**, 20 (2009).

84. and M. T. Adachi, Kengo, Kiyoo Sato, J. Phys. Soc. Japan **26**, 631 (1969).

85. C. Zhao, Y. Zhu, W. Liu, Z. Chen, Z. Wang, and P. Feng, J. Solid State Chem. **266**, 37 (2018).

86. S. Furuseth, A. Kjekshus, A. F. Andresen, V. Nordal, A. A. Lindberg, and J. C. Craig, Acta Chem. Scand. **23**, 2325 (1969).

87. J. Taraszewska, G. Rosłonek, and B. Korybut-Daszkiewicz, J. Electroanal. Chem. **297**, 245 (1991).

88. D. C. Olson and J. Vasilevskis, Inorg. Chem. **8**, 1611 (1969).

89. D. . Murray, C.K, and Margerum, Inorg. Chem. **22**, 463 (1983).

90. R. S. Ningthoujam, N. S. Gajbhiye, and S. Sharma, Pramana - J. Phys. **72**, 577 (2009).

91. T. Łuczak, J. Appl. Electrochem. **37**, 653 (2007).

92. M. Rodriguez, H. J. Ciro, J. Salcedo, and T. Serna, Rev. Mex. Ing. Química **12**, 505 (2020).

93. L. C. Pacoste, A. N. Jijana, U. Feleni, and E. Iwuoha, ChemistrySelect **5**, 4994 (2020).

94. G. Roos, F. De Proft, and P. Geerlings, Chem. - A Eur. J. **19**, 5050 (2013).

95. S. Fierro, T. Watanabe, K. Akai, M. Yamanuki, and Y. Einaga, Int. J. Electrochem. **2012**, 1 (2012).

96. G. A, A. NF, and E.-A. EH, Talanta **93**, 264 (2012).

97. U. Feleni, U. Sidwaba, N. Ntshongontshi, L. Wilson, and E. Iwuoha, 68 (2020).

98. D. G. Wierse, M. M. Lohrengel, and J. W. Schultze, J. Electroanal. Chem. **92**, 121 (1978).

99. Eric Valeur and Mark Bradley, Chem. Soc. Rev. **38**, 606 (2009).

100. M. Di Marco, S. Shamsuddin, K. A. Razak, A. A. Aziz, C. Devaux, E. Borghi, L. Levy, and C. Sadun, Int. J. Nanomedicine **5**, 37 (2010).

101. N. Gaponik, S. K. Poznyak, N. P. Osipovich, A. Shavel, and A. Eychmüller, Microchim. Acta **160**, 327 (2008).

102. K. Childs, D. Joshi, R. Byrne, M. Bruce, I. Carey, K. Agarwal, and C. Taylor, Aids **27**, 1443 (2013).

103. D. Vogna, R. Marotta, A. Napolitano, R. Andreozzi, and M. D'Ischia, Water Res. **38**, 414 (2004).

CHAPTER FIVE

BANANA EXTRACT-BASED METAL CHALCOGENIDE FOR NEVIRAPINE WASTEWATER ELECTROOXIDATION

Summary

In recent years, the green synthesis of nanoparticles has received a lot of attention. Various plant elements, such as leaves, roots, stems, flowers, and microbes, are used in the green route of nanoparticle synthesis. This chapter summarises the results of employing banana peel extract as a $NiSe_2QD$ *capping agent. The synthesised BPE-*$NiSe_2QD$ *are also characterised using spectroscopic, microscopic, and electrochemical methods in this chapter. It also provides an overview of the application of the BPE-*$NiSe_2QD$*-based electrochemical sensor system for the detection of nevirapine drug.*

5.1 Introduction

The use of microbes or plants in the synthesis of nanomaterials is a cost-effective, biologically safe, and environmentally friendly method. The plants or plant extracts used in the green synthesis of nanomaterials are more favourable than biological methods. This is because the synthesis process is very simple, it can be scaled up for large-scale production, and it does not involve the intricate process of cell culturing and maintenance [1,2]. The plant extracts act as reducing and capping agents for the nanoparticles. Several reports have been documented on the synthesis of different nanoparticles such as gold, silver, and platinum by plant parts like leaves, fruit, peels [3,4], lemon extracts [5], bark, and roots [6,7].

Bananas are one of the most consumed fruits worldwide. They are available all year round in tropical and sub-tropical regions [8,9]. Banana peels are discarded as waste after consumption of the pulp, and they have found application in various processes. They have been used for the adsorption of heavy metals from water, in the production of fungal biomass, in ethanol fermentation and for medicinal purposes [1,3,9]. Previous studies report that the peel is a good source of antioxidants and various phytochemical compounds such as phenolic acids, flavonoids and alkaloids [3,8,10–13]. Gopi et al. stated that the major components of the banana peel include cellulose, hemicellulose, some proteins, lignin, and pectin, which are mainly found in plant cell walls [2,14,15]. Other compounds found in ripe banana peels include anthocyanins and catecholamines [11,12]. Some of these biological compounds are shown in scheme 5.1.

The present study aims to fabricate a $NiSe_2$QD-based electrochemical sensor system for the detection of NVP in wastewater samples. The synthesis of $NiSe_2$QD involves the use of an extract derived from banana peels as a capping agent. Functional groups such as hydroxyls (-OH), carboxylic acids (-COOH), and amine groups (-NH) have been reported to be present in the banana peel extract. These are capable of successfully passivating the QD, resulting in non-agglomerated and stable QD [16,17]. The synthesis procedure and the characterisation techniques have been discussed in Chapter 3.

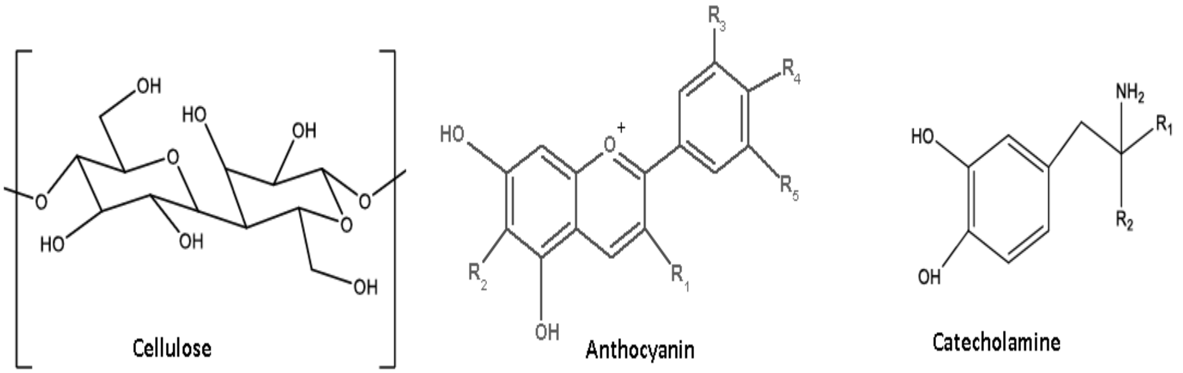

Scheme 5.1 showing examples of biological compounds that may be present in banana peel extract.

5.2 Results and Discussion

The synthesis of BPE-$NiSe_2$QD was described in Chapter 3 section 3.6 (pages 51-53) and the characterisation in section 3.1 (pages 46-50). Electrochemical characterisation and sensor fabrication were also discussed in sections 3.7.4 of Chapter 3 (page 55).

5.2.1 Internal structure of BPE-$NiSe_2$QD

The internal structure, particle size, and size distribution of the synthesised BPE-$NiSe_2$QD were evaluated using Small-angle X-ray scattering (SAXS). The GIFT software was then used to Fourier-transform the results from SAXS into a pair distance distribution function (PDDF) by volume and size distribution by number, as shown in Figure 1A. The PDDF of the QD in Figure 5.1A (a) showed that the maximum QD radius was 58 nm. The QD presented a spherical shape, which corresponds to the results obtained from HRSEM and HRTEM [18]. A shoulder peak was seen on the spectrum for BPE-$NiSe_2$QD at 47 nm, which is an indication of the agglomeration of smaller particles that formed larger particles. The presence of a small shell may have resulted from the BPE which was used as a capping. The awkward spectrum for L-cysteine alone is depicted in Figure 5.1A (b). A combination of BPE-$NiSe_2$QD and L-cyst showed in (c) has signatures at 20 nm and 42 nm, which are attributed to the QD and L-cysteine, respectively. The PDDF of L-cyst-NVP in Figure 5.1B (a) showed 2 peaks at 40 nm arising from L-cyst and at 55 nm arising from the drug and the presence of a shell at 77 nm. FTIR analysis revealed no interaction between these two components. A shift to lower radius values was observed for BPE-$NiSe_2$QD-NVP and L-cyst-BPE-$NiSe_2$QD-NVP as depicted in Figures 5.1B (b) and (c), respectively. This observation was brought about by the presence of the BPE-$NiSe_2$QD. In relation to electrochemistry, the QD accelerated the rate of electron transfer between the analyte and the electrode, which is practically similar to these findings. However, the spectrum for BPE-$NiSe_2$QD-NVP experienced the greatest shift compared to that of L-cyst-BPE-$NiSe_2$QD-NVP. This could be attributed to the weak type of bonding that exists between L-cysteine and the QD, an observation made during electrochemical analysis. Lastly, Figure 5.1C shows the size distribution by number for BPE-$NiSe_2$QD. The majority of the QD have a maximum radius of 6 nm, even though there are particles with larger sizes of 21 nm and 31 nm, as shown in the insert (x), a zoomed area of graph C. This may have arisen from the agglomeration of smaller particles, as also observed in Figure 5.1A (a).

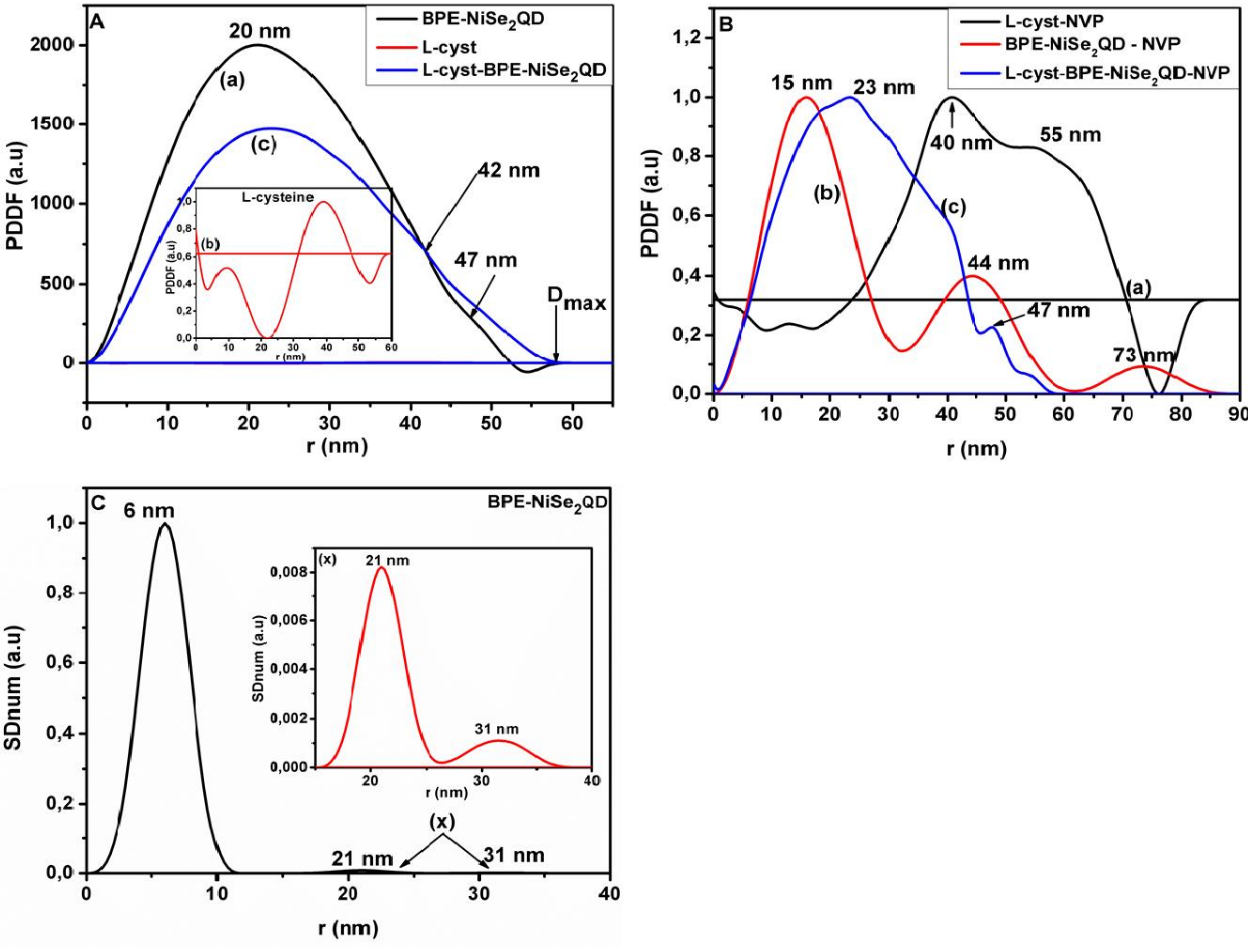

Figure 5. 1. SAXS free model PDDF results of A: (a) BPE-NiSe$_2$QD, (b)L-cyst and (c) L-cyst-BPE-NiSe$_2$QD, B: L-cyst-NVP, (b)) L-cyst-BPE-NiSe$_2$QD-NVP and C: particle radius, r, distributed by the number of particles.

5.2.2 Structural properties of BPE- NiSe$_2$QD

FTIR analysis, as illustrated in Figure 5.2A, was used to identify some characteristic functional groups present in the banana peel extract. As expected, there were various functional groups present in the extract due to its complex nature. As shown in Figure 5.2A (a), a broad peak observed at 3436 cm^{-1} represents the stretching of the hydroxyl groups characteristic of polyphenolic compounds. The stretching vibrations of aliphatic C-H or CH$_2$ groups derived from carbohydrates are shown by the band at 2920 cm^{-1} [19]. The absorption band around 1625 cm^{-1} can be attributed to C=C in aromatic rings [4,20]. The band around 2368 cm^{-1} in both spectra may be due to the stretching of CO$_2$ molecules existing in the atmosphere [21]. Furthermore, peaks between 1386 cm^{-1} and 1112 cm^{-1} were assigned to the C-O stretch in carboxylic acids, phenols, alcohols, or esters [15,20]. The presence of aromatic rings is further confirmed by the band around 774 cm^{-1} [19]. Band shifting to higher wavenumbers and the increase in intensity for the BPE-capped NiSe$_2$QD shown in Figure 5.2A (b) was an indication that BPE has been successfully utilised as a capping agent.

Figure 5.2B shows the FTIR spectrum of (a) L-cysteine, (b) the synthesised BPE-capped NiSe$_2$QD and (c) the combination of L-cyst-BPE-NiSe$_2$QD, respectively. It is evident from these spectra that L-cysteine binds with the BPE-NiSe$_2$QD. It is seen from this figure that the peak at 2544 cm^{-1}, which is due to S-H stretching, is present in the FTIR spectra of L-cysteine, while absent in that of L-cyst-BPE-NiSe$_2$QD. This confirms the binding of the sulphur atom of L-cysteine to the Ni atom of BPE-NiSe$_2$QD. The broad absorption band observed in all the spectra between 3400 cm^{-1} and 3100 cm^{-1} corresponds to the overlap of O-H and N-H stretching modes. Interestingly, the band shown at 2 992 cm^{-1}, which corresponds to C-H stretching modes, is only seen in the spectra for L-cysteine. Other weak bands located at 1620 cm^{-1} indicate the C=O band of L-cysteine and the weak band at 1590 cm^{-1} are due to C=C stretching modes in BPE-NiSe$_2$QD, respectively. The C-C stretching modes present in an aromatic ring are shown at 1492 cm^{-1} and 1407 cm^{-1}. Band shifting to lower wavenumbers and the decrease in the intensity of the bands is observed in Figure 5.2B (c). Intramolecular bonding between the carboxylic acid group and the amine group present in L-cysteine may be responsible for this observation.

Interactions between NVP, L-cysteine and the L-cyst-BPE-NiSe$_2$QD sensor platform were studied using FTIR as shown in Figure 5.2C. Very little change was observed in the spectra for the combination of L-cysteine and NVP, which can be seen in the region between 3500 cm^{-1} and 3100 cm^{-1} in Figure 5.2C (a). These small changes may be ascribed to a weak type of bonding taking place, such as hydrogen bonding. However, band shifting to higher wavenumbers was observed in Figure 5.2C (b) and (c) FTIR spectra for BPE-NiSe$_2$QD-NVP and L-cyst-BPE-NiSe$_2$QD-NVP, respectively. A decrease in the intensity of the bands is noted, and the appearance of a shoulder peak at 1710 cm^{-1} for spectra 5.2C (c). The broadening of peaks at 1241 cm^{-1} and 1094 cm^{-1} may be caused by the presence of C-N and C-O stretches. The formation of amide bonds between the L-cysteine and the BPE-NiSe$_2$QD could have made it possible for the interaction with the drug to take place. This is in line with the findings that were made by Elahe and his co-workers [22].

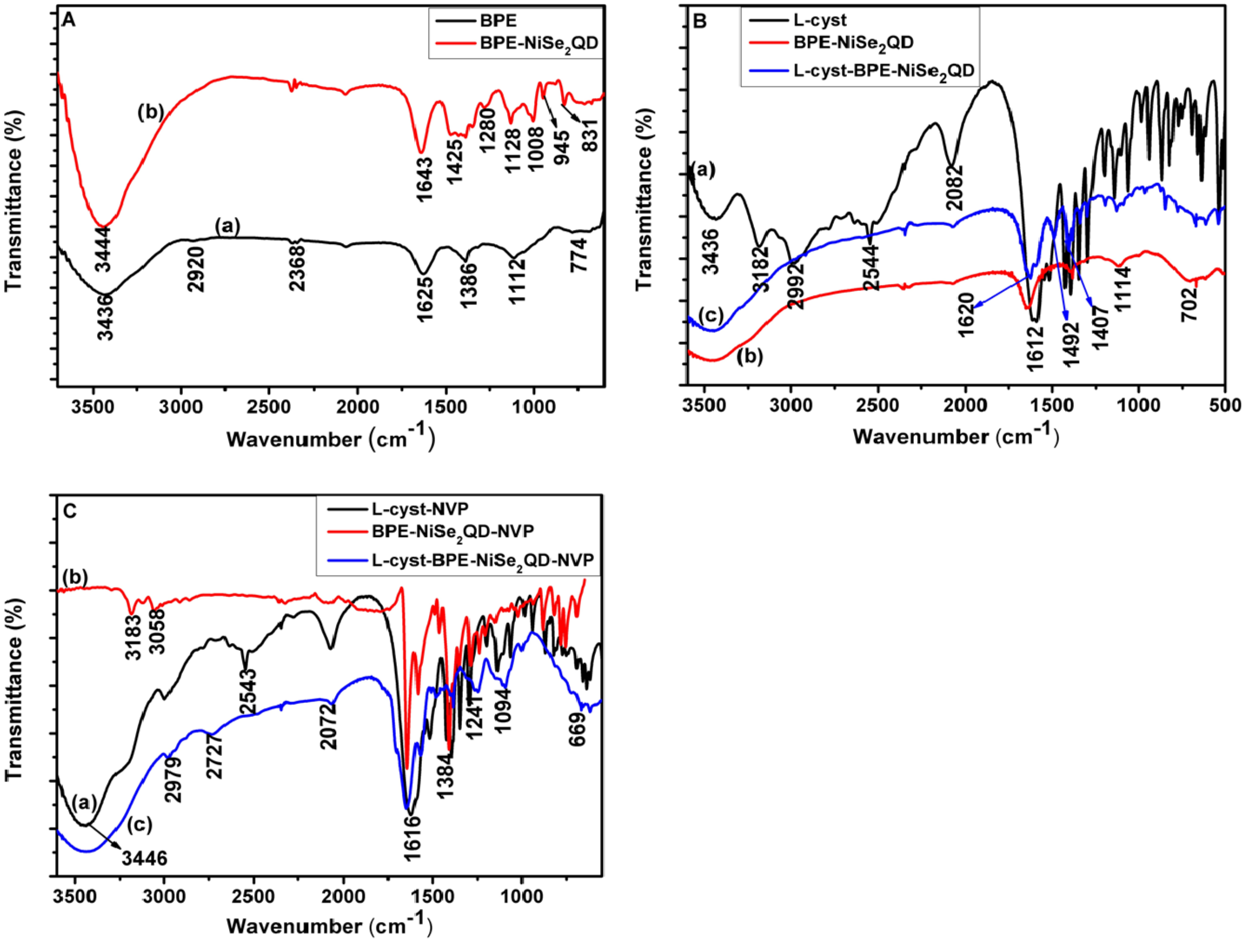

Figure 5. 2. FTIR spectra of A: (a) BPE capping agent, (b) BPE-NiSe$_2$QD and B: (a) L-cyst, (b) BPE-NiSe$_2$QD and (c) L-cyst-BPE-NiSe$_2$QD and C: (a) L-cyst-NVP, (b) BPE-NiSe$_2$QD-NVP and (c) L-cyst-BPE-NiSe$_2$QD-NVP.

5.2.3 Raman spectroscopy analysis

Figure 5.3A shows the Raman spectra of BPE-NiSe$_2$QD, which looks quite similar to the one obtained for 3-MPA capped NiSe$_2$QD in Chapter 4 (section 4.2.4). The stretching mode of the Se-Se pair with symmetries Ag and Tg is detected at 264 cm^{-1} [54–59]. The intraionic stretching modes of dumbbell-shaped Se$_2$ units are primarily responsible for these active modes in NiSe$_2$ with a pyrite-type structure [55,58]. NiSe's characteristic longitudinal optical (LO) one-phonon mode is visible in the band at 510 cm^{-1}, while the band appearing at 820 cm^{-1} arose from the Si-O-Si of the glass slide. The asymmetric $v_{as}(COO^-)$ stretching vibration of the carboxylate group is responsible for the band appearing around 1464 cm^{-1} [23,24]. This indicates that the capping agent is chemisorbed as carboxylates onto Ni ions on the NiSe$_2$QD surface. According to Naik et al.

[25], the deprotonation of the carboxylic acid group makes it absorb onto the metal as carboxylates. C-H stretching is signified by the bands at 2711 cm^{-1} [26].

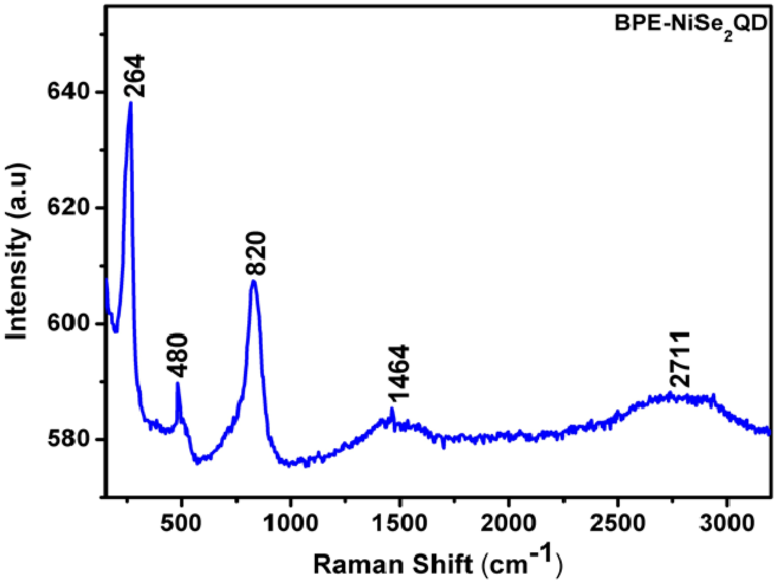

Figure 5. 3. Raman spectrum for BPE-NiSe$_2$QD.

5.2.4 Morphological properties of BPE-NiSe$_2$QD

The surface morphology of the as-synthesised BPE-NiSe$_2$QD was evaluated by high-resolution scanning electron microscopy (HRSEM). The HR-SEM image in Figure 5.4A shows that the particles are spherical but display some degree of agglomeration. The elemental composition of the nanomaterial was investigated using energy-dispersive X-ray spectroscopy (EDX), as shown in Figure 5.4B, which revealed the presence of nickel, selenium, carbon, and oxygen atoms. The presence of the carbon and oxygen atoms is due to the presence of carboxylic acid or polysaccharide groups in BPE.

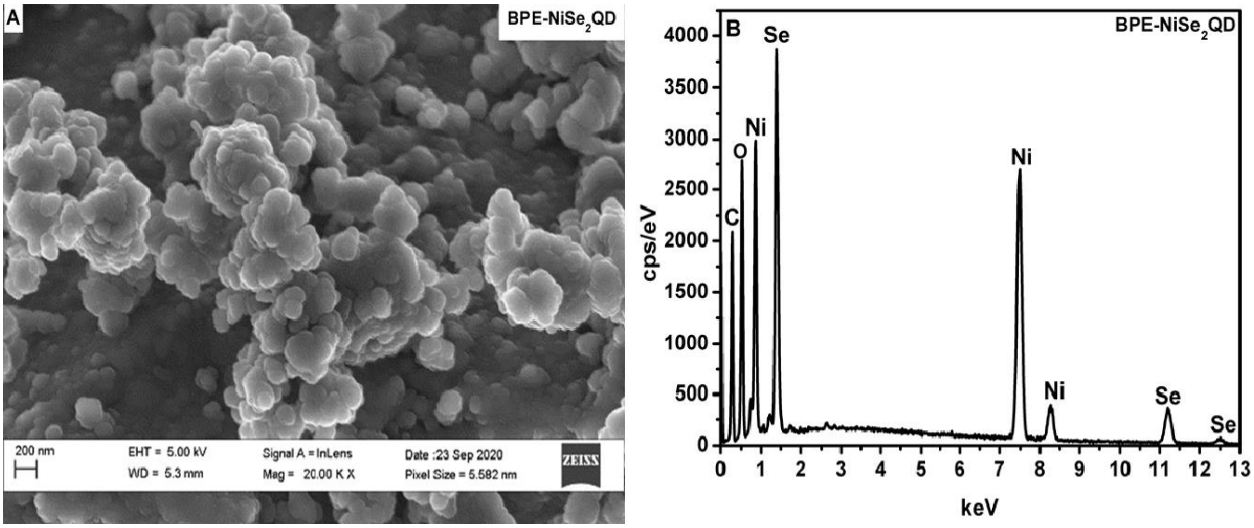

Figure 5. 4. A: HRSEM micrograph and B: EDX spectra for BPE- NiSe$_2$QD.

5.2.5 HR-TEM and XRD analysis of BPE-NiSe$_2$QD

The structural morphology of BPE-NiSe$_2$QD was investigated by high resolution transmission electron microscopy (HRTEM), as depicted in Figure 5.5A. The HRTEM images show very small particles with sizes less than 5 nm, although there is some degree of aggregation of small particles that have formed bigger structures in the presence of the capping agent shown in insert A1. Sobhani et al. [27] reported that if a surfactant/capping agent is not used during the synthesis of the nanomaterials, it makes the particles unstable and causes them to aggregate into flower-like structures. The nucleation of nickel and selenium takes place immediately after mixing the two precursors. The absence of a surfactant causes the nucleation rate of the material to attain very high values within a short space of time because there is nothing available to cover the nuclei [27]. Some of the capping agent might have been washed away and left the nuclei of the sample exposed, later leading to the agglomeration of particles. The agglomeration may also be due to the possibility that BPE may be a weak capping agent. As shown in Figure 5.5B, the selected area electron diffraction pattern (SAED) shows high crystalline behaviour.

The crystallinity of the synthesised QD was determined by XRD. The XRD pattern shown in Figure 5.5C is indicative of penroseite NiSe$_2$. The diffraction peaks seen at 2θ values of 23.5, 29.9, 33.4, 38.9, 41.2, 50.7, 55.5, 59.8, and 72.6 ° can be indexed to (111), (200), (210), (211), (220), (311), (320), (400) and (421) respectively. The peaks observed at 2θ = 23.5 are due to selenium (JCPDS card: 06-0362) [28–31]. These diffraction peaks were identified using JCPDS card no.

96-901-2538 which corresponds to the cubic phase of $NiSe_2$ (penroseite), which is structurally similar to pyrite. Figure 5.5D shows the simulated crystal structure of $NiSe_2$ with a space group of P a-3 (205).

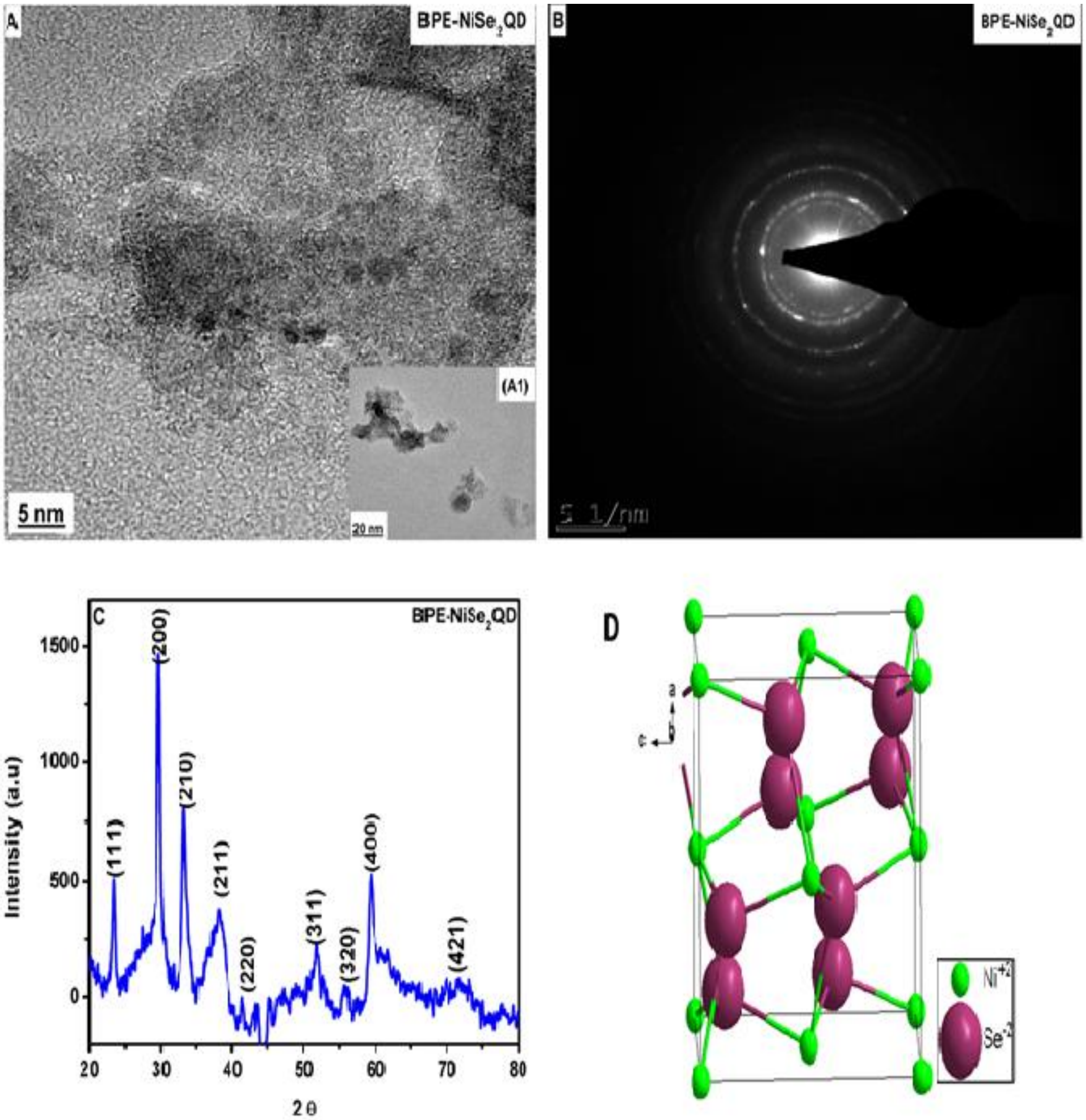

Figure 5. 5. HR-TEM micrographs of A: BPE- $NiSe_2$QD at 5 nm scale view and (A1) inserted region at 20 nm scale view, B: SAED pattern of BPE-$NiSe_2$QD, C: XRD pattern of BPE-$NiSe_2$QD, D: Simulated crystal structure of $NiSe_2$.

5.2.6 UV-Vis and Optical Bandgap

The optical properties of the precursors, capping agent and BPE-$NiSe_2$QD were investigated by a UV-Vis spectrophotometer. Figure 5.6A shows the spectra obtained for (a) $NiCl_2$, (b) BPE, (c) Ni-BPE, and (d) reduced selenium, of which (a) and (d) have already been discussed in Chapter 4. The absorption spectra for BPE showed the appearance of five bands at 280 nm, 321 nm, 450 nm, 493 nm, and 641 nm. This was expected since the banana peel extract consists of many compounds. However, due to the preparation method used, only water-soluble substances were present in the extract [32]. The strong absorbance band at 280 nm and the small bump at 321 nm can be credited to the presence of phenolic compounds [33,34]. Polyphenols have π conjugated systems with hydroxyl-phenolic groups. The electronic transitions of the π-type molecular orbitals provide the UV-Vis spectrum of this group of compounds [34]. The yellow colour of the ripe banana peel is due to the presence of carotenoids, which have been previously detected at 450 nm [13]. This correlates with our findings. Anthocyanin, a kind of flavonoid, could be responsible for the absorbance band at 493 nm. According to Saha et al. [35], a typical anthocyanin spectrum exhibits two basic absorbance bands, the first at 260-280 nm and the second at 490-550 nm. Fu et al. [13] have also detected the presence of anthocyanins in banana peel extract at 520 nm. The strong absorbance band at 641 nm could be due to pheophytin, an intermediate compound from the degradation of chlorophyll [36,37]. Figure 5.6A (c) shows an overall decrease in the intensity of the bands in Ni-BPE, which could indicate that the Ni species has been successfully capped and reduced. The insert (d) shows a weak absorbance band at 493 nm for the reduced Se. This could be due to Se_2^{2-} species [38]. The UV-Vis spectra of BPE-$NiSe_2$QD in Figure 5.6B revealed absorbance bands at 275 nm, 329 nm, 422 nm, and 451 nm, respectively. The metal to ligand charge transfer (i.e., nickel ions and BPE capping agent) is responsible for the absorbance band at 275 nm. The spectrum shows that the BPE-$NiSe_2$QD have a distinctive absorption band at 329 nm, which corresponds to an energy bandgap of 2.99 eV shown in Figure 5.6C. At 424 nm, the Se_2^{2-} species of the QD was visible, while the absorbance band at 551 nm showed the presence of pheophytin. Figure 5.6D shows the PL spectra obtained for BPE-$NiSe_2$QD at an excitation wavelength of 500 nm.

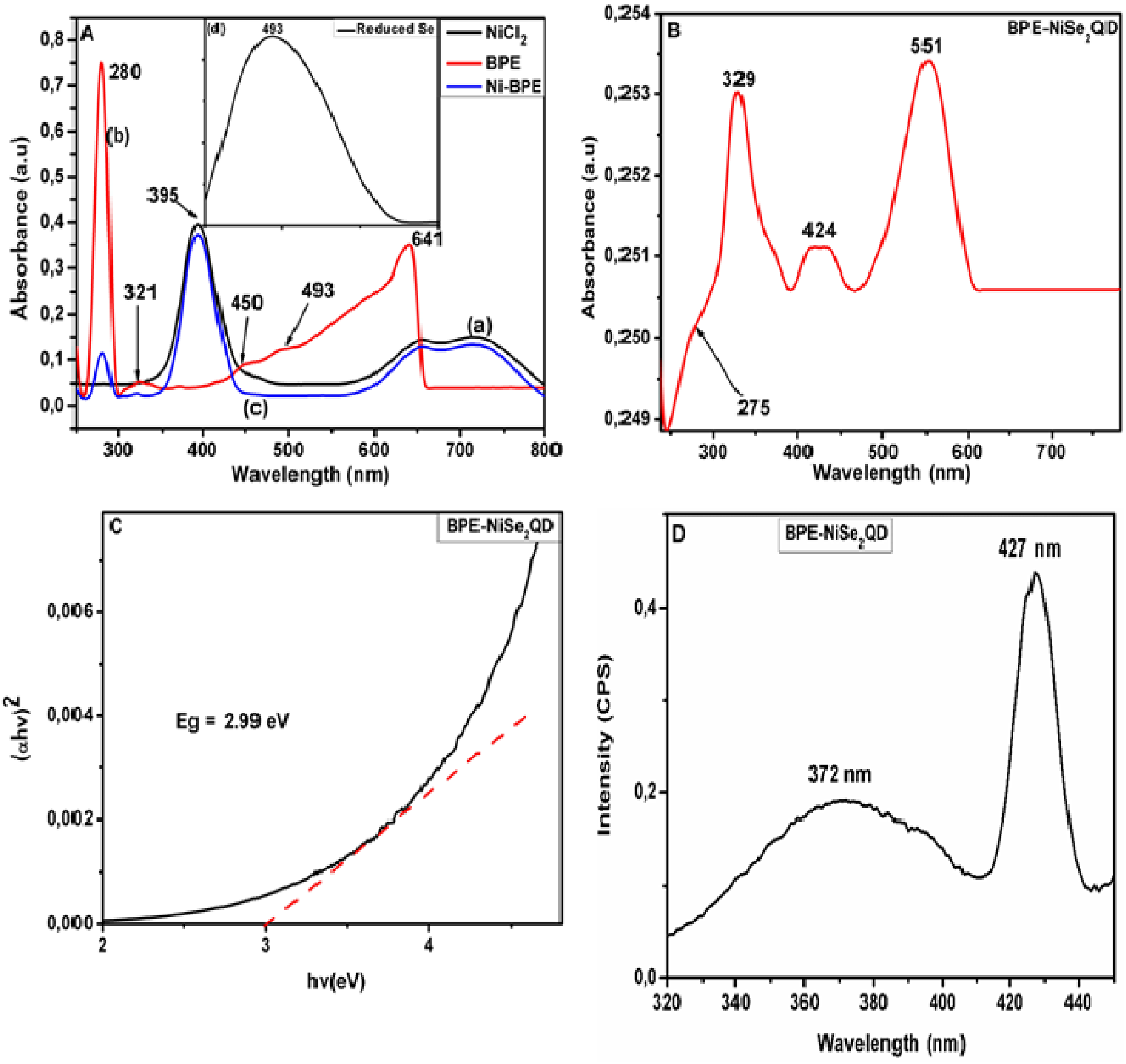

Figure 5. 6. UV-Vis spectra of A: precursors, B: BPE-NiSe$_2$QD, C: Tauc plot and D: PL spectra of BPE-NiSe$_2$QD.

5.2.7 Electrochemical studies of Au/Nafion

Nafion is a perfluorinated sulfonated ion-exchange polymer. Nafion films have been extensively used for electrode modification in electrochemistry in the construction of chemical or biosensors [39–42]. It is chemically inert, highly stable in aqueous solutions, possesses anti-fouling properties, and has high mechanical strength for stabilising the deposited metal layer [40,41,43–45]. The oxidation response of Nafion on a bare Au electrode is shown in Figure 5.7A (a and b). One oxidation peak was observed at the gold electrode at 0.67 V which is a gold oxide peak. A new peak appeared at 0.21 V and a decrease in the current intensity was observed in the region of the gold oxide peak when Nafion was added to the electrolyte, as shown in Figure 5.7A (b). The new peak may be due to the adsorption of sulfonate groups on the gold electrode [46] and the drop in current could be a result of this adsorption, which reduced the number of active sites on the gold electrode [47]. This is similar to the observations made by McGovern et al. [47], where Nafion blocked a percentage of the active sites of the electrode, resulting in a lower surface area and lower current. Three reduction peaks were seen in Figure 5.7B at 0.51 V, 0.02 V and -0.29 V. The peak at 0.51 V is due to the reduction of gold oxides, while the peaks at 0.02 V, and -0.29 V could be attributed to the reduction of the sulfonate or fluorocarbon groups present in Nafion. Before applying Nafion as a binder for the sensor, the Nafion modified electrode (Au/Nafion) was tested for its response to the nevirapine drug. From the results shown in Figure 5.7A (c) and Figure 5.7B (c), it can be concluded that Au/Nafion was not responsible for NVP detection as no significant change was seen in the voltammograms.

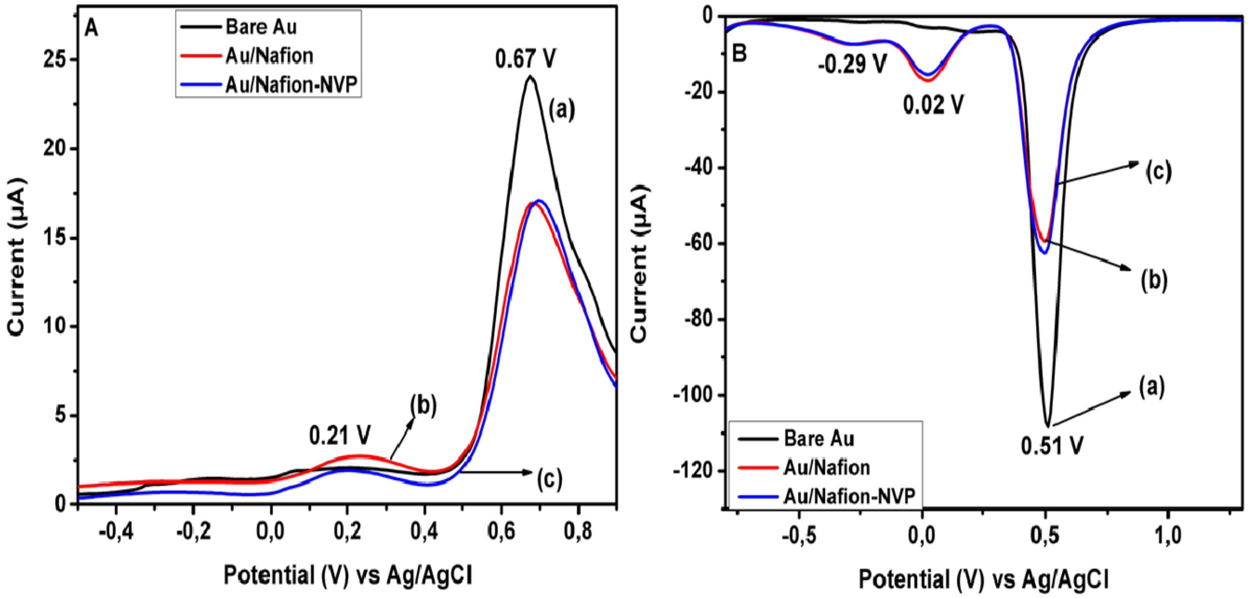

Figure 5. 7. ODPV of A: (a) Bare Au, (b) Au/Nafion, (c) Au/Nafion-NVP and B: RDPV of (a) Bare Au, (b)Au/Nafion, (c) Au/Nafion-NVP in 0.1 M PBS pH 7.4 at 30 mV/s.

5.2.8 Electrochemistry of BPE-$NiSe_2$QD

Differential pulse voltammetry was used to investigate the electrocatalytic characteristics of BPE-$NiSe_2$QD on a Nafion/Au modified electrodes and the results are shown in Figure 5.8. The signatures seen are very similar to the ones obtained for 3-MPA- $NiSe_2QD$ and have been discussed in section 4.2.7. The anodic peak at -0.41 V is due to Ni^{2+} produced by the oxidation of the QD, and that at -0.21 V arises from the interaction between the metal and the BPE capping agent (metal to ligand charge transfer). The presence of Nafion is shown by the anodic peak at 0.19 V, while the anodic peak at 0.44 V is attributed to the Se (0) oxidation of the QD. The characteristic peak of the $NiSe_2QD$ oxidation is shown at 0.76 V. The cathodic peaks at 1.11 V, 0.54 V, -0.04 V and -0.40 V are attributed to Ni (III) to Ni (II) reduction, reduction of the gold oxide, Se (IV) to Se (0) reduction and the characteristic reduction of the $NiSe_2QD$, respectively.

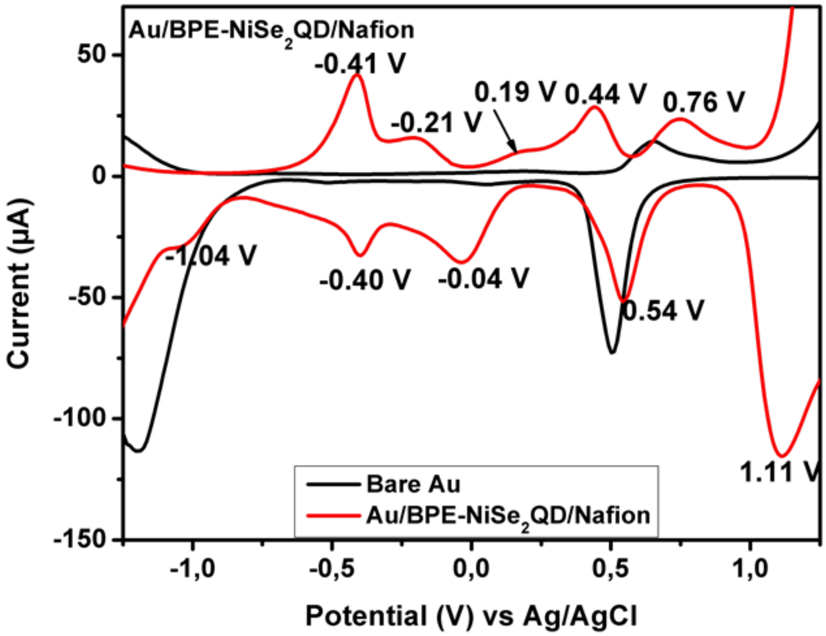

Figure 5. 8. Electrochemistry of BPE-$NiSe_2QD$.

5.2.9 Effect of pH

The electrochemical behaviour of 10 nm NVP on Au/BPE-$NiSe_2QD$/Nafion was investigated in 0.1 M PBS with different pH values (ranging from 4.0 to 9.0). It can be seen that the oxidation peak potential shifted towards negative potential with increasing pH values in Figure 5.9A. This indicates that protons are involved in the electrochemical reaction. A good linear relationship between E_{pa} and pH was obtained from the linear regression equation as shown in equation 5.1:

$$E_{pa} (V) = -0.0555 \text{ pH} + 1.134 \ (R^2 = 0.989) \qquad (5.1)$$

The slope value obtained of -55.5 mV/pH is close to the Nernstian theoretical slope value of −59 mV, indicating that the oxidation of NVP involves an equal number of electrons and protons. As can be seen in Figure 5.9B, the oxidation peak current of NVP increased from pH 4.0 to pH 7.0 and then decreased with a further increase in the buffer pH. The maximum current value was obtained at pH 7.0, therefore pH 7.4 was selected as the optimal pH for this study.

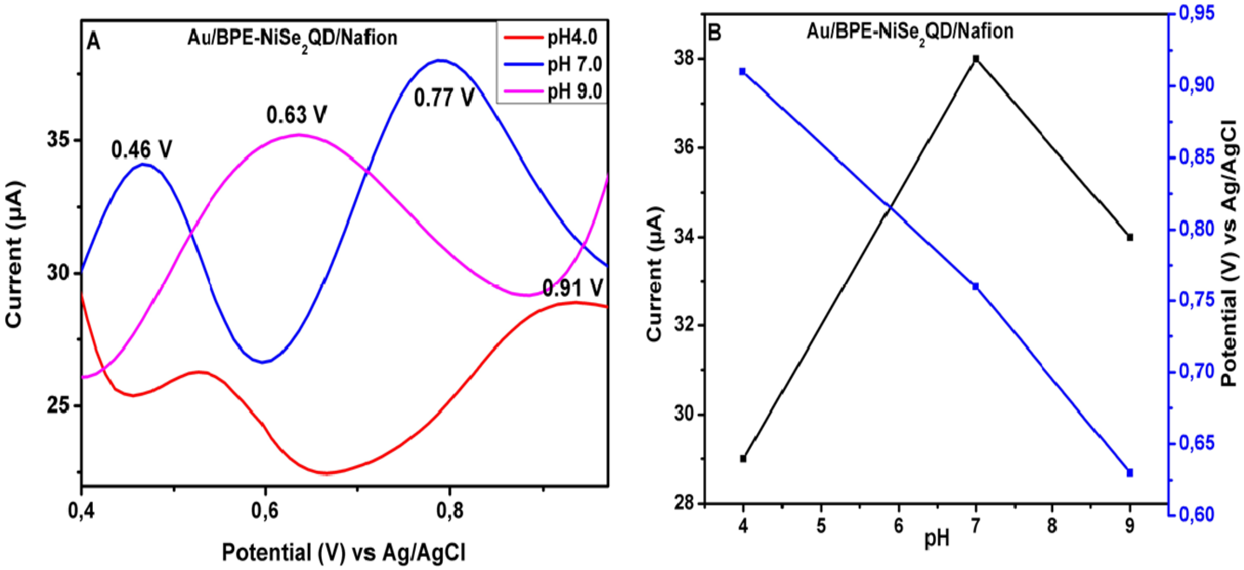

Figure 5. 9. A: DPV responses of Au/BPE-NiSe$_2$QD/Nafion to 10 nM nevirapine at pH 4.0, pH 7.0 and pH 9 in 0.1 M PBS at a scan rate of 30 mV/s and B: the influence of solution pH on oxidation peak current and potential.

5.2.10 Electrochemical determination of NVP

Differential pulse voltammetry was used for the voltammetric sensing of NVP because of its higher sensitivity and quantitative analysis ability than cyclic voltammetry. Figure 5.10A shows the results obtained when Au/L-cyst/BPE-NiSe$_2$QD was used to detect NVP under optimal conditions. Unfortunately, its use as an NVP sensor was hampered by signal instability. The gradual increase of NVP concentration would lead to either an increase or a decrease in the signal. This inconsistency could be due to the lack of stability of the BPE-NiSe$_2$QD on the gold electrode surface, which may have resulted in them falling off the electrode. It is also an indication that no strong amide bonds could have formed between the L-cysteine monolayer and the BPE-NiSe$_2$QD.

To address this problem, Nafion was then used to modify the electrode in place of L-cysteine. Nafion was employed as an adhesive agent or catalyst binder [41,47,48]. It was incorporated into the sensor system through deposition on top of the BPE-$NiSe_2$QD, which were already drop-cast onto the gold electrode. Preliminary studies revealed that a Nafion-modified gold electrode exhibited no electrochemical response to the presence of NVP. Therefore, the performance of Au/BPE-$NiSe_2$QD/Nafion was evaluated for NVP detection. The incorporation of Nafion to the electrode resulted in well resolved and good signal stability as shown in Figure 5.10B. The oxidation peak current gradually increased with an increase in NVP concentration and shifted to negative potentials from 0.76 V to 0.73 V. This observation was due to the presence of BPE-capped $NiSe_2$QD, which promoted fast electron transfer between the analyte and the electrode. However, a saturation point was reached at concentrations above 1.05 pM as the addition of more NVP led to an insignificant change in the peak current, as seen in Figure 5.10C. As seen in Figure 5.10D, the dynamic linear range was 0.08 pM–1.21 pM and the sensitivity of the sensor was determined to be 5.52 µA/pM. The limit of detection was calculated to be 0.024 pM (0.0064 ng/L). The sensitivity of the Au/BPE-$NiSe_2$QD/Nafion-based sensor was compromised by the presence of Nafion, which may have blocked some of the active sites of the sensor [47] and also hindered the transfer of electrons between the electrode and the analyte [49]. The LOD was also found to be higher than that of the 3-MPA-$NiSe_2$QD/L-cyst/Au-based electrochemical sensor by 0.011 pM (0.0029 ng/L).

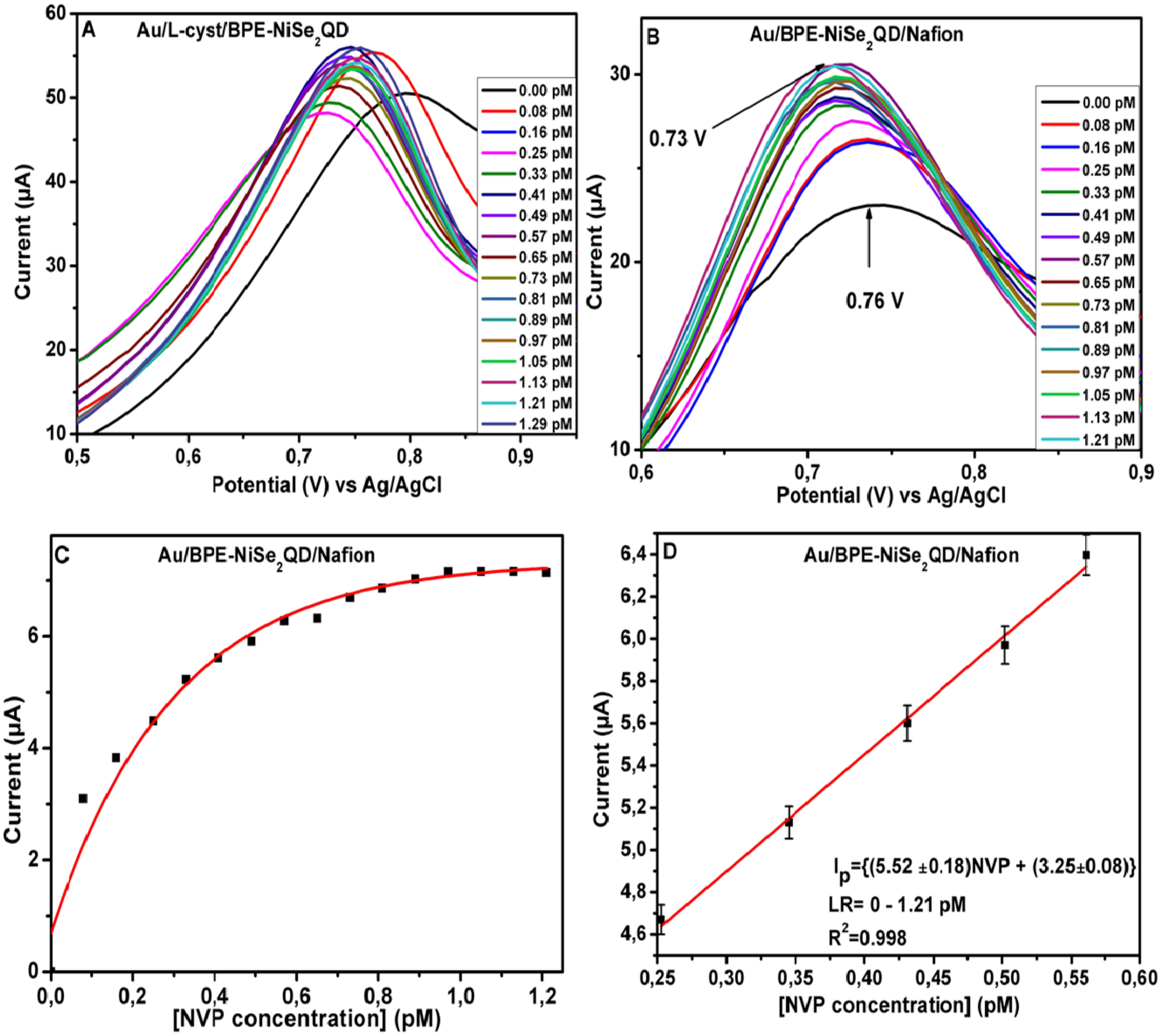

Figure 5. 10. DPV response of A: Au/L-cyst/BPE-NiSe$_2$QD and B: Au/BPE-NiSe$_2$QD/Nafion on successive addition of nevirapine from 0.08 pM to 1.21 pM in 0.1 M PBS (pH 7.4) at 30 mV/s, C: corresponding exponential curve and D: calibration plot.

5.2.11 Effect of interfering species

Under optimal conditions, the influence of I0 µM Tenofovir, 1 mM EDC, and 10 µM Diclofenac in the detection of 10 nM nevirapine was investigated. As illustrated in Figure 5.11, the DPV signal did not change significantly when tenofovir was added. Strangely, an enhancement of about 8% in the signal was observed after the addition of EDC and diclofenac to the buffer solution. The interferents in this study were chosen based on their point sources, which included painkillers (diclofenac) and an ARV used in combination with NVP (tenofovir), both of which are commonly in the reach of HIV patients. However, without a doubt, Nafion could have tempered with the sensitivity of the sensor.

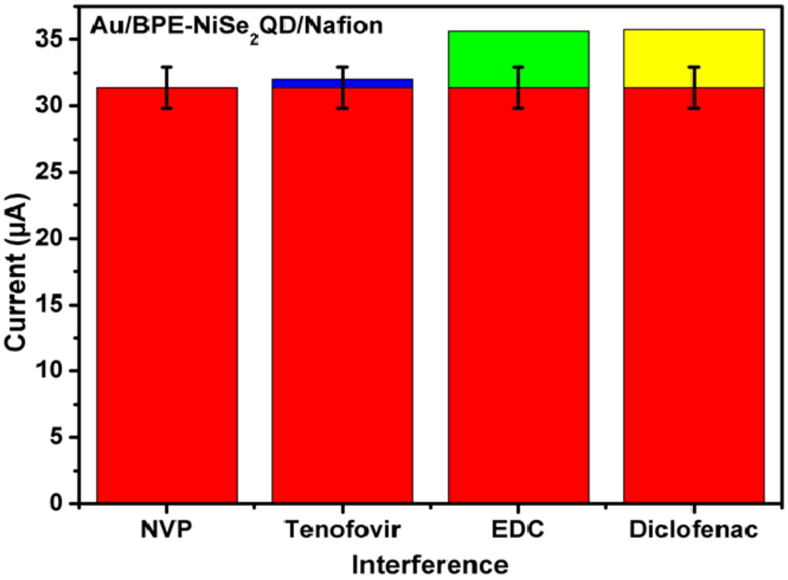

Figure 5. 11. Effect of interferents such as tenofovir, EDC and diclofenac on the oxidation peak of NVP in 0.1 M PBS (pH 7.4).

5.2.12 Stability study

The stability of the Au/BPE-NiSe$_2$QD/Nafion sensor was investigated over 9 days under two different conditions. Figure 5.12A shows that after storage of the sensor in the dark at room temperature, the current response of 10 nM nevirapine decreased to 84% of its initial response. On the other hand, the sensor did not show any noticeable changes after being stored in the refrigerator at 4 °C. Figure 5.12B shows the sensor retained 96% of its initial current response, indicating very good stability. Therefore, putting the sensor in the refrigerator is preferable because it helps to maintain the sensor's integrity. The good stability of the sensor was also aided by the presence of Nafion. The addition of Nafion, an anchoring agent, increased the sensor's stability by keeping the BPE-NiSe$_2$QD firmly attached to the electrode. This in turn improved the sensor's reproducibility [50].

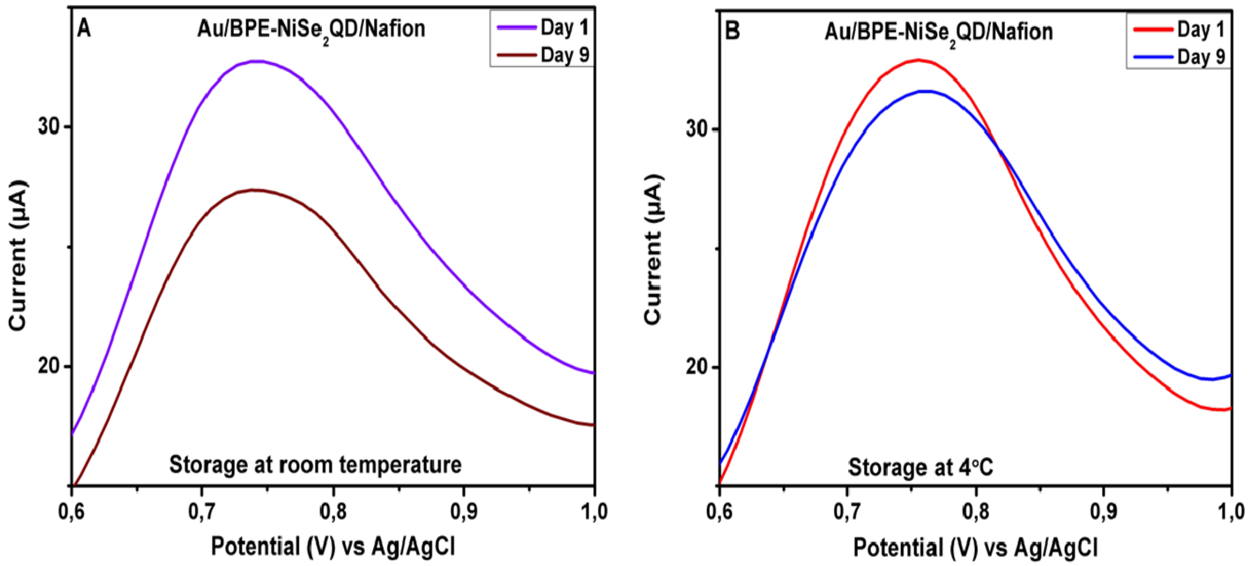

Figure 5. 12. Effect of storage conditions on the response of Au/BPE-NiSe$_2$QD/Nafion to NVP at A: room temperature and B: at 4 °C.

5.2.13 Application in real samples

To evaluate the practicability of the developed Au/BPE-NiSe$_2$QD/Nafion sensor for routine analysis, the sensor was used to determine the nevirapine concentration in wastewater samples (Northern wastewater effluent, 26-04-2021). The samples were spiked with different amounts of known NVP concentrations. Figure 5.13 shows a typical voltammogram for the responses obtained for three samples. The amount of NVP in the samples was calculated from the calibration plot, and the corresponding satisfactory results are summarised in Table 5.1. The recoveries of NVP in wastewater samples were in the range of 85 % to 108 %. The low RSD values of below 7 % and the good recoveries obtained highlight the reproducibility of the results. Therefore, the fabricated sensor could be effectively applied to real-time sample analysis.

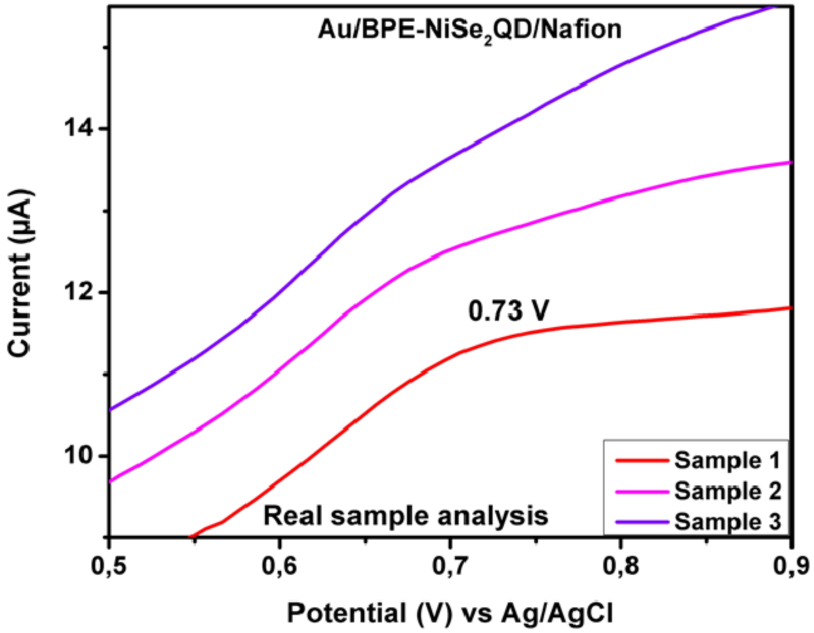

Figure 5. 13. DPV responses of Au/BPE-NiSe$_2$QD/Nafion to the addition of 0.08 pM to 0.49 pM NVP in the wastewater sample

Table 5. 1: Determination of NVP in real wastewater samples.

Real waste water sample	**NVP added (pM)**	**NVP Found ± error**	**Recovery (%)**	**% RSD**
1	0.080	0.068 ± 0.14	85	4.7
2	0.250	0.270 ± 0.18	108	6
3	0.490	0.482 ± 0.21	98	7

Conclusion

In this work, a novel electrochemical sensor for NVP was fabricated by the incorporation of BPE-NiSe$_2$QD onto a gold electrode. The green synthesis approach of QD using banana peel extract was a cost-effective, non-toxic, and eco-friendly method. SAXS and HRTEM studies revealed the very small sizes of BPE-NiSe$_2$QD to be 6 nm or less. HRSEM validated the spherical shape of the QD, while EDX analysis revealed the presence of Ni, Se, C and O, with the C, and O originating from the capping agent. The FTIR confirmed that the QD were functionalised with the banana peel extract. XRD and SAED revealed the high crystallinity nature of the synthesised QD. The deposition of BPE-NiSe$_2$QD onto the electrode was followed by Nafion for stabilisation of the

QD. This Au/BPE-$NiSe_2$QD/Nafion-based sensor exhibited electro-catalytic activity towards NVP oxidation, evident from the increased peak current and decreased potential. This could be attributed to the presence of BPE-$NiSe_2$QD, which accelerated the transfer of electrons between the electrode and the analyte. The proposed sensor exhibited high sensitivity and selectivity, long-term stability, reasonable reproducibility, and a low detection limit compared to other reported sensors (Chapter 2). The sensor was also successfully utilised to determine trace amounts of NVP in wastewater samples with satisfactory results. However, some improvements that can be made in the preparation of this sensor include the use of stronger capping agents to ensure the stability of the QD on the electrode or the use of a different binder that will not inhibit the signal. The effect of different electrolytes can also be investigated, as well as the effect of a variety of interferences on the response of the sensor to NVP.

References

1. H. M. M. Ibrahim, J. Radiat. Res. Appl. Sci. **8**, 265 (2015).
2. A. Narayanamma, M. E. Rani, and K. M. Raju, Int. J. Sci. Res. ISSN **5**, 1434 (2013).
3. T. Kokila, • P S Ramesh, and • D Geetha, Appl. Nanosci. **5**, 911 (2015).
4. S. Kamsonlian, S. Suresh, C. B. Majumder, and S. Chand, Int. J. Sci. Technol. Manag. **2**, 1 (2011).
5. T. C. Prathna, N. Chandrasekaran, A. M. Raichur, and A. Mukherjee, Colloids Surfaces B Biointerfaces **82**, 152 (2011).
6. P. Velmurugan, K. Anbalagan, M. Manosathyadevan, K. J. Lee, M. Cho, S. M. Lee, J. H. Park, S. G. Oh, K. S. Bang, and B. T. Oh, Bioprocess Biosyst. Eng. **37**, 1935 (2014).
7. M. Nasrollahzadeh and S. M. Sajadi, Ceram. Int. **41**, 14435 (2015).
8. Y. Yuan, Y. Zhao, J. Yang, Y. Jiang, F. Lu, Y. Jia, and B. Yang, Food Chem. **218**, 406 (2017).
9. G. K. Deokar and A. G. Ingale, RSC Adv. **6**, 74620 (2016).
10. P. P. Sarma, N. Gurumayum, A. K. Verma, and R. Devi, Food Funct. **12**, 4749 (2021).
11. R. González-Montelongo, M. Gloria Lobo, and M. González, Food Chem. **119**, 1030 (2010).
12. G. B. Seymour, C. Lizada, J. E. Taylor, and G. A. Tucker, *Biochemistry of Fruit Ripening* (1993).
13. X. Fu, S. Cheng, Y. Liao, B. Huang, B. Du, W. Zeng, Y. Jiang, X. Duan, and Z. Yang, Comparative Analysis of Pigments in Red and Yellow Banana Fruit (2018).

14. D. Gopi, K. Kanimozhi, N. Bhuvaneshwari, J. Indira, and L. Kavitha, Spectrochim. Acta - Part A Mol. Biomol. Spectrosc. **118**, 589 (2014).

15. P. D. Pathak, S. A. Mandavgane, and B. D. Kulkarni, Curr. Sci. **113**, 444 (2017).

16. E. Nasra, R. Sari, S. B. Etika, D. Kurniawati, and T. K. Sari, Adv. Biol. Sci. Res. **10**, 238 (2020).

17. M. Green, J. Mater. Chem. **20**, 5797 (2010).

18. U. Feleni, U. Sidwaba, H. Makelane, and E. Iwuoha, J. Nanosci. Nanotechnol. **19**, 1 (2019).

19. P. B. Franco, L. A. De Almeida, R. F. C. Marques, M. A. Da Silva, and M. G. N. Campos, Int. J. Polym. Sci. **2017**, 1 (2017).

20. L. S. Maia, L. D. Duizit, F. R. Pinhatio, and D. R. Mulinari, Carbon Lett. **31**, 749 (2021).

21. C. Feng, Z. Jin, M. Zhang, and Z. S. Wang, Electrochim. Acta **281**, 237 (2018).

22. E. Ahmadi, M. Reza, V. Riahifar, and H. Momeneh, Microchem. J. **146**, 1218 (2019).

23. M. S. Abd El-Sadek, J. Ram Kumar, and S. Moorthy Babu, Curr. Appl. Phys. **10**, 317 (2010).

24. J. L. Castro, M. R. López-Ramírez, J. F. Arenas, and J. C. Otero, J. Raman Spectrosc. **35**, 997 (2004).

25. E. Indrajith Naik, H. S. Bhojya Naik, R. Viswanath, I. K. Suresh Gowda, and B. R. Kirthan, Mater. Sci. Energy Technol. **4**, 23 (2021).

26. R. W. Berg, Appl. Spectrosc. Rev. **50**, 193 (2015).

27. A. Sobhani, M. Salavati-Niasari, and F. Davar, Polyhedron **31**, 210 (2012).

28. K. S. Bhat and H. S. Nagaraja, Int. J. Hydrogen Energy **43**, 19851 (2018).

29. C. Zhao, Y. Zhu, W. Liu, Z. Chen, Z. Wang, and P. Feng, J. Solid State Chem. **266**, 37 (2018).

30. Z. Zhuang, Q. Peng, J. Zhuang, X. Wang, and Y. Li, Chem. - A Eur. J. **12**, 211 (2005).

31. N. Moloto, M. J. Moloto, N. J. Coville, and S. Sinha Ray, J. Cryst. Growth **324**, 41 (2011).

32. A. Dmochowska, J. Czajkowska, R. Jędrzejewski, W. Stawiński, P. Migdał, and M. Fiedot-Toboła, Int. J. Biol. Macromol. **165**, 1581 (2020).

33. S. Lopes, L. Moresco, L. A. M. Peruch, M. Rocha, and M. Maraschin, Adv. Intell. Syst. Comput. **616**, 290 (2017).

34. J. Luis Aleixandre-Tudo and W. du Toit, in Front. New Trends Sci. Fermented Food Beverages (2019), pp. 1–21.

35. S. Saha, J. Singh, A. Paul, R. Sarkar, Z. Khan, and K. Banerjee, J. AOAC Int. **103**, 23 (2021).

36. A. A. Khoozani, A. E. D. A. Bekhit, and J. Birch, Int. J. Biol. Macromol. **130**, 938 (2019).

37. J. W. Heaton and A. G. Marangoni, Trends Food Sci. Technol. **7**, 8 (1996).

38. H. Rojo, A. C. Scheinost, B. Lothenbach, A. Laube, E. Wieland, and J. Tits, Dalt. Trans. **47**, 4209 (2018).

39. P. Pang, F. Yan, H. Li, H. Li, Y. Zhang, H. Wang, Z. Wu, and W. Yang, Anal. Methods **8**, 4912 (2016).

40. Z. Wang, H. Zhang, S. Zhou, and W. Dong, Talanta **53**, 1133 (2001).

41. H. Chen, Y. Wang, Y. Liu, Y. Wang, L. Qi, and S. Dong, Electrochem. Commun. **9**, 469 (2007).

42. Y. P. Dong, J. Lumin. **130**, 1539 (2010).

43. H. Yi, K. Wu, S. Hu, and D. Cui, Talanta **55**, 1205 (2001).

44. Z. Wang, G. Liu, L. Zhang, and H. Wang, Ionics (Kiel). **19**, 1687 (2013).

45. Y. C. Tsai, S. C. Li, and J. M. Chen, Langmuir **21**, 3653 (2005).

46. M. Ahmed, D. Morgan, G. A. Attard, E. Wright, D. Thompsett, and J. Sharman, Phys. Chem. C **115**, 17020 (2011).

47. M. S. McGovern, E. C. Garnett, C. Rice, R. I. Masel, and A. Wieckowski, J. Power Sources **115**, 35 (2003).

48. I. Ivanov, Y. T. Ahn, T. Poirson, M. A. Hickner, and B. E. Logan, Int. J. Hydrogen Energy **42**, 15739 (2017).

49. T. Mudrinić, Z. Mojović, P. Banković, N. Jović-Jovičić, A. Ivanović-Šašić, A. Milutinović-Nikolić, and D. Jovanović, Gold Bull. **50**, 191 (2017).

50. H. S. Jang, D. Kim, C. Lee, B. Yan, X. Qin, and Y. Piao, Inorg. Chem. Commun. **105**, 174 (2019).

CHAPTER SIX

CONCLUSION AND RECOMMENDATIONS

Summary

This chapter presents conclusions for the work presented and makes recommendations for future research.

6.1 Conclusions

In conclusion, we have successfully fabricated a highly sensitive and selective $NiSe_2$QD -based electrochemical sensor for the detection of nevirapine drug for the first time. The colloidal $NiSe_2$QD were synthesised using a cost-effective, straightforward, and reproducible aqueous approach. 3-MPA and BPE were used as capping and stabilising agents. The effect of these capping agents on the functionalisation of the QD surface was examined by microscopic, spectrophotometric, and electrochemical techniques. SAXSpace, HR-TEM, and HR-SEM revealed the formation of spherical, small-sized QD about 6 nm in diameter or less, while XRD and SAED revealed high crystallinity. FTIR and Raman analysis confirmed the presence of the capping agent on the surface of the QD, revealing the presence of various distinctive functional groups such as thiol, carboxylic acid, alkyl, and hydroxyl groups. The elemental composition of the QD was determined by EDX, which showed the presence of Ni, Se, C, and O. The C and O observed were coming from the capping agents. UV-Vis studies showed absorption band edges at 331 nm and 329 nm, corresponding to energy band gap values of 3.91 eV and 2.99 eV for 3-MPA-$NiSe_2$QD and BPE-$NiSe_2$QD, respectively. The electrochemical detection of nevirapine showed a characteristic oxidation peak at 0.76 V in 0.1 M PBS. The electrochemical sensors exhibited enhanced electroactivity, which was attributed to the catalytic effect of the incorporated quantum dots. The 3-MPA-$NiSe_2$QD/L-cyst/Au electrochemical sensor performed better than the BPE-$NiSe_2$QD/Nafion/Au sensor, evidenced by the lower detection limit of 0.0035 ng/L compared to 0.0064 ng/L and a significantly higher sensitivity of 6.15 µA/pM compared to 5.52 µA/pM obtained by the BPE-$NiSe_2$QD/Nafion/Au sensor. This slight deviation was attributed to the use of Nafion as a binder to prevent the quantum dots from falling off the electrode, which unfortunately resulted in signal inhibition. The oxidation peak current of NVP had a linear range of 0–1.21 pM with a correlation coefficient of 0.998. The application of both sensors in the determination of nevirapine in real wastewater samples showed good recoveries in the range of 85%-108%, which indicates that the sensors can be employed in real-time sample analysis. The exceptional results obtained using these sensors qualifies them for future use in detecting nevirapine in wastewater compared to other sensors that have been reported in literature as they perform better. The very low LODs obtained are comparable to those obtained whilst using highly sophisticated techniques such as liquid chromatography coupled to (tandem) mass spectrometry (LC-MS/MS) and Ultrahigh performance liquid chromatography system coupled to a triple quadrupole mass spectrometry, with electrospray ionization (ESI) (UPLC-ESI-MS/MS). Therefore, the sensing devices may be a suitable alternative to the spectrometric methods.

6.2 Recommendations for future study

Further studies of the QD-based electrochemical sensor system and applications are discussed below.

- It is proposed that the influence of various electrolytes on the sensor's response should be investigated.
- Because the banana peel extract alone was unable to cause the QD to adhere firmly to the electrode, a combination of fruit extracts can be utilised as a capping agent.
- In the case that the quantum dots fall off the electrode, alternative binding agents that will not inhibit the signal can be tested if available.
- The material can be used in energy applications for example in solar cells, hydrogen evolution reactions, oxygen evolution reactions or water splitting.
- It is suggested that the sensor can be used to detect a variety of contaminants in real water.